

22098194

MICHIGAN STATE UNIVERSITY LIBRARIES



3 1293 00564 9649

LIBRARY
Michigan State
University

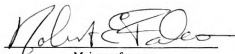
This is to certify that the
dissertation entitled

A STUDY OF TURBULENCE PRODUCTION AND MODIFICATION IN
BOUNDARY LAYERS USING A NEW PHOTOCHROMIC VISUALIZATION
TECHNIQUE
presented by

Chin-Chou Chu

has been accepted towards fulfillment
of the requirements for

Ph. D. degree in Mechanical Engineering


Major professor

Date December 30, 1987



RETURNING MATERIALS:
Place in book drop to
remove this checkout from
your record. FINES will
be charged if book is
returned after the date
stamped below.

--	--	--

503-3561

**A STUDY OF TURBULENCE PRODUCTION AND MODIFICATION IN
BOUNDARY LAYERS USING A NEW PHOTOCHROMIC VISUALIZATION
TECHNIQUE**

by

Chin-Chou Chu

A DISSERTATION

Submitted to
Michigan State University
in partial fulfillment of the requirements
for the degree of

DOCTOR OF PHILOSOPHY

Department of Mechanical Engineering

1987

ABSTRACT

A STUDY OF TURBULENCE PRODUCTION AND MODIFICATION IN BOUNDARY LAYERS USING A NEW PHOTOCROMIC VISUALIZATION TECHNIQUE

A major extension of Laser Induced Photochemical Anemometry (LIPA) has been developed that enables the velocity components and their gradients over a two-dimensional domain of a fluid flow to be measured. As a result, the transverse vorticity component and the strain rate as well as the Reynolds stresses in the interrogation plane can be determined. Calibration depends only on a time and a length scale. Comparison of measurements with the exact solution in a Stokes' layer indicates that the technique's accuracy can be predicted by classical error analysis and that it is comparable or better than that achievable with the best single point probe techniques. Using the LIPA technique we have quantified several complicated turbulent and unsteady flows which include the skin friction measurement on compliant surfaces and both temporal and spatial information pertaining to the velocity distributions, spanwise vorticity distributions, and streamwise vorticity distributions associated with the vortex ring/moving wall interaction model of the turbulence production process. The results of this study extend our understanding of turbulence production and modification concerning boundary layers and also provide a rational basis for boundary layer control.

ACKNOWLEDGEMENTS

On completion of this dissertation, I have reached the end of my formal education. I would like to acknowledge the advice and support of a number of people.

I would like to acknowledge the support of the Office of Naval Research, grant monitor: Dr. Reischman; and the Air Force Office of Scientific Research, grant monitor: Dr. J. McMichael, for their support in the completion of this work.

I particularly express my gratitude to R. E. Falco, my advisor, for all his assistance and guidance throughout my Ph.D. program.

I would like to give many thanks to the committee members: John Foss, David Yen, Richard Bartholomew, and Daniel Nocera. In particular, John Foss gave me quite a few constructive comments on my thesis, and Richard Bartholomew helped me a lot in computer graphics.

The following people provided specific help which I appreciated: Frank Cummings' contribution to the experimental facilities, Mary Cline's proof-reading and typing, Joe Klewicki's advice on my first draft of the thesis, Sean Hilbert's fabrication of the beam divider, Kue Pan's help in computer graphics, and Chuck Gendrich's digitization of the circulation.

Many thanks to John Bracy and Scott Wixom, for their assistance in the early stages of my thesis. Also, many thanks to James Chang, Yoo Seoung-Chool, Nasser Rashidnia, Michael Hetherington, and Jeff Zenas for their friendship.

Finally, thanks to the Eastman Kodak Co. for their cooperation in preparing the photochromic chemicals and providing the information shown in Fig. 2.1.

TABLE OF CONTENTS

	page
LIST OF FIGURES	viii
LIST OF TABLES	xv
LIST OF SYMBOLS	xvi
 CHAPTER	
1. INTRODUCTION	1
2. LASER INDUCED PHOTOCHEMICAL ANEMOMETRY (LIPA)	4
2.1 Introduction	4
2.1.1 Photochromic chemical, light source and working fluid	
2.2 Technical details	5
2.2.1 Optical configuration	
2.2.1.1 Single tracer technique	
2.2.1.2 Grid tracing technique	
2.3 Algorithms to obtain fluid dynamic quantities	8
2.3.1 Single tracer technique	
2.3.2 Grid tracing technique	
2.4 Calibration and error analysis	10
2.5 Summary and comments	11
3. EXPERIMENTAL DETERMINATION OF DRAG MODIFICATIONS DUE TO ELASTIC COMPLIANT SURFACES USING QUANTITATIVE VISUAL TECHNIQUES	13
3.1 Introduction	13

3.2 Experimental details	14
3.2.1 Kerosene channel facility	
3.2.2 Flow documentation in kerosene channel	
3.2.3 Compliant surfaces	
3.2.4 Surface responses on compliant coatings	
3.2.5 Direct shear stress measurement on the walls	
3.3 Results	18
3.3.1 Flow documentations in kerosene channel	
3.3.1.1 Velocity profiles	
3.3.1.2 Pressure measurement	
3.3.2 Surface responses of compliant coatings in turbulent channel flow	
3.3.3 Shear stress measurements at walls - both stiff and compliant surface	
3.3.3.1 Results obtained from photochromic technique	
3.3.3.2 Skin friction measurement on stiff surface by hot-film anemometry	
3.3.4 Surface response on compliant surfaces associated with wall shear stress measurement	
3.3.5 Observed wave patterns on compliant surfaces	
3.4 Discussion	23
3.5 Conclusion	26
4. NEW UNDERSTANDING OF THE INTERACTIONS ASSOCIATED WITH TURBULENCE PRODUCTION: A VORTEX RING/MOVING WALL INTERACTION MODEL OF THE TURBULENCE PRODUCTION MECHANISM NEAR WALLS	27
4.1 Introduction	27
4.1.1 Background	
4.1.2 New boundary layer observations in the Turbulence Structure Laboratory, Michigan State University	
4.2 Vortex ring/moving wall interaction model	31
4.2.1 Vortex ring/moving wall simulation of the turbulence production process	
4.2.2 Experimental details	
4.2.2.1 Experimental apparatus	
4.2.2.1.1 Ring generating system	
4.2.2.1.2 Moving belt system	
4.2.2.1.3 Control system	
4.2.2.2 Visualization and recording	
4.2.2.2.1 Two-view flow visualiztion	
4.2.2.2.2 Three-view flow visualization	
4.3 Results of the interactions based on two-view flow visualization	35

4.3.1 Evolution of model	
4.3.1.1 Vortex ring moves towards wall (fast ring, $U_r/U_w > 0.45$)	
4.3.1.2 Vortex ring moves towards wall (slow ring, $U_r/U_w < 0.35$)	
4.3.1.3 Vortex ring moves away from wall (fast ring, $U_r/U_w > 0.60$)	
4.3.1.4 Far field effect	
4.3.1.5 Vortex ring moves away from wall (slow ring, $U_r/U_w < 0.45$)	
4.3.1.6 Summary of interaction	
4.3.2 Scaling associated with the interactions	
4.3.2.1 Streak spacing	
4.3.2.2 Streak length	
4.3.2.3 Wavelength associated with wavy instability	
4.3.3 Stability consideration	
4.3.3.1 Ring stability	
4.3.3.2 Streaks stability	
4.3.3.3 Comparison	
4.4 Results based on three-view visualization	41
4.4.1 Slow ring moves toward the wall	
4.4.2 Fast ring moves away from the wall	
4.5 Implication for turbulent boundary layer	43
4.5.1 Connection between vortex ring/moving wall description and the typical eddy/ wall layer interaction	
4.5.1.1 Outer region	
4.5.1.2 Inner region	
4.5.1.3 Inner/outer region interaction	
4.5.2 Streaks spacing	
4.5.3 Vortical motions associated with streaky structure	
4.5.4 Implications for drag modification	
4.6 Summary and comment	48
5. QUANTITATIVE REFINEMENT OF THE VORTEX RING/MOVING WALL INTERACTION MODEL	51
5.1 Introduction	51
5.2 Stokes' layer measurement	51
5.2.1 Introduction	
5.2.2 Experimental details	
5.2.3 Results	
5.2.4 Discussion and summary	
5.3 Vortex ring measurement	54

5.3.1 Introduction	
5.3.2 Experimental details	
5.3.3 Results	
5.3.4 Discussion and summary	
5.4 Flow visualization in kerosene tank	56
5.4.1 Introduction	
5.4.2 Experimental details	
5.4.3 Results	
5.4.4 Discussion and summary	
5.5 Velocity distribution associated with the vortex ring/moving wall interaction	59
5.5.1 Introduction	
5.5.2 Experimental details	
5.5.3 Results	
5.5.4 Discussion and summary	
5.6 Streamwise vorticity measurement associated with the vortex ring/moving wall interaction	63
5.6.1 Introduction	
5.6.2 Experimental details	
5.6.3 Results	
5.6.4 Discussion and summary	
5.7 Summary	67
5.7.1 The photochromic technique - an accurate and powerful technique	
5.7.2 Further understanding of turbulence production process through the vortex ring/moving wall interaction	
6. CONCLUSION AND FURTHER COMMENT	69
6.1 Conclusion	69
6.2 Further comment	71
FIGURES	72
APPENDIX A	168
BIBLIOGRAPHY	173

LIST OF FIGURES

Fig. 2.1	The associated absorption and emission spectrum of the photochromic chemical used in this study	72
Fig. 2.2	A schematic of the stretching of the photochromic line in shear flow	73
Fig. 2.3	The dependence of the quality of photochromic line on its orientation in shear flow	74
Fig. 2.4	A schematic of experimental configuration for one of the laser beam orientations	75
Fig. 2.5	The divergence characters of the laser beam after a F-500mm convex lens	76
Fig. 2.6	The specular reflection from the beam divider	77
Fig. 2.7	A photo of the beam divider	78
Fig. 2.8	A photo of the output of the divider showing the Fraunhofer diffraction	79
Fig. 2.9	A sketch of the optical configuration for generating a grid in Fig. 2.10 (a)	80
Fig. 2.10	A demonstration of the grid; a) shortly after the laser pulse, b) 0.4 seconds later	81
Fig. 2.11	Algorithm to obtain the wall shear stress using photochromic technique	82
Fig. 2.12	Procedure for conversion of the displacement of a grid box to velocities	83
Fig. 2.13	Decomposition of the velocities used to calculate the circulation around a grid box	84
Fig. 3.1	A schematic of the kerosene channel flow facility	85
Fig. 3.2	The dependence of the shear modulus of gelatin on the concentration of gelatin and water mixture	86

Fig. 3.3 A sketch of the experimental configuration used to capture the surface deformation under the turbulent channel flow	87
Fig. 3.4 The optical configuration of the wall shear stress measurement experiment	88
Fig. 3.5 A close-up of the technique used for the wall shear stress measurement on compliant surfaces	89
Fig. 3.6 The mean velocity profile over a stiff surface.(The centerline velocity is 0.341 m/sec yielding $Re_\theta \approx 1200$)	90
Fig. 3.7 The turbulent intensity profiles	91
Fig. 3.8 The pressure distribution along the kerosene channel at $Re_\theta \approx 1200$	92
Fig. 3.9 The onset boundary for different compliant coatings	93
Fig. 3.10 The dependence of the occurrence of each element on both K and coating thickness	94
Fig. 3.11 The histogram of the skin friction obtained from 1205 samples over the reference stiff surface	95
Fig. 3.12 The histograms of the skin friction associated with 3, 19 and 30 mm compliant coatings	96
Fig. 3.13 The combination of Fig. 3.13 (a) through (c) regardless of thickness	97
Fig. 3.14 A photo of the pocket-like depressions formed on the 3mm compliant surface	98
Fig. 3.15 The comparison of transverse length scale of depressions in compliant surfaces with the pocket footprints made on a solid surface	99
Fig. 3.16 The comparison of the time between pocket-like depressions in compliant surfaces with that obtained from boundary layer and channel flows	100
Fig. 3.17 A photo showing the triangular-shaped waves	101
Fig. 3.18 A photo of the quasi two-dimensional large-scaled waves	102
Fig. 3.19 A comparison of the visual phenomena on compliant surfaces with the flow visualization in the near wall region of channel flow by Yoda (1982)	103

Fig. 4.1 Two pockets and a pair of streaks as seen in wall slit visualization of a turbulent boundary layer using smoke as the contaminant in air, the slit is at the top of the photo and the flow is from top to bottom. (Falco 1981)	104
Fig. 4.2 The basic idea behind the simulation. Performing a Galilean transformation on the vortex ring/moving wall interaction makes in a model of the turbulent boundary production process; (a) instantaneous turbulent boundary layer; (b) simulated vortex ring/wall shear layer	105
Fig. 4.3 A schematic of the side view and end view of the experimental apparatus used in the vortex ring/moving wall simulations	106
Fig. 4.4 A schematic of the three-view visualization system; note that only the end view was illuminated by the laser sheet	107
Fig. 4.5 Sketches of the four types of local vortex ring/moving wall interactions (see text for explanation)	108
Fig. 4.6 Streaks form from the stretching of the lifted hairpin for $U_r/U_w \approx 0.8$	109
Fig. 4.7 Six photos of a vortex ring/moving wall interaction for $U_r/U_w < 0.35$ when the ring moves toward the wall at a 3 degree angle. Both plan and side views are shown. The ring and the wall are moving to the right and only the wallward side of the ring has dye in it. The interaction results in a pair of long streaks, a pocket and its associated hairpin lift-up, which then gets partially ingested into the ring	110
Fig. 4.8 Hairpins form over streaks	111
Fig. 4.9 Four photos of a vortex ring/moving wall interaction for $U_r/U_w > 0.45$ when the ring is moving away from the wall at a 2.5 degree angle. Both plan and side views are shown. The ring and the wall are moving to the right. A hairpin forms first. The long stable streaks which also form, come closer and closer together, indicating that the streamwise vorticity which caused them are of opposite sign. This evolution leads to "pinch-off" and the creation of a new vortex ring	112
Fig. 4.10 Same conditions as Fig. 4.9, except that the wall layer is very thin. We obtain long stable streaks and a long stretched hairpin which does not pinch-off over 2500 wall layer distance of the facility. The time between each photo is approximately 50 wall units	113

Fig. 4.11 Four photos of the evolution for $\delta/D > .15$. In this case a pocket does not form, and it appears that the hairpin has been generated by the initial vortex ring/wall interaction	114
Fig. 4.12 Four photos of the interaction for $\delta/D < .15$. In this case pinch-off of a portion of the lifted hairpin does occur, creating a new small vortex ring	115
Fig. 4.13 The dependence of the formations and evolutions of streaks on δ/D and U_r/U_w for $D^+ > 250$ and a 3 degree incidence angle. The indicated boundaries between different evolutions are approximate	116
Fig. 4.14 The dependence of the formations and evolutions of streaks on δ/D and U_r/U_w for rings moving away from the wall at 2.5 degrees. δ/D now plays a much more important role, and long streaks are generated over the entire speed ratio range studied	117
Fig. 4.15 The dependence of the streak spacing in wall units on the size of the vortex ring in wall units, for an incidence angle of 3 degrees and $U_r/U_w = .31$. The thickness of the wall layer (in wall units) is shown next to each data point	118
Fig. 4.16 The dependence of the streak spacing on the speed ratio and angle	119
Fig. 4.17 The non-dimensionalized streamwise wavelength that sets in as a function of δ^+ for different U_r/U_w and angles	120
Fig. 4.18 A comparison between ring and streak stability the of a three degree ring moving towards the wall	121
Fig. 4.19 The dependence of the time to instability of the streaks on the wall layer thickness (both quantities are non-dimensionalized by wall layer variables) for three degree incidence rings	122
Fig. 4.20 (a) A photo of a hairpin vortex in three-view flow visualization; (b) A sketch of the vortical motion of the hairpin vortex; note that the arrows indicate the sign of rotation	123
Fig. 4.21 Four photos of the three-view visualization; each photo is $10 t^+$ apart	124
Fig. 4.22 A conceptual picture describing the spatial relationship of the formation of visual features observed in the vortex ring/moving wall interaction including the main hairpin vortex, secondary hairpin vortices, long streaks, and pocket; the arrows indicate the local flow direction	126
Fig. 4.23 A photo showing the laser illuminated end view flow visualization for a fast ring moving away from the wall. The observed long	

streaks were just the legs of the lifted hairpin vortex; they were one unit. The dye marker actually concentrated within the streamwise vortices. The sign of the vorticity shown in Fig. 4.23 (b) is consistent with that associated with the hairpin vortex shown in Fig. 4.20 (b)	127
Fig. 4.24 The conceptual picture summarizing the spatial evolution of the vortex ring/moving wall interaction for $U_r/U_w > 0.6$ when the vortex ring moves away from the wall	128
Fig. 4.25 Comparison among several investigators' observations	129
Fig. 4.26 The distribution of D^+ obtained from the diameter of the typical eddies of a turbulent boundary layer at $R_\theta \approx 1176$, superimposed upon the streak spacing obtained for various size rings	130
Fig. 4.27 (a) The vortical motions associated with the observed streaky structure in vortex ring/moving wall simulation; (b) The counter-rotating pair hypothesized by many investigators	131
Fig. 5.1 A schematic of experimental apparatus of the Stokes' layer measurement; the moving belt system is similar to what was used in water tank	132
Fig. 5.2 The optical configuration for generating the photochromic grid	133
Fig. 5.3 The flow chart of the control system of the Stokes' layer measurement. The best orientation of the incident laser beam is also shown in this figure	134
Fig. 5.4 Two photos from the result which are 0.05 seconds apart; these photos were taken for $U_w = 12.7$ cm/sec and belt running time $t = 5.25$ seconds; the belt moved from right to left	135
Fig. 5.5 The non-dimensional velocity profile for two belt running speeds where the solid line represents the exact solution	136
Fig. 5.6 Results of the velocity gradient $\partial u/\partial y$ obtained from double differentiation and of the spanwise vorticity obtained from circulation approach are shown in this figure where they are compared with the exact solution (represented by solid line). Everything is nondimensionalized by the similarity variables of the exact solution. A check of continuity equation is also shown in this figure	137
Fig. 5.7 A schematic of the experimental configuration used to generate and measure the vortex ring	138
Fig. 5.8 The flow chart of the control system for vortex ring measurement	139

Fig. 5.9 Two photos of the result which are 0.07 seconds apart	140
Fig. 5.10 The instantaneous velocities distribution along two axes of the ring	141
Fig. 5.11 The instantaneous circulation distribution of the ring, which also shows the results obtained by Sullivan et al. (1973) for different Reynolds numbers and shows Hill's exact solution of a spherical vortex	142
Fig. 5.12 The instantaneous vorticity distribution over a vortex ring	143
Fig. 5.13 A set of photos with both top view and side view describing the time evolution of vortex ring/moving wall interactions in the conditions of $U_r/U_w = 0.26$, 3 degree of incident angle, $\delta/D = 0.18$ and $U_w = 15.5$ cm/sec	144
Fig. 5.14 By sending a single photochromic tracer parallel to the moving wall at $y^+ \approx 16$ we obtained the visual result of the interaction shown in this figure, which is the same as that obtained from the hydrogen bubble technique by many other researchers, such as Kim et al.(1971) and Smith et al.(1983)	145
Fig. 5.15 The locations of velocity measurement	146
Fig. 5.16 The details of the optical configuration	147
Fig. 5.17 The time evolution of the streamwise velocity distribution at the measurement points. The dotted lines represent the undisturbed velocity profiles of the Stokes' layer	148
Fig. 5.18 The constant velocity lines in y-z plane	150
Fig. 5.19 The velocity defect or gain with respect to the undisturbed wall layer shown in (a). These sets of data had been converted to the turbulent boundary layer point of view by performing the Galilean transformation	152
Fig. 5.20 A photo of the optical configuration and the orientation of the laser beam	154
Fig. 5.21 The side view of the data acquisition and lighting system	155
Fig. 5.22 The result of the streamwise vorticity measurement. Those photos are selected from the same sequence of movie in one experiment. Two photos of each set were 0.02 seconds apart which corresponded to $0.5t^+$ apart	156
Fig. 5.23 The contour plots of the instantaneous streamwise vorticity distribution	158
Fig. 5.24 The instantaneous Reynolds stress distribution	161

Fig. 5.25 A photo taken 0.02 seconds before $t=6.8$ seconds (shown in Fig. 5.25 (a)) indicates that a pair of counter-rotating streamwise vortices formed from the wall and moved upward.....	164
Fig. 5.26 The time evolution of total circulation of the strong vortex (the region with positive sign in Fig.5.23 (c)-(e); and the time evolution of the total circulation of one leg of the hairpin (the region with negative sign in Fig. 5.23 (c)-(e))	165
Fig. 5.27 A sketch of the pocket vortex (Falco 1980b)	166
Fig. 5.28 The sketch of possible merging process	167
Fig. A.1 The undistorted and distorted mesh	171
Fig. A.2 An example of the error analysis	172

LIST OF TABLES

TABLE 1	Local skin friction reduction.....	20
TABLE 2	Skin friction measurement from hot-film.....	21
TABLE 3	Physical scales associated with the pocket-like depressions	22
TABLE 4	Characteristics of triangular-shaped waves.....	23

LIST OF SYMBOLS

A	Area
C	Circumference
C_f	Skin friction coefficient, $(\nu \partial u / \partial y) / (0.5 U_{cl}^2)$
D	Ring bubble diameter (dye marked region)
D_o	Inner diameter of the orifice
G	Shear modulus
K	Flow speed/surface wave speed
R_θ	Reynolds number based on momentum thickness
T_d	Average time duration of a single event
T_b	Average time between events
U_r	Velocity of vortex ring in streamwise direction
U_w	Velocity of moving wall
U_{cl}	Channel centerline velocity
U_∞	Boundary layer free stream velocity
U_{TE}	Convection velocity of Typical eddy
U_c	Convection velocity of pocket-like depression
V	Total velocity (vector)
W	Transverse length scale of pocket-like depression
Z	Streaks spacing
d	Normal displacement of compliant surface
s	Displacement

t	Time
x,y,z	Spatial coordinates
u,v,w	Velocity components in x,y , and z -direction
u_τ	Friction velocity, $\sqrt{(\nu \partial u / \partial y)}$
δ	Stokes' layer thickness
ω	Vorticity
τ	Shear stress
γ	Shear strain
η	$y / 2\sqrt{\nu t}$
ν	Kinematic viscosity
θ	Momentum thickness
∂	Partial derivative
Γ	Circulation
ϵ	Grid spacing
Δ	Finite interval
λ	Wavelength
$()^+$	Non-dimensional by wall layer unit, ν/u_τ
t^*	Non-dimensional time, $t(U_w/D_o)$
ω^*	Non-dimensional vorticity, $\omega(\delta/U_w)$
$(\partial u / \partial y)^*$	Non-dimensional $\partial u / \partial y$, $(\partial u / \partial y)(\delta/U_w)$
$(\partial v / \partial y)^*$	Non-dimensional $\partial v / \partial y$, $(\partial v / \partial y)(\delta/U_w)$

CHAPTER 1

INTRODUCTION

A large number of fluid flows are difficult to measure. Examples include flows with moving boundaries, reversed flows, flows with unsteady velocity and temperature gradients, and flows in complicated geometries. In a wider class of flows only a limited amount of information can often be obtained, due to the limitations of the measurement techniques. Development of classical techniques has been underway for years in attempts to understand complicated fluid problems. The state of the art hot-wire anemometry such as Foss' vorticity probe (see Foss 1984) and Wallace's nine-wire probe (see Wallace 1986) have made it possible to acquire one point vorticity measurements; however, these techniques must invoke the Taylor's hypothesis and are limited to flows with an appropriate mean component relative to the fluctuation. Recently, Lang's (1985) four-spot LDA technique eliminated the intrusive problem, and, in principle, the need for Taylor's hypothesis and an appreciable mean velocity component. However, this technique still yields only one point, one component vorticity measurements. For many flow problems, it is desirable to obtain simultaneous multi-point measurements. These include understanding the coherent motions in many turbulent and unsteady flows, and the study of mixing in internal combustion engines. Furthermore, quantitative Lagrangian information cannot be obtained by these techniques. Thus, a technique which is able to provide the flow field information simultaneously over a region is currently needed. Laser Induced Photochemical Anemometry (LIPA) is considered a most promising technique to meet our need for the fluid dynamics measurement because it is a visual, non-intrusive, and quantitative technique, which is simple to set up and calibrate.

The objective of the present study is to demonstrate LIPA as a powerful tool in turbulent and unsteady flow problems and to extend our understanding of turbulence production and modification in boundary layers. It is hoped that the information gained will lead to a rational basis for boundary layer control. Thus, this study is a combination of both the technical development of LIPA and its application towards understanding the basic physics of the bursting process in turbulent boundary layer flows.

In chapter 2 the LIPA technique, a non-intrusive technique, will be discussed. This technique was first developed by Hummel and his co-workers (1967). With the advent of high powered excimer lasers, use of highly efficient photochemicals, and new optical designs, we are able to obtain important fluid quantities such as velocity and vorticity over a two-dimensional domain of a complicated fluid flow. The first topical study, which is discussed in Chapter 3, is to use the simplest application of LIPA to quantitatively measure the change of the skin friction in a turbulent channel flow which results from the motion of a compliant surface. The study of the surface deformation observed on the compliant surfaces leads to the next topic, the origin of the turbulence production in boundary layers. Several investigators (Kline et al. 1967, Corino and Brodkey 1969, Offen and Kline 1975, Falco 1978, 1979, 1980, Smith 1978) have presented some possible mechanisms which are responsible for the production process in the near wall region of boundary layer flows. Based upon the research which has been carried out by Falco (1974, 1977, 1979, 1980 and 1983), Lovett (1982), and Signor (1982), it has been shown that the turbulence production mechanism near a wall is closely related to the formation and evolution of a localized flow module which is created in the wall region of a turbulent boundary layer as the result of the interactions of vortex-ring-like eddies with the viscous sublayer. Further study of the vortex ring/moving wall interaction model of this process will be discussed in Chapter 4. This

model successfully simulates the turbulence production process and provides all visual features observed in the wall region of a turbulent boundary layer such as pocket (Falco 1979), a pair of low speed streaks (Runstadler et al. 1963, Offen and Kline 1975, Oldaker and Tiederman 1977, Smith 1978, Falco 1980) with the spacing about 100 wall layer units, and hairpin liftup (Falco 1982, Acarlar and Smith 1984). It also reveals the vortical motions associated with the streaky structure. To quantify the fluid quantities in such a complicated three-dimensional unsteady flow, we apply the LIPA technique. We make use of LIPA measurements of vorticity and velocity in a Stokes' layer in order to demonstrate the accuracy of the LIPA technique. The ability of this technique is revealed by the measurements of vortex ring flows. Measurements of the vortex ring/moving wall interaction in chapter 5 reveal many details of the vortex ring/moving wall interaction model and shed new light on how production takes place in the bursting process in the boundary layer flows. The physical evidence includes the velocity field associated with the bursting process, the characteristics of the low speed streaks, and the time evolution of the streamwise vorticity associated with the streaky structure.

CHAPTER 2

LASER INDUCED PHOTOCHEMICAL ANEMOMETRY (LIPA)

2.1 Introduction

Hummel and his co-workers (1967) first exploited the phenomena of photochromism (Brown 1971). Photochromism is attributed to atoms or molecules which are stable or metastable in two states and which possess different molecular or electronic configurations; i.e., having distinguishably different absorption spectra. Certain external excitations can cause the atoms to shift between the two states. Discovering this fact, Popovich and Hummel (1967) and Seely et al. (1975) used a single line of uv radiation to excite an organic liquid in which a certain amount of photochromic chemical had been dissolved. They were able to follow the discolored time line and measure one component of velocity in flows with one predominant direction of motion. Today, with the advent of highly powered uv lasers, advanced optical designs and new chemicals, we are able to extend this technique to more complicated flows.

2.1.1 Photochromic chemical, light source and working fluid

The chemical used in this study was Kodak 1,3-Trimethyl-8-nitrospiro[2-H-1-benzopyran-2,2'-indoline]. Fig. 2.1 shows the associated absorption and emission spectrum of this chemical. We excited it at 351nm using pulses of 20ns duration produced by a Tachisto Excimer laser running on XeF with approximately 100 mj output and repetition rate being adjustable from 0.1 to 100 Hz. The laser beam was 3 x 20 mm at the exit and had a divergence of 6 mrad half angle. The chemical was dissolved in the working fluid, kerosene; we found that when the chemical was excited,

it reflected blue light for a certain period of time which depended on the power of the excitation and the concentration of the chemical. Generally speaking, higher laser intensity results in a longer trace length and a darker trace color; higher chemical concentration results in a shorter trace length, a longer trace lifetime and also a darker trace color. For each experiment we controlled the concentration of the chemical to let the fluid be tagged long enough to move appreciably, so that we could obtain the required information. Usually, the concentration of the chemical ranged between 5 to 15 ppm. Since the working fluid had a low electrical conductivity, 5 ppm of anti-static agent, Shell-Sol 71, was added to increase the conductivity of the kerosene to avoid building up an electrostatic charge. The addition of the anti-static agent also increased the polarity of the testing fluid, and thus the equilibrium between the two molecular states was shifted toward the colored side. Therefore, the lifetime of the photochromic traces increased with the concentration of the anti-static agent. In principle, for the velocities of our experiments, we needed to follow the photochromic lines for only a fraction of a second to obtain the required information.

2.2 Technical details

In practice, we need only to follow one visual photochromic time line to obtain one velocity component in the flows with one predominant flow direction, and also to obtain the velocity gradient within the viscous sublayer of a turbulent boundary. However, to measure two components of the velocity in a flow using the visualization, we must tag and follow specific fluid particles. The simplest way to do this is to have two photochromic lines intersect. That intersection defines a point in the flow which we can follow. To measure a spatial gradient, we must simultaneously mark two points in the flow. In addition, we need several points and must use interpolation to measure a

spatial gradient in a prescribed direction. Thus, creation of a grid of marked intersecting fluid lines would allow us to simultaneously measure velocities and gradients in the plane on which the grid is generated. Furthermore, by integrating the velocity component along each grid box we are able to obtain instantaneous circulation and vorticity distribution in the plane of the recording media. Accordingly, we catalog the applications into two groups: single tracer technique and grid tracing technique. All the technical details and the applications of these techniques are given below.

2.2.1 Optical setup

2.2.1.1 Single tracer technique

Liang (1984) applied this technique to study the spatial growth of a Stokes' layer. For some applications, we need only one photochromic line to define the velocity gradient $\partial u / \partial y$ on the wall in a turbulent boundary layer and the velocity profiles in the unsteady flows with one predominant flow direction. However, due to the rectangular shaped cross-section of the laser beam, it depends on the local flow conditions and the orientation of the laser beam to get the best quality of the photochromic time line. For example, if we would like to obtain the velocity distribution of a two-dimensional boundary layer, the photochromic time line shown in Fig. 2.2 (a) will, of course, result in a higher resolution image than that shown in Fig. 2.2 (b). In other cases, such as measuring the mean velocity distribution in the spanwise direction of the same flow field, the orientation of the laser beam shown in Fig. 2.3 (a) will result in a better image than that shown in Fig. 2.3 (b), even though the photochromic time line is less dense in color; however, its reduced sensitivity to the local shear force of the flow will keep the photochromic time line itself from smearing.

Fig. 2.4 shows the experimental configuration for one of the laser beam orientations. The convex lens was a fused silica lens, 38.2 mm in diameter, 500 mm in

focal length, and with a transmission higher than 90% at 351 nm wavelength. The lens thinned the laser beam from 20 x 7 mm down to 0.056 x 0.160 mm at the focal point. Fig. 2.5 shows the divergence characters of the laser beam after a F-500mm convex lens.

2.2.1.2 Grid tracing technique

To enable us to measure important fluid quantities over a two-dimensional domain of a fluid flow, we have generalized the technique to uniquely tag specific points in the flow on a specific grid which can be used to obtain two velocity components and the spatial gradients of these components at a large number of points in a flow field.

We sought a method of dividing a laser beam into 'n' beams where 'n' would be 10, using a static device. In doing so, we sought to lose as little light as possible. Thus, a special divider was designed by Prof. Falco, which appears as an oversized blazed reflecting grating; the step size 'a' is approximately 2 mm. The incident laser beam was directed at a shallow angle (15 degrees) to the plane of the grating. Because the facets are so much larger than a wavelength of light, we expected to primarily see specular reflection. The separation of the specularly reflected portions of the beam was determined by the difference of the angle of incidence and the blaze angle, and the grating step width and spacing as shown in Fig. 2.6. A photo of the actual beam divider is shown in Fig. 2.7. It was fabricated by individually fixing aluminum coated mirrors to a machined base. Apart from diffraction effects, no incident laser energy would be lost. As expected, diffraction effects were exhibited in a far-field case, that is, Fraunhofer diffraction (see Hecht and Zajac). A photo of the output of the beam divider using a Helium Neon laser is shown in Fig. 2.8. We can see the specularly reflected beams and the superimposed diffraction pattern. When experiments were performed with the

Excimer laser at 351 nm in the near-field, the diffraction pattern was not observed (Fresnel diffraction). For all experiments using the photochromic grid tracing technique, we have to make sure to locate the test area away from the effect of far-field diffraction.

Fig. 2.9 presents a schematic representation of the optical setup for making a grid in Fig. 2.10 (a). The beam splitter is made by Newport Co. and designed for 351 nm wavelength. Again, the focal length of the convex lens is 500 mm. Note that the orientation of the laser beam is also based upon the same principle mentioned in the previous section. The arrangement of the optical set for different flow measurements will be discussed in Chapter 5.

2.3 Algorithms to obtain fluid dynamic quantities

2.3.1 Single tracer technique

The technique to measure the velocity component by a single incident beam path is to measure the displacement between two tracers along the mean flow direction and to divide this distance by the time interval between the two tracers. (The time interval is the reciprocal value of the laser pulsing rate.) Fig. 2.11 shows one example of wall shear stress measurement in the turbulent channel flow where t_1 and t_2 represent two instantaneous photochromic tracers in the near wall region. We choose y_0 within the sublayer and measure the distance between t_1 and t_2 which is Δs ; we know the time interval Δt between two tracers, then the velocity V will be $\Delta s/\Delta t$ at y_0 ; furthermore, the velocity gradient at the wall can be approximated as V/y_0 . This procedure can be used to calculate the displacement, velocity, and the velocity gradient.

2.3.2 Grid tracing technique

The two photos in Fig. 2.10 show the grid generated by the optical configuration shown in Fig. 2.9, which are 0.4 seconds apart, taken by a still camera with a motor drive. The mesh size is the order of 1 mm. From the distortion of the grid in Fig. 2.10 (b) in comparison to the one in Fig. 2.10 (a), (one laser pulse, two photos with Δt apart) we can calculate all the kinematic quantities of the flow in the plane of the film. Note that, in practice, we would not use a second image which has distorted as much as Fig. 2.10 (b); this is only used to illustrate the procedure.

For convenience, we choose any one 'grid box' in Fig. 2.10 (a) which, if the mesh size is small enough, can be thought as of as a textbook 'fluid particle' in a flow at time $t = 0$. This fluid particle is shown using solid lines in Fig. 2.12 (a). As this particle moves with the flow, it may undergo several motions such as translation, rotation, and deformation. The dashed lines in Fig. 2.12 (a) show the same fluid particle after a short time interval, Δt . Because we know the history of this specific fluid particle, we can compute the velocity of each corner by taking the time derivative of displacement Δs associated with each point, that is, $\Delta s/\Delta t$. The deduction procedures are shown in Fig. 2.12 (b). Note that V is designated as the velocity at point 1 which is then positioned at the midpoint between point 1' and point 1". Fig. 2.13 shows the velocity vectors deduced from Fig. 2.13. Actually, a fluid particle moving in a general three-dimensional flow field may have motions about all three coordinate axes; however, we limit the discussion to the projection of this motion onto the plane of the photos which is parallel to the initial plane of the grid.

To obtain velocity gradients, vorticity, and strain rates from the velocities, we must differentiate across the distance of a grid box. Thus, for a given flow, the grid mesh must be small enough to resolve the smallest scales of motion.

An alternative method can be used if we are interested in the vorticity. Using the

definition of the circulation Γ ,

$$\Gamma = \int_C \mathbf{V} \cdot d\mathbf{s} \quad (1)$$

and Gauss' theorem to relate the surface integral to an area integral,

$$\Gamma = \iint_A \boldsymbol{\omega} \cdot d\mathbf{A} \quad (2)$$

we can obtain the vorticity component normal to the film plane, ω_z , from a grid box of arbitrary shape, with circumference C and area A . The velocity component $\mathbf{V} \cdot d\mathbf{s}$ in Eq.(1) is estimated by forming the average of the corner velocity components (see Fig. 2.13). The dividing of Γ in eq.(2) by the area of the grid box results in the average vorticity at the centroid of this fluid particle. This approach has the advantages of avoiding a second differentiation (i.e. the differentiation of \mathbf{V} with respect to x or y) of the experimental data.

Thus, by following the distortions of a single grid box we can obtain the velocities, circulation, vorticity and even the Reynolds stress and strain rates, if desired, over that small area. By doing this for the other grid mesh points, we can obtain the important fluid dynamic quantities at many locations over a two-dimensional field in a fluid flow simultaneously.

2.4. Calibration and error analysis

The calibration of this technique depends only on a time and a length scale. In principle, we need only to have a known length scale on the film and the time interval between two films, so we are able to calculate displacement, velocity, and etc.

As far as the designated accuracy of the grid tracing technique is concerned, let us consider the grid box in Fig. 2.10 (a). Let us assume that the grid mesh is spaced ϵ

22

10
25

4

•

•

2

5

9

4

24

3

 γ^i

2

1

2

and that a worse case line movement between images is $1/2$ the mesh width. After time Δt , standard analysis (see Taylor 1972 as well as Falco and Chu 1987) shows that the uncertainty in estimating the vorticity z is

$$\delta \omega_z = (1/\Delta t)(\delta \epsilon / \epsilon)$$

to first order in ϵ . The details of this analysis are shown in Appendix A. As an example of the designed accuracy of our experiments, if we produce $100 \mu\text{m}$ lines on a grid of mesh of 1 mm , and our error in reading the center of the lines is 10% , we obtain $\delta \epsilon / \epsilon = 0.01$. For $\Delta t = 0.01 \text{ sec}$, the uncertainty in the measurement is $1/\text{sec}$. This is better than has been possible with a hot-wire probe, and is comparable with the most sophisticated four-spot laser doppler measurements (see Lang 1985).

2.5 Summary and comments

1. A non-intrusive, visual, and quantitative technique has been developed, by which we are able to measure the instantaneous fluid dynamic quantities such as velocity, vorticity, and circulation over a two-dimensional domain of a fluid flow.

2. The vorticity obtained by the photochromic grid tracing technique is the average vorticity of a small area instead of the true vorticity at one point because vorticity is a point function. All the measured vorticity mentioned in chapter 5 will represent the average vorticity of each small grid box. The direction of the average vorticity is normal to the image plane.

3. The calibration depends only on a time and a length scale.

4. Analytically, the designed accuracy is better than that with hot-wire probes, and is comparable with the most sophisticated four-spot LDA measurement.

5. The algorithms of obtaining fluid dynamic quantities involves the linear approximation. Thus, the distortion of the photochromic time line cannot be too much; usually we keep the edges of each grid box as straight as possible.

6. The ability and accuracy of this technique and the possible human errors will be tested and discussed in following chapters through the all applications in this study.

7. Further discussion and comments and improvements will be in Chapter 5 & 6.

CHAPTER 3

EXPERIMENTAL DETERMINATION OF DRAG MODIFICATIONS DUE TO ELASTIC COMPLIANT SURFACES USING QUANTITATIVE VISUAL TECHNIQUES

3.1. INTRODUCTION

Over the past few years there has been a renewed interest in the possibility of lowering skin friction drag caused by turbulent boundary layers through the use of compliant surfaces. These are surfaces that will deform under the shear stress and pressure fluctuations created by turbulence. This deformation can result in significant changes in flow properties. It has been suggested that this ability to deform the surface may inhibit the process by which turbulence is produced, thus lowering the drag. The detailed mechanism by which this will occur is not yet completely understood. To determine whether or not a compliant surface reduces the skin friction drag, only three types of measurement are possible: momentum balances, drag balances and obtaining $\partial u/\partial y$ at the wall with a non-disturbing measurement technique. Drag balance measurements have been made by several investigators for PVC based visco-elastic surfaces such as Hansen et al. (1974). On the whole, these show an increase in drag that has been attributed to the formation of static divergence waves in the surface. Recently, elastic surfaces have been investigated (Gad-el-Hak 1984). These experiments showed the formation of smaller and faster waves. However, no drag measurements have yet been attempted. In principle, no matter how accurate the drag balance measurement is, it cannot give instantaneous shear stress information, which will be needed to determine what aspects of the turbulence production process are interfered with by various wall mechanisms. Although the surface hot-film technique

and hydro

the prob

problems

ressive

books.

Section 11

The mea

and visi

in measu

see the

11. EXI

11

include

flows a

the loc

flow co

11.1 K

these

in the

the

then

flow

and hydrogen bubble technique are available to get the instantaneous information, yet, the problems of surface interference, buoyancy problems, and flow disturbance problems are still not solved, which make the results questionable. Thus, a non-intrusive wall shear stress measurement technique is needed, which can give accurate results. The photochromic technique can do this. We present the results of skin friction measurements made on an almost elastic (very low damping) compliant surface. The measurements were made possible by using the single tracer technique. It enabled us to visualize the instantaneous velocity profile in the viscous sublayer region and thus to measure the velocity gradient at the wall directly even though the surface is moving (see the discussion in the chapter about the error analysis).

3.2. EXPERIMENTAL DETAILS

Experiments were performed in a recirculating channel flow facility, which included 1) overall deformations of the compliant surfaces under turbulent channel flows at fluid to surface wave speed ratios, K , from 0 to 2.2; and 2) measurements of the local skin friction on both stiff surface and compliant surfaces under the identical flow conditions.

3.2.1 Kerosene channel flow facility

A turbulent channel flow was developed in the 5.49 m by 0.4572 m by 0.1524 m test section of a recirculating liquid flow facility, in which deodorized kerosene was used as the working fluid. The rectangular channel was designed with a 0.4 degree decline angle along the flow direction to remove any air bubble in the channel. The flow was driven by a 2 HP DC motor with a solid state power supply turning an axial pump. The flow was tripped by two 6.35 mm diameter threaded rods which were mounted at the

top and the bottom plate of the channel separately. The trip rods were located 6.35 cm downstream of a 20 mesh screen which was at the downstream end of a precise hex honeycomb. The test section hatch (50.8 cm by 25.4 cm) was fitted at the bottom plate and was 4.19 m downstream of the trips. Two viewing windows (45.72 cm by 15.24 cm) were mounted on the side walls of the channel at the test section. A 19 mm quartz laser access window was mounted flush with the top wall of the channel, allowing measurements to be made 38 cm downstream of the leading edge of the test hatch. Fig. 3.1 shows a scheme of the experimental apparatus.

The use of approximately 500 gallons of kerosene necessitated some safety precautions. Ten parts per million of the antistatic agent, Shell 71 solution, were added to prevent dangerous electrical charge buildup since the channel was typically run for several hours such that the kerosene reached equilibrium state with ambient temperature before measurements were made. The channel, storage tank and all associated equipment were grounded, and all pump motors were shielded. To achieve high quality of hot-film measurement; a filter made by Flow Tech Co. was also used to eliminate any particles in the kerosene bigger than 0.5 microns.

3.2.2 Flow documentation in kerosene channel

Velocity profiles were taken using a TSI cylindrical hot-film probe, 1210-20W, and a DISA anemometer, 55M01. The probe was bent into a five degree of pitch angle in order to get several measurements in the near wall region. The probe was calibrated at the center line of the kerosene channel flow by the photochromic single tracer technique. We averaged about 100 velocity values from photos which were taken by a Nikon camera with a micro lens and a motor drive during the probe sampling period. In all, there were ten velocity points calibrated between 0.015 m/sec. and 0.366 m/sec. The laser pulsing rate for each velocity calibration was set from 2 Hz to 25 Hz.

The two-dimensionality of the channel flow was checked from the static pressure drop measurements made at the quarter, half and three-quarter spanwise points every foot along its length. An open type kerosene manometer was used for those measurements. The details of the pressure measurement is also shown in Fig. 3.1.

3.2.3 Compliant surfaces

The compliant surfaces were made of Knox unflavored gelatin, which has been found to exhibit nearly elastic properties (see Hunston, Yu and Bullman 1984). Shear moduli G of compliant surfaces were obtained through the relationship $\tau = G \times \gamma$ where τ was the applied shear stress and γ was the shear strain carefully measured by a telescope. Fig. 3.2 shows the dependence of the shear modulus of gelatin on the concentration of gelatin and water mixture. The concentration is counted as the percentage of the weight of the powder gelatin in the water mixture. The gelatin was put in a refrigerator at 40 degrees F for six hours after it was prepared in the special tray; then we measured the shear modulus of the gelatin prior to testing it in the kerosene channel. The special trays could be inserted into the test section hatch, allowing various thicknesses to be tested. 3 mm, 19 mm and 30 mm thick surfaces were studied, which corresponded from 6 to 60 times the viscous sublayer thickness at $Re_\theta \cong 1200$. The trays were 48 cm long in the streamwise direction and 22 cm wide in the spanwise direction.

3.2.4 Surface responses on compliant coatings

Preliminary experiments were conducted to study overall surface motion characteristics of compliant surfaces under the turbulent channel flows at different Reynolds numbers. Taking advantage of the total internal reflection at the interface between compliant surface and kerosene (because the index of refraction of the

kerosene is greater than that of the gelatin), we were able to study the spatial pattern of the surface motions by visualizing the light which shone through the rear viewing window and was totally reflected at the interface. We set up a 16 mm REDLAKE high speed movie camera looking through one of the viewing windows with a 25 degree pitch angle with respect to the tested surface to capture the surface deformation under the turbulent channel flow. The sketch of the experimental apparatus is shown in Fig. 3.3. The surface deformation was recorded on EASTMAN KODAK EKTACHROME 7250 film. The framing rate varied from 100 to 400 frames/second, depending on the channel flow speed. The recorded movie was projected on a 90 by 90 cm diffused glass through a 16 mm PHOTO OPTICAL DATA ANALYZER which has the function of single frame advancing. By the superimposed calibration scale we could obtain length scales, time scales, frequencies of occurrence, and velocity scales associated with various deformation patterns.

3.2.5 Direct shear stress measurement on the walls

3.2.5.1 Measurement technique and set-up

The photochromic single tracer technique was used to measure the wall shear stress on both stiff and compliant surfaces. The laser pulses passed through the laser access window and intersected the bottom plate on the tested surfaces. Fig. 3.4 shows the optical set-up of this experiment. The laser beam was thinned by a 500 mm focal length convex lens to 150 μm at the tested wall. The photochromic time lines were viewed through a short range Questar telescope which enabled us to resolve the motions in the viscous sublayer and its adjacent region, typically, the field of view was 5 mm by 3 mm. The data was recorded by a 35 mm Photosonic high speed movie camera on Kodak TRI-X 400 film. We photographed at a framing rate that allowed two fresh photochromic time lines to be recorded on each frame. The rate of the laser pulse was

high enough to have a negligible motion of the compliant surface between two pulses.

The aluminum and gelatin surfaces were reflective enough to result in a sharp reflection of the photochromic time line. The point at which the actual photochromic time line and its image met uniquely defined the instantaneous position of the surface. This fact was used both to define the distance above the surface, and to quantify the instantaneous motion of the surface. We measured the velocity at a constant distance ($y^+ \approx 4$, where the u_τ was obtained from the hot-film measurement for stiff surface) from the surface, whether it was fixed or moving, by simply measuring the distance between two lines at our chosen distance above the current position of the wall and dividing it by the time between two pulses. Thus, the $\partial u / \partial y$ or wall shear stress value could be obtained from each frame. Fig. 3.5 shows a close-up of this technique used for wall shear stress measurements on compliant surfaces. In those experiments, a laser pulse rate of 75 Hz and camera framing rate of 25 frames/second were used. All films were analyzed on a NAC motion film analyzer which is accurate to 0.05 mm.

3.3. Results

3.3.1 Flow documentation in kerosene channel

3.3.1.1 Velocity profiles

The standard deviation of the calibration of the hot-film probe was 0.003 m/sec. Fig. 3.6 shows the mean velocity profile over a stiff surface at the same streamwise location used for the photochromic measurements taken under conditions which lead to skin friction reduction on the compliant surfaces. The centerline velocity was 0.341 m/sec yielding $Re_\theta \approx 1200$. The plot follows the Coles (1968) law of the wall. Fig. 3.7 shows the turbulent intensity profiles which match those of Eckelmann (1974).

1112 P

1

which in

of the C

from the

1112 S

which in

which in

which in

which in

which in

which in

which in

which in

which in

which in

which in

which in

which in

which in

which in

which in

3.3.1.2 Pressure measurement

The result of the pressure measurement at $Re_\theta \cong 1200$ is shown in Fig. 3.8, which indicated that there was an even pressure distribution in the spanwise direction of the channel flow and there was a smooth pressure gradient along the channel flow direction.

3.3.2 Surface responses of compliant coatings in turbulent channel flow

Preliminary experiments were performed to classify the surface responses of the gelatin at different values of flow speed/surface wave speed, K , for three coating thicknesses. Fig. 3.9 shows the stability boundary for the onset of class B waves for both gelatin and PVC plastisols obtained by Gad-el-Hak et al (1984). It indicates that the onset value of K of wave-like motion for both materials strongly depends on the coating thickness. The current visual observations of 3, 19 and 30 mm thick coatings showed that the first response of all three coatings was with local, three-dimensional, small scale, randomly oriented, and short lived deformations at approximately the same value of K , 0.6, instead of being a wave-like response. This onset response is different from that of the wave-like motion and hasn't been observed by other investigators. The insensitivity of coating thickness to this onset response supported these observation.

As we increased the values of K , we observed the change of the characteristics of the surface responses. The three-dimensional, micro-scaled, and short-lived pocket-like depression (Falco 1980 b), the intermittency of triangular-shaped waves, and the large-scaled quasi two-dimensional waves are the basic elements which constituted the surface responses of the compliant surfaces. The occurrence of each element strongly depended upon the values of K and on the coating thickness. Fig. 3.10 shows the dependence of the occurrence of each element on both K and coating thickness.

Gad-el-Hak et. al. (1984) showed that wave-like motion on the compliant coatings did increase the drag. It appears that the beneficial range of surface motions might occur between our current onset condition and the onset of the wave-like motions (class B waves).

3.3.3 Shear stress measurements at walls - both stiff and compliant surface

3.3.3.1 Results from photochromic technique

We performed experiments to measure the wall shear stress in the possibly beneficial range suggested from the visual results in sec. 3.3.2. The wall shear stresses were obtained using the photochromic single tracer technique at 4.31 m downstream of the trip rod, with centerline velocity 0.341 m/sec yielding $Re_\theta \cong 1200$. The measurement conditions associated with each different thickness are also shown in Fig. 3.9. Table 1 lists the statistical results of the local skin friction coefficient on both stiff and compliant surfaces.

TABLE 1
Local skin friction coefficient C_f

surface	K	mean	s.d.	skewness	flatness
STIFF		0.004324	0.001277	0.670	3.629
COMPLIANT	overall	0.003966	0.001295	0.685	3.413
3 mm	1.58	0.003950	0.001310	0.760	3.687
19 mm	1.37	0.003976	0.001255	0.500	2.880
30 mm	1.33	0.003973	0.001333	0.810	3.661

Figure 3.11 shows the histogram of the skin friction obtained from 1205 samples over the reference stiff surface. The curve is a lognormal distribution, which has the same mean and standard deviation as the experimental result shown in Table 1. Fig. 3.12 (a) through (c) are the histograms of the skin friction associated with 3, 19 and 30

11 00

11 10

Fig 3

11 20

11 30

11 40

11 50

12 00

12 10

12 20

12 30

12 40

12 50

13 00

mm compliant coatings. The curves are also lognormal distributions. If we combine Fig. 3.12 (a) through (c) regardless of thickness, then we will have the histogram shown in Fig. 3.13. Comparing the stiff surface (Fig. 3.11) versus the compliant surfaces (Fig. 3.13), we have an 8% reduction in skin friction coefficient.

3.3.3.2 Skin friction measurement on stiff surface by hot-film anemometer

Table 2 shows the results of local skin friction, C_f , obtained from the hot-film measurement under the same flow conditions which led to skin friction reduction on compliant surfaces. The results obtained from the photochromic technique are also shown in Table 2 as reference.

TABLE 2
 C_f measurement from hot-film

# of measurement	C_f (Clauser)	C_f (Newton)
1	0.00460	0.00379
2	0.00455	0.00388
3	0.00455	0.00376
average	0.00457	0.00381
Photochromic technique	0.00432	

3.3.4 Surface response on compliant surfaces associated with the wall shear stress measurement

Visual observation showed that three-dimensional, short-lived pocket-like depressions, which are of the order of Taylor microscale, formed on the compliant surfaces (see Fig. 3.14 photo) at the same flow condition at which we conducted the wall shear stress measurement. Those depressions were the major observed response which showed up randomly on the compliant surfaces and were bordered by crests that

extended above the mean level of the undisturbed surfaces. Table 3 lists the physical scales associated with the pocket-like depressions. Those data were obtained from the 16 mm movie mentioned in sec. 3.2.4.

Fig. 3.15 shows the comparison of transverse length scale of depressions in compliant surfaces with the pocket footprints made on a solid surface. (cf. Yoda, Falco, and Emmerling). The comparison of the time between depressions in compliant surfaces with the time between pocket-like foot prints obtained from boundary layer and channel flows is shown in Fig. 3.16 (Lovett, Eckelmann, and Thomas).

TABLE 3

Physical scales associated with the pocket-like depressions

thickness	3 mm	19 mm	30 mm	average
K	1.55	1.25	1.25	
$\log w^+$	1.92 ± 0.04	1.92 ± 0.04	1.96 ± 0.04	1.93 ± 0.04
T_d^+	30.2 ± 1.8	27.8 ± 1.8	33.2 ± 3.8	30.4 ± 2.5
T_b^+	35.8 ± 5.4	33.4 ± 4.6	30.9 ± 5.4	33.4 ± 5.1
U_c/U_{cl}	0.59 ± 0.07	0.62 ± 0.07	0.59 ± 0.05	0.60 ± 0.05
max. d	1.2 y+	1.6 y+	1.6 y+	1.5 y+
K used in C_f measurement	1.58	1.37	1.33	

3.3.5 Observed wave patterns on compliant surfaces

When the value of K was over 1.2 (for thinner coating), groups of three-dimensional triangular-shaped waves were observed intermittently. Fig. 3.17 is a photo showing this kind of wave. This phenomenon strongly depends on the thickness of the compliant coatings. It appeared at relatively lower values of K for thicker coatings. For 3 mm coating it existed at K between 1.2 and 2.1. As K was below 1.8, the pocket-like

2000

2001

2002

2003

2004

2005

2006

2007

2008

2009

2010

2011

2012

2013

2014

2015

depressions dominated the overall picture. However, those triangular-shaped waves were dominant when K was over 1.8. Table 4 shows the wavelength, half angle, wave speed, and wave numbers associated with the triangular-shaped waves in 3 mm coating at two different value of K.

As the value of K was increased, the wave patterns became quasi-two-dimensional and approached two-dimensionality for thicker coatings. Those waves were the large-scale waves with large amplitudes traveling at about 50% of the channel center-line velocity, they looked like the class B waves which were observed by Gad-el-Hak et al. Fig. 3.18 shows a photo of these quasi two-dimensional large-scaled waves.

TABLE 4
Characteristics of the triangular-shaped waves

flow speed/surface wave speed, K	1.80	2.07
wavelength/coating thickness	2.89 ± 0.35	3.50 ± 0.31
half angle (degree)	46.7 ± 3.0	52.1 ± 3.3
wave velocity/flow velocity	0.73 ± 0.02	0.72 ± 0.03
wave numbers	2.43 ± 0.56	3.34 ± 0.80

3.4. Discussion

The lateral scale of the pocket-like depressions is about 60 times the height of the surface movement, so that if a probe was positioned in the wall, it would severely inhibit these motions of the compliant surface. The photochromic technique is a reliable tool to obtain the wall shear stress on compliant surfaces nonintrusively and accurately.

The average reading uncertainty obtained from different readers during the data reduction process through a motion film analyzer was 3%, which was mainly a result of

human error. Through the use of digital image processing equipment, this uncertainty can be reduced. The maximum error associated with the $\partial u/\partial y$ measurement caused by the movement of compliant surface was 4%. This error was estimated by the maximum vertical displacement on compliant surfaces between two photochromic time lines. It is reasonable to use the lognormal distribution to estimate the mean of the error which is due to the surface movement because the wall shear stress has a lognormal distribution. Thus, the mean of the error in calculating $\partial u/\partial y$ is about 1.5%.

Results of hot-film measurement were different from those obtained using the photochromic technique. The result obtained using Clauser plot based on Coles (1968) universal law is about 5% higher than that obtained using the photochromic technique. The reason for this difference may possibly be attributed to measurement error or the favorable pressure gradient of the channel flow which was not fully developed.

The value of $\text{rms}(\partial u/\partial y)/\text{mean}(\partial u/\partial y)$ was 0.295 on the stiff surface measurement; this indicates that the measurement was in agreement with several investigators such as Mitchell & Hanratty (1966) and Eckelmann(1974).

In comparing the two histograms in Fig. 3.11 and Fig. 3.13, the compliant surfaces did change the characteristics of the statistical results on skin friction distribution. Interestingly, it shows that only the high probability events have been changed and the skewness and flatness almost stay the same.

The only other study of elastic surfaces known to the author is that of Gad-el-Hak et al.(1984). He found that two-dimensional waves set in at values of K (approximately 3.5, for a 3 mm thick surface) higher than those for which we found a three-dimensional pattern. The reason for the differences are not known, but earlier, Falco, Chu and Wiggert (1983) also observed a three-dimensional pattern developed in

be same

waves of

microsc

does be

length

depress

low as

among

phenom

decrea

three

charac

surface

of K

bound

comp

proton

three

charac

which

decre

the same compliant material in a water channel test before the onset of large amplitude waves of the type found by Gad-el-Hak et al.

It appears that the response we have found is a response of the surface to the microscale eddies of the turbulence, which, at least in these preliminary experiments, does lead to skin friction reduction. More evidence on this is shown in Table 3; the length scales, the velocity scales and the time scales associated with the pocket-like depressions correlate very well with those of the bursting process in a turbulent channel flow and boundary layer flow. Fig. 3.15 and Fig. 3.16 show a very good agreement among the comparisons. Fig. 3.19 shows the further comparison between the visual phenomena on compliant surfaces and the flow visualization in the near wall region of channel flow by Yoda (1981). Apparently, they look similar.

Interestingly, we obtained almost the same amount of skin friction reduction for three different thickness coatings at the operating conditions. It may suggest that the characteristics of turbulence being modified during the interaction with the compliant surfaces has weak dependence on the thickness of the coating, when the operating value of K is slightly above our current onset boundary and is significantly below the onset boundary of class B waves. If this modification were created by wave motions on compliant surfaces, then the dependence on the coating thickness should be pronounced.

From Fig. 3.9 we also can see that for thinner coatings there is a wider range of three-dimensional surface deformation before the onset of quasi-two-dimensional surface motions. Thus, thinner coatings should have a wider operating range over which skin friction reductions are possible. Further experiments are needed to determine the range of applicability of these results.

As far as the triangular-shaped waves are concerned, their half angles,

wavelengths and wave numbers increased as the value of K went up. Eventually, the half angles reached to 90 degrees and the waves became two-dimensional, which had large amplitude and wavelength spreading over the whole compliant surface. Those large scale waves were close to class B waves observed by Gad-el-Hak et al., which travelled at about 50% of the channel center line velocity.

3.5. Conclusions

1. A non-intrusive quantitative photochromic single tracer technique has been used to measure the skin friction both on a stiff surface and on compliant surfaces. The error of this technique is about 4.5% plus sampling error.

2. Eight percent (8%) skin friction reduction has been found on low damping elastic gelatin.

3. Histograms of skin friction distribution are lognormal for both stiff and compliant surfaces.

4. The observed onset response on currently used compliant surfaces was local, three-dimensional, small scale, and short lived deformation at approximately the same value of K , 0.6, for three different thicknesses.

5. In conditions which lead to skin friction reduction, the surface responses show the characteristics of turbulence. The measured length scale, time scales and velocity scale associated with the observed pocket-like depressions correlate very well with those of the bursting process in wall bounded turbulent flows.

CHAPTER 4

NEW UNDERSTANDING OF THE INTERACTION ASSOCIATED WITH TURBULENCE PRODUCTION: A VORTEX RING/MOVING WALL INTERACTION MODEL OF THE TURBULENCE PRODUCTION MECHANISM NEAR A WALL

4.1 Introduction

In the previous chapter we studied the surface responses of the compliant surfaces associated with the skin friction measurement and compared those with the bursting process in wall bounded turbulent flows visually (see Fig. 3.19) and quantitatively (see Table 3, Fig. 3.15, and Fig. 3.16). We concluded that at low forcing levels where C_f reduction was found, the response of compliant surfaces is a response to turbulence. Accordingly, we ask ourselves a question, "What mechanism is responsible for creating pocket-like deformations on compliant surfaces and also for rearranging a dye marker to create the structural features in the near wall region of rigid wall bounded turbulent flows (see Fig. 3.19)?" We focus on this point in this chapter and the following chapter.

There is a need to construct both experimental and numerical simulations of the turbulence production process near walls, because of the difficulty of isolating mechanisms when experiments are conducted in the boundary flows. A good simulation must embody the essential features of the production process. Several investigators (Kline et al. 1967, Corino and Brodkey 1969, Offen and Kline 1975, Falco 1978, 1979, 1980, Smith 1978) have presented some possible mechanisms which are responsible for the production process in the near wall region of boundary layer flows. In this chapter we present a moderately extensive review of the important structural features associated with the wall region events as well as the new boundary layer observations

observed in Turbulence Structure Laboratory, Michigan State University (Falco, Lovett, and Signor), that helps complete the picture of structural feature interactions. Then we present the vortex ring/moving wall simulation experiments that model all of the important properties.

4.1.1 A review of the important structural features associated with the wall region events in boundary layer flows

Turbulent boundary layer structure that should be modeled includes the long streaks (Runstadler et al. 1963), the pockets (Falco 1980a, 1980b), the hairpins (Falco 1982, Acarlar and Smith 1984), the Typical eddies (Falco 1977, 1983), and coherent regions of streamwise vorticity and/or streamwise vortices. Basically, these structural features have been shown to be associated with the production process, but the formation of the structures and the interactions are not completely understood. A number of investigators have studied the formation of low speed streaks. Oldaker and Tiederman (1977) observed that a pair of low speed streaks formed as a result of the response to what appeared to be a sequence of local high speed outer region eddies interacting with the wall and aligned along a streamwise direction. The path left by the outer region disturbances clearly formed a high speed streak. Falco (1980a) observed the formation of low speed streaks in pairs by a similar mechanism. Although low speed streaks are often observed to exist singly, care must be taken when interpreting low speed streak formation, because once formed the low speed streaks can persist for very long times (Smith and Metzler 1983), and the undisturbed passive dye marked region will simply convect into the observation zone.

Since the mid fifties, it has been suggested that long counter rotating streamwise vortices exist in the wall region and that pairs of these vortices produce a gathering of wall layer dye between them that we see as the low speed streaks. A high speed streak

would be the result of high speed fluid being induced towards the wall between a pair of these streamwise vortices rotating the other way. A number of authors have suggested causes for these streamwise vortices. Currently, the most popular suggestion is that they are the 'legs' of hairpin vortices that are also observed in the wall region. However, as Acarlar and Smith (1984) have pointed out, it is very hard to understand how the hairpin legs could extend upstream as far as would be necessary to produce streaks of length $x^+ = O(1000)$. Thus, there is still no experimental evidence supporting the various rational physical hypotheses describing the formation of long streaks.

Another feature of the wall region structure is the frequent rearrangement of marker that moves it away from a local region, leaving a scoured 'pocket' of low marker concentration. Fig. 4.1 shows two pockets as seen in a layer of smoke marked sublayer fluid. Pockets are footprints of outer region motions that interact with the wall. Falco (1980a) showed that they start out as a movement of wall layer fluid away from a location as a high speed outer region eddy (a typical eddy, discussed below) nears the wall. The interaction results in the footprint opening up into a developed pocket shape. Fluid is seen to lift-up from the downstream end of the pocket, and take on the characteristics of a hairpin vortex (Falco 1982).

Vortex lines are constantly being bent in turbulent boundary layers. Although flow visualization of a passive contaminant cannot be used to observe vorticity directly, dye marked features in the wall region that appear to be hairpin vortices have been observed by Falco (1982) and Smith et al. (1983). We have observed hairpins appearing to form over individual streaks. The streak is seen to become lumpy, and one of the lumps grows and a hairpin emerges from it. Acarlar and Smith (1984) have also observed hairpins growing over simulated streaks, and, it appears, in a turbulent

boundary layer.

The microscale coherent motions observed across a turbulent boundary layer, which are similar to laminar vortex rings embedded in a shear flow, are called Typical eddies. They have been studied by Falco (1974, 1977, 1982, 1983), who showed that they contribute significantly to the Reynolds stress in the outer part of the boundary layer, and that they are the excitation eddies that create the pockets. Experiments using two mutually orthogonal sheets of laser light enabled Falco (1980b) to determine, as far as the smoke marking allows, that the coherent feature was a ring, as opposed to a portion of a hairpin vortex, as suggested by Head and Bandyopadhyay (1981).

Both types of hairpin creation mechanisms described above can produce hairpins that can pinch-off and form new vortex rings. Falco (1983) showed visual evidence of a hairpin lifting from the downstream end of a pocket, contorting and pinching off to form a new vortex ring-like typical eddy. This pinch-off mechanism has also been clearly shown to occur in the calculations of Moin et al. (1986) mentioned above.

Many investigators have noted the presence of streamwise vortices in the wall region. Almost without exception, the vortices have been of short extent (Praturi and Brodkey 1978, Falco 1980b, Smith 1982). A number of investigators have suggested that streamwise vortices of much greater extent exist in the wall region essentially laying just above the wall in pairs, which are responsible for the creation of both low and high speed streaks. This evidence is of a statistical nature, usually from correlation measurements. However, no one has ever observed them, and recent calculations of turbulent channel flow using the full Navier-Stokes equations (Kim 1986) have shown that the eddies which have streamwise vorticity are not elongated in the streamwise direction.

4.1.2. New boundary layer observations in the Turbulence Structure Laboratory, Michigan State University

The major discovery is that as a typical eddy convects over the wall, it causes an interaction that results in the formation of a pair of long streaks. If the typical eddy is convecting towards the wall, when it gets close enough, it will create a pocket, and have one of four types of interactions defined below. The creation of the long streaks occurs even when the typical eddies are quite distant from the wall, well into the log region.

Observations mentioned above have indicated that hairpin vortices can form as a result of pocket evolution and as a result of lumping instability of existing low speed streaks. They also found that there were occurrences where neither of these mechanisms appeared to be the cause. They also identified another mechanism that can result in the formation of hairpin vortices. When a typical eddy is moving away from the wall at a shallow angle and when it is moving relatively slowly, say $U_c/U_\infty < 0.4$, it will create a pair of long very stable streaks that trail behind a hairpin vortex that lifts up slowly. The eddy can be as far from the wall as indicated above, and thus, will convect appreciably downstream before the hairpin will be noticed. It may convect out of the field of view, leaving the observer with the impression that the formation of the hairpin did not involve the coherent motion.

Thus, only one coherent motion, interacting with the wall, is necessary to create both the long streaks and the pockets; since the remaining structures found in the wall region are related to these two structures. The visual results suggested that the typical eddy be responsible for the onset of the turbulent production process.

4.2 Vortex Ring/Moving Wall Interaction Model

4.2.1 Vortex ring/moving wall simulation of the turbulence production process

Accordingly, we can simulate the interaction of a typical eddy with the wall region of a turbulent boundary layer by creating a vortex ring and having it convect towards or away from a moving wall. Fig. 4.2 shows the basic idea behind the simulation. The vortex ring can be aimed at or away from the wall at shallow angles. Both the wall and the ring move in the same direction. The Reynolds numbers based upon the initial ring velocity and diameter of the dyed ring bubble, D , ranges between 600 and 2000. When created away from walls, these rings remain stable to azimuthal instabilities over durations longer than those used in the interaction experiments. By performing a Galilean transformation on the simulation, we recover the essential aspects of the typical eddy wall region interaction in a turbulent boundary layer flow.

For convenience, we have used an impulsively started moving belt. It has the advantages of being an exact solution of the Navier-Stokes equations (Stokes' first problem), and therefore is well defined. Furthermore, the velocity profile is approximately linear in the wall region which is similar to the mean velocity profile of the viscous sublayer of a turbulent boundary layer. It is relatively easy to match the friction velocity in these simulations with those found in low Reynolds number turbulent boundary layers.

4.2.2 Experimental details

4.2.2.1 Experimental apparatus

Experimental simulations were performed in a water tank which is 40.5 cm deep by 32.4 cm wide by 243.8 cm long. Fig. 4.3 shows the side view and end view of the experimental apparatus which includes a vortex ring generating device, a moving belt and driving arrangement, a synchronizing timer, and visualization recording devices.

4.2.2.1.1 Vortex ring generating device

The vortex ring generating device includes a constant head reservoir from which fluid, which could be dyed, passes through a solenoid valve whose opening time could be varied, and an orifice of prescribed size (see Fig. 4.3 items 1,2,3). The constant head reservoir (item No. 1) is filled with a mixture of 10 ppm Fluorescent Sodium Salt Sigma No. F-6377, green dye and water solution. As the solenoid valve (No. 2) opens, a slug of dyed fluid is released from the orifice (3) by the pressure head, and rolls up into a vortex ring. Three different inner diameters of the orifice have been used; 2.54 cm, 1.27 cm, and 0.95 cm. The size and speed of the vortex ring generated depends upon both the height of the dye reservoir and the opening duration time of the solenoid valve for a fixed orifice. The details have been presented in Liang (1984).

4.2.2.1.2 Moving belt and driving device

The wall upon which the vortex ring interacted is a moving belt (4) made of transparent plastic which has a smooth surface. Two ends of the belt are joined together to form a loop, which circulates around two rollers (5) as shown in Fig. 4.3. The width of the belt is 17.8 cm; and the distance between the two rollers is 152.4 cm. The test section is at 76.2cm downstream from one of the rollers, giving us a Stokes' layer for this distance (if the belt is run longer in time, the leading edge effects begin to enter into the problem). This width/length ratio is sufficient to prevent the disturbances generated in the corners from reaching the center of the belt at the test section. Therefore, the wall layer flow on the moving belt could be considered one-dimensional. One of the rollers is driven by a 1/4 HP DC motor (6). The speed of the belt is adjustable within the range of 2.5 cm/sec. to 22.9 cm/sec. The belt reaches a constant speed very soon (within a second) after power is turned on. This short acceleration period allows us to consider the belt to be impulsively started. As the belt moves, a Stokes' layer builds up on the belt. A mixture of red food coloring and water is used to mark the wall layer for visualization. The belt is covered with dye before each run

during a 'dye run' using a dye injector near the leading roller of the belt, shown in Fig. 4.3 (7). The fluid is allowed to come to complete rest before each 'data run'.

4.2.2.1.3 Control system

The opening duration time of the solenoid valve, and the time delay between the onset of the belt movement and release of the vortex ring are controlled by a 115 VAC/60 Hz timer designed in the laboratory. Since the thickness of the Stokes' layer, δ , is a function of the square root of the belt run time, that is, $\delta = 4.0 \sqrt{\nu t}$, by carefully adjusting the time delay, we can adjust δ/D as desired.

4.2.2.2 Visualization and recording

4.2.2.2.1 Two-view visualization

The primary visual data consisted of simultaneous plan and side view time resolved images which were collected using a standard video camera, a VCR, and a monitor, and are shown in the end view of Fig. 4.3. The side view was often illuminated by a laser sheet emitted from an 8 W Coherent CR-8 Supergraphite Argon Ion Laser. The visual data were analyzed on a high resolution monitor with a superimposed calibrated scale, using the slow motion capabilities of the recorder.

A 35mm Photo-Sonic movie camera and a 16mm Redlake high speed movie camera were also used to record high resolution images of the interactions on Kodak ASA 400 color negative film and Kodak Ektachrome 7250 film respectively. The data acquisition system is the same as that shown in Fig. 4.3

4.2.2.2.2 Three-view visualization

A simultaneous three-view data acquisition system was designed in order to resolve the vortical structure associated with the vortex ring/moving wall interaction in the plane which is perpendicular to the mean flow direction Fig. 4.4 shows the scheme of the three-view visualization system; note that only the end view was illuminated by

the laser sheet. The image of the laser illuminated end view was sent to the top view collecting mirror through a front coating flat mirror. This is shown in both views of the set-up in Fig. 4.4.

4.3 Results of vortex ring/moving wall interactions based on two-view flow visualizations

We will describe the model in terms of the velocity ratios and spatial relationships of the simulation. Later in the discussion, we will invoke the Galilean transformation to relate the findings to the turbulent boundary layer case.

4.3.1 Evolutions of the model

4.3.1.1 Fast rings ($U_r/U_w > 0.45$) moving towards the wall with a shallow angle (3, 6, and 9 degree)

Interactions which result from these rings have been described by Liang et al. (1983). They result in the formation of a pocket, and varying degrees of lift-up of wall layer fluid. The interactions have been divided into four types. Fig. 4.5 shows sketches of the four types of interactions. Type I results in a minor rearrangement of the wall layer fluid; followed by the ring moving away from the wall essentially undisturbed. Type II (same as described for boundary layer interactions) results in a well defined lift-up of wall layer fluid, which takes on a hairpin configuration. This fluid does not get ingested into the ring, and the ring moves away from the wall as a perturbed but stable ring. The hairpin has been observed to pinch-off or just move back down towards the wall and lose its identity. Type III results in a lifted hairpin of wall layer fluid which gets ingested into the ring, resulting in a chaotic breakdown of both the lifted hairpin and the vortex ring, as the vortex ring is moving away from the wall. Type IV also initiates a hairpin vortex, but in this case the hairpin vortex is ingested into the ring on a much

shorter timescale, and the ring and lifted wall layer fluid both breakdown while the ring is very close to the wall.

Liang et al. used vortex rings with $D^+ > 250$ and δ^+ between 20 and 50, and they observed only the above four types of interactions. Current experiments indicate that if $D^+ < 150$ and δ^+ is between 20 and 50, we can also obtain the four types of interactions noted above, but, in addition, we found that long streaks also formed. In these cases, a hairpin grew out of the open end of the pocket, its legs stretched and a pair of streamwise streaks formed along the hairpin legs (see Fig. 4.6). The streaks grew to several hundred wall units. This observation is in contrast to the suggestions of a number of investigators that a lifted hairpin vortex would induce a single streak to form between its legs.

4.3.1.2 Slow rings ($U_r/U_w < 0.35$) moving towards the wall at a shallow angle (3, 6, and 9 degree)

These initial conditions result in a pair of long low speed streaks, $x^+ = O(1000)$, a pocket, and hairpins which induce themselves and portions of the streaks to lift-up. Fig. 4.7 shows six photos of this happening prior to the onset of a Type III interaction. We can see the formation of the pair of low speed streaks, followed by the formation of the pocket, and the associated hairpin lift-up, then partial ingestion of the pocket hairpin. The ring later breaks up. The streaks that form under these conditions become wavy and slowly breakdown resulting in additional lift-up and transport. Hairpins have been observed to form over these streaks (see Fig. 4.8). The initial conditions are two-dimensional. The moving belt is started from rest, so that the layer approximates a Stokes' layer. These streaks have obviously not formed as the result of the pre-existence of streamwise vortices, but spanwise vorticity has been distorted to give a streamwise component, and it is clear from the Navier Stokes equations that new streamwise vorticity has also been generated at the wall.

4.3.1.3 Fast rings ($U_r/U_w > 0.45$) moving away from the wall at a shallow angle (less than 3 degrees)

These initial conditions result in a hairpin vortex which is linked to the distributed streamwise vorticity that has formed a pair of long, very stable, low speed streaks. A pocket is not observed. The evolution of the hairpin in this case has been observed to lead to the pinch-off of this hairpin, forming a vortex ring, and another hairpin. Fig. 4.9 shows four photos of the evolution leading to the creation of a new vortex ring. The long stable streaks which form come closer and closer together, indicating that the streamwise vorticity which caused them, and which is of opposite sign, is being stretched and brought very close together. Diffusion is accelerated, and the vorticity is redistributed into a vortex ring and a hairpin loop. Fig. 4.10 shows long stable streaks and a long stretched hairpin which does not pinch-off over the distance available due to size limitations of the experimental facility--more than 2500 wall layer units. There are two initial conditions that may cause this kind of long stretched streamwise vorticity to evolve into a hairpin: 1) δ/D is very small; 2) the ring is far away from the wall. Further study concerning the effects of ring to wall distance is needed.

4.3.1.4 Far-field effect (fast ring, $U_r/U_w > 0.6$, moves away from the wall at a shallow angle)

The far field effect could happen even though the edge of the lower lobe of the vortex ring is around $120 y^+$ above the wall. A long stretched hairpin was observed to form which had the same shape as that shown in Fig. 4.10, however, the spacing between the two legs became narrower as the distance between the ring and the wall became larger.

4.3.1.5 Slow rings ($U_r/U_w < 0.45$) moving away from the wall at a shallow angle (less than 3 degree)

These initial conditions result in a hairpin from which a pair of long stable low speed streaks emerge. A pocket is also not observed. The phenomenon of hairpin

pinch-off, for this case, appears to depend upon δ/D . If $\delta/D < 0.15$ we get pinch-off, but only a part of the fluid involved in the hairpin is observed to pinch-off and form the ring. If δ/D is greater, and the ring moves away from the wall without ingesting any wall layer fluid (Type I or II), the lifted hairpin appears to do very little. Fig. 4.11 shows four photos of the evolution for $\delta/D > 0.15$. In this case a pocket does not form, and it appears that the hairpin has been generated by the initial vortex ring/wall interaction, and that a pair of streamwise vortices--which could be called its legs--trail behind, creating the streak pair. Pinch-off does not occur. Fig. 4.12 shows four photos of the interaction for $\delta/D < 0.15$. In this case pinch-off of a portion of the lifted hairpin does occur creating a new small vortex ring.

4.3.1.6 Summary of interactions

A summary of the vortex ring/wall interactions which result in streak formation and evolution is shown as a function of the parameters U_r/U_w , δ/D , and ring angle in Fig. 4.13 and 4.14. Fig. 4.13 shows the dependence of the formations and evolutions of streaks on δ/D and U_r/U_w for $D^+ > 250$ and a 3 degree incidence angle. The indicated boundaries are between different evolutions and are approximate; additional data are necessary to precisely locate their positions. The available information suggests that the streak development is essentially not dependent upon δ/D . Furthermore, the long streaks are only observed to form for speed ratios less than approximately 0.35. Fig. 4.14 shows the dependence of the formations and evolutions of streaks on δ/D and U_r/U_w for rings moving away from the wall at 2.5 degrees. δ/D now plays a much more important role, and long streaks are generated over the entire speed ratio range studied.

4.3.2 Scaling associated with the vortex ring/moving wall interactions

From our perspective of a turbulence production model, the streak spacing,

streak length and wavelength of the streak instability are quantities of interest.

4.3.2.1 Streak spacing

Fig. 4.15 shows the dependence of the non-dimensional streak spacing on the size of the non-dimensional vortex ring, for an incidence angle of 3 degrees and $U_r/U_w = 0.31$. The thickness of the wall layer (in wall units) is shown next to each data point. The streak spacing, Z^+ , is within 10% of the ring diameter for wall layer thicknesses between 20 and 50 wall units. Results shows that decreasing U_r/U_w will decrease the average streak spacing relative to the ring size for fixed incidence angles. Furthermore, increasing the incidence angle of the vortex ring will increase the average streak spacing for a given ring size and speed ratio. Fig. 4.16 shows the dependence of the streak spacing on the speed ratio and angle.

4.3.2.2 Streak length

Measurements show that streak lengths greater than $x^+ = 500$ were obtained for many of the interactions in ranges where the streaks are stable (for rings with $D^+ = 100$, streaks as long as $x^+ = 1000$ were found).

4.3.2.3 Wavelength associated with wavy streak instability

Fig. 4.17 shows the non-dimensionalized streamwise wavelength that sets in as a function of δ^+ for different U_r/U_w . The wavelength is the same order as the ring diameter. It decreases as the ring/wall speed ratio.

4.3.3 Stability considerations

4.3.3.1 Vortex ring stability

Some additional data has been obtained, which confirms and extends the results of Liang (1984), showing that the boundary between stable ring wall interactions (Types I and II), and unstable interactions (Types III and IV) depends upon δ/D . Fig. 4.18

shows a stability map of the interactions for 3 degree rings. We can see that for low ring/wall speed ratios, the ring stability depends primarily upon the relative thickness of the wall layer and the size of the ring; for thicker wall layers or smaller rings, the interactions are more stable. Furthermore, the shallower the incidence angle the more stable the interaction.

4.3.3.2 Stability of the streaks

Fig. 4.19 shows the dependence of the time onto instability (i.e. the time from the formation of the streaks to the first observation of the wavy instability) of the streaks which exhibited wavy instability on the wall layer thickness (both quantities are non-dimensionalized by wall layer variables) for 3 degree incidence rings. We can see that for each convection velocity ratio, there is a value of δ^+ above which the time to instability becomes much longer.

4.3.3.3 Comparison between ring and streak stability

Both the rings and the streaks are more stable when the wall layer is thicker. Fig. 4.18 shows a comparison of the stability boundaries of a three degree ring moving towards the wall, with the stability boundary of streaks formed by those same rings. The streak stability boundary has generally the same shape; stable rings will, in general, correspond to stable streaks, except for a small range of δ/D . The ring stability curves and the streak stability boundary curves for different size rings collapse when plotted this way.

The streak formation boundaries in this figure represent the boundaries between conditions that will enable a pair of long streaks to form. For δ/D below the boundaries, we have a very unstable situation in which the fluid in the region around the eddy seems to rearrange itself into the beginnings of a streak, but the streak pair is not stable, and immediately breaks up. For δ/D values above the boundaries, a pair of

long streamwise streaks form. However, once formed, the streaks are susceptible to breakdown by the wavy or lumpy instabilities noted above, where the time to instability is a function of angle, convection velocity, and the instantaneous wall layer thickness (for example, see Fig. 4.19).

4.4 Results of the vortex ring/moving wall interactions based on three-view visualization

By accessing the laser illuminated end view we were able to realize the streamwise vortical structure associated with the vortex ring/moving wall interaction. We will discuss the interactions which were observed the most in the turbulent layer, that is, the interactions in which a pair of long streaks were observed as being either stable or unstable.

4.4.1 Slow rings ($U_r/U_w < 0.35$) moving towards the wall with a shallow angle (3 degree)

The conditions of the case discussed here are shown as point 'A' in Fig. 4.18. These initial condition result in a main hairpin, a pair of low streaks $x^+ = O(1000)$, a pocket, and hairpins induce themselves and portions of the streaks to lift-up. By sending the laser sheet to different locations we were able to resolve the vortical structure at different parts of the interaction.

The main hairpin was observed to form first; the sign of the hairpin vortex is shown in Fig. 4.20. Evidently, it was a vortex loop; the core is about $5-10y^+$ and the distance between two legs was about $50-60 z^+$ in the spanwise direction. This hairpin vortex was the wall layer fluid induced and lifted up by the lower lobe of the vortex ring. After the hairpin vortex was lifted up from the wall, it was stretched and diffused. The visual evidence showed that this hairpin vortex lasted about $50 t^+$. Even though we still

can visual the organized dye marker associated with the lifted hairpin at the later stage of the vortex ring/moving wall interaction, however, the laser illuminated end view suggested that there was not much vortical motion in this hairpin vortex.

Fig. 4.21 shows the evolution of the vortex pair which was observed to be associated with the streaky structure. There are $10 t^+$ between photos. As this vortex pair induced itself up, it was getting bigger and bigger and its size could be about $25-30 z^+$ extending about $200-300 x^+$ in the near wall region ($y^+ < 10$). The three-view visualization showed that even before the streamwise vorticity, x , rolled into vortices, the top view had already shown the wall layer dye marker being gather together to form streaks (see Fig. 4.21 (b)). After the vortex pair was observed to form, it induced itself up and broke up. This quick lifting and breakup lasted only about $20 t^+$. Mainly, the dye marker associated with the observed breakup was from this vortex pair. Only the top view could not tell the difference between the streamwise vortices and the long streaks. Fig. 4.21 (b) shows clearly the evidence of the formation of the secondary hairpin vortices over streaks; especially in the region near the pocket.

Three-view visualization also showed that as the pocket vortex (Falco 1980b) entered into the viewing window (laser illuminated end view), suddenly, the lifted vortex pair was turned inward in the rotating direction of the pocket vortex (Falco 1980b). This inward motion caused the lifted vortex pair to break-up. However, there was no dye marker present in the vortical structure of the pocket vortex. One possible reason for this may be due to the dye marker which had been pushed away to form streaks in the earlier stage of the interaction.

Based upon the results of three-view visualization on vortex ring/moving wall interaction model, we summarize the interaction into one picture. Fig. 4.22 shows a conceptual picture describing the spatial relationship of the formation of visual features

observed in the vortex ring/moving wall interaction including the main hairpin vortex, secondary hairpin vortices, long streaks, and pocket; the arrows indicate the flow direction.

4.4.2 Fast rings ($U_r/U_w > 0.6$) moving away from the wall with a shallow angle (less than 3 degree)

Fig. 4.23 (a) is a photo showing the laser illuminated end view visualization under the those initial conditions. The observed long streaks were just the legs of the lifted hairpin vortex; they were one unit. The dye marker actually concentrated with the streamwise vortices. The sign of the vorticity shown in Fig. 4.23 (b) is consistent with that associated with the hairpin vortex shown in Fig. 4.20 (b). Fig. 4.24 shows the conceptual picture summarizing the spatial evolution of this type of vortex ring/moving wall interaction.

4.5 Implications for turbulent boundary layers

4.5.1 Connection between vortex ring/wall layer description and the typical eddy/wall layer interaction

4.5.1.1 Outer region of turbulent boundary layer

To interpret the results of the vortex ring/moving wall interactions in terms of turbulent boundary layer interactions, we must perform a Galilean transformation on the velocity field. Our interpretation of the simulation has been to identify the Stokes' layer with the viscous wall region which extends to y^+ approximately 30-50. The mean velocity at this height is approximately 70 - 80% of U_∞ . Thus,

$$U_{TE}/U_\infty = a(1 - U_r/U_w)$$

where 'a' represents the outer region velocity defect which we can not simulate

(20-30%). Thus, in thinking about the implications for the turbulent boundary layer, basically high speed ratios in the simulations correspond to low convection velocities of the typical eddies in the boundary layer.

4.5.1.2 Inner region of turbulent boundary layer

As far as the shear condition in the near wall region is concerned, we can estimate the velocity gradient at the wall by using the exact solution of Stokes' layer. The velocity of the moving wall used in the vortex ring/moving wall interactions ranges from 0.076 m/sec to 0.152 m/sec which corresponds to 0.65 to $0.25 U_r/U_w$ or 0.35 to $0.75 U_{TE}/U_\infty$, and the belt running time is between 2 and 6 seconds: resulting in the ratio of the friction velocity to the wall velocity, u_τ/U_w , is between 5.5% and 3.5%. This range of the friction velocity is very close to what is found in low Reynolds number boundary layer flows. However, due to the unsteady nature of the Stokes' layer, for each fixed velocity of the moving wall, the percentage of u_τ/U_w decreases monotonically during each experiment. This variation in u_τ/U_w is approximately 1% over the course of any given experiment. This is slightly different from the real situation in the near wall region of turbulent boundary layer where the friction velocity is stochastically stationary.

4.5.1.3 Inner/outer region interaction

As a result, we expect the typical eddies that emerge from wall layer fluid (through a pinch-off of lifted hairpin vortices, for example) to have a low convection velocity. Since these are moving away from the wall, they will correspond to fast rings moving away from the wall. These exhibit long streak formation which is stable, and pinch-off, depending upon the thickness of the wall layer. We do see long stable low speed streaks in the boundary layer (Falco 1980), and we have limited evidence of hairpin pinch-off (Falco 1983). On the other hand, typical eddies that are convecting

towards the wall will be of relatively high speed, and thus simulated by low speed vortex rings moving towards the wall. These will produce long streaks which go unstable (undergoing either wavy or lumpy instabilities), short streaks which go unstable, and pockets in all cases. Again we see all these events in the turbulent boundary layer. Fig. 4.25 shows a comparison with what were observed by Offen, Kline (1975) and Smith (1978). The similarity is apparent.

The wide range of interactions that can be simulated using the vortex ring/moving wall experiments are not all admitted by the turbulent boundary layer with equal frequency. Some are not admitted at all. The range of the parameters (angle, wall layer thickness, convection velocity) found in the boundary layer are limited, and in all cases they have skewed probability distributions (towards higher values) that are approximately lognormal. When these distributions are used to determine the events that are most probable, we begin to see what to expect.

4.5.2 Spacing between streaks

Fig. 4.26 shows the distribution of D^+ obtained from the diameter of the typical eddies of a turbulent boundary layer at $Re_\theta \approx 1176$ (Falco 1974), superimposed upon the streak spacing obtained for various size rings. When the simulation outcomes are conditioned by the probabilities of scales found in this boundary layer, we see that the simulation gives a most likely streak spacing of approximately 100 wall units. This is an important quantitative test of the quality of the simulation, for although the average streak spacing is $Z^+ = 100$, all observations of streak pairs have also shown their spacing to be approximately this value.

4.5.3 The vortical motions associated with the streaky structure

The three-view visualization realized the vortical motions associated with the

streaky structure in the vortex ring/moving wall interaction (see Sec. 4.3.4). We may interpret as follows. When the coherent motion moves towards the wall from the outer region, the pressure gradient at the wall in the spanwise direction will cause the creation of the streamwise vorticity and roll up into vortices later on. The size of the counter-rotating streamwise vortices observed to be associated with each streak resulted from the vortex ring/moving wall interaction (see Fig. 4.21) is very much different from the familiar sketch of the counter rotating vortices (see Fig. 4. 27) in turbulent boundary layers which was hypothesized by many investigators.

Some investigators hypothesized that the lifted hairpin vortices found in the wall region of the turbulent boundary layers were responsible for the formation of the low speed streaks. However, this phenomenon was not observed in the vortex ring/moving wall interaction simulation. The main hairpin is observed to form due to the interaction between the lower lobe of the vortex ring and the wall layer fluid; its strength depends on how close the ring can approach (this is just what was defined as four Types of interaction). This lifted hairpin will not last long enough to form such a long streak which is about $1000 x^+$. Because soon after it is lifted, it may either get ingested into the lower lobe of the ring and lose its coherence or stay in the low shear region. However, in the second case the two legs of the hairpin are too far apart (see Sec. 4.3.4.1) as well as too far away from the wall (the tip of the hairpin will reach as far as $40 y^+$), it is not possible to form a streak between the legs; and the laser illuminated end view indicates that even if this lifted hairpin does not get ingested into the vortex ring it will not keep its coherence over $30 t^+$. Some interactions (Fig. 4.8 and 4.21 for examples) do result in the formation of the secondary hairpin vortices over streaks, this phenomena is a consequence of the viscous effect between the two vortices of each streamwise vortex pair and is not the initiator of the formation of the streaks. This is also shown clearly in the conceptual picture in Fig. 4.22.

As mentioned in Sec. 4.3.4.2, the fast vortex ring moves away from the wall which corresponds to the vortex ring moving away from the wall with low convection velocity in the turbulent boundary layer. The observed long streaks are just the legs of the lifted hairpin vortex; they are one unit. The dye marker actually concentrated with the streamwise vortices. Thus, this type of interaction should not be confused with the typically assumed non-vortical structure of streaks.

We have very limited information about distributions of this type for the angles of incidence and/or movement away from the wall, for the convection velocity, and for the instantaneous wall layer thickness, but the evidence indicates that the frequency of occurrence of many of the interactions which we can simulate is quite low in the turbulent boundary layer. Often these interactions are very intense. Thus, the conditions in the boundary layer that exist which keep their probability low are likely to be essential to the maintenance of the measured values of the drag. We need to explore ways to further limit the occurrence of the violent breakups if we are to pursue a rational program of drag reduction (and noise reduction) in the boundary layer. The model allows us to isolate a specific high drag producing event, and carefully study the parameters that it depends upon. We are currently building the sample sizes necessary to more accurately obtain the distributions mentioned above.

4.5.4 Implications for drag modifications

As we have seen, small changes in the parameters of typical eddy size, incidence angle, convection velocity, and wall layer thickness can alter the evolutions that result when a typical eddy interacts with the wall. Changes in any of these variables which cause a cross over in the boundaries (such as those shown in Fig. 4.18), will result in a change in the drag at the wall.

Consider, for example, the angle of incidence. If we can change the strength of

the large scale motions, say, by outer layer manipulators, we can easily change the angle of a typical eddy that is moving towards the wall, and may even be able to change the direction if it is at a shallow angle, so as to make it move away from the wall. This will affect the stability of both the local eddy wall interaction (interactions of Type I-IV), and the stability of the streaky structure which is created, as well as the formation of new typical eddies via the pinch-off process. Thus, we can affect not only the local drag, but alter the drag downstream by directly interfering with the cyclic production process.

Modifications to the wall that result in small changes in the effective wall region thickness, for example, NASA riblets, will also have an effect on the drag. If increases in wall region thickness above the critical thicknesses can be made (see for example, Fig. 4.18), streaks are more likely to remain stable. Furthermore, the local interactions (Types I-IV) will also tend to be of Type I and II. Thus, the drag can also be reduced.

4.6 Summary and Comment

New boundary layer observations in the Turbulence Structure Laboratory, Michigan State University have suggested that long low speed streaks are formed in pairs as the result of the interactions of microscale very coherent vortex ring-like eddies (typical eddies) propagating over the wall. Depending upon the distance from the wall, the angle of incidence of the eddy with the wall (both magnitude and sign), the convection velocity of the eddy, and the local thickness of the viscous wall region, different structural features can evolve out of the evolution. The extent of the distance over which a typical eddy could interact with the wall and wall layer flow was a surprise, but means that many coherent microscale eddies that are in the logarithmic region and further out take part in the production process.

The vortex ring/moving wall simulation incorporates all of the evolutions and

structural features associated with the turbulence production process. Besides, the results of the three-view visualization present the similar vortical structure associated with the low speed streaks found in the near wall region of turbulent boundary layers. The vortex ring/moving wall simulation dramatically demonstrates that the pre-existing streamwise vortices are not required to produce streamwise streaks. When the streak spacings obtained in the simulation are conditioned by the probability of occurrence of typical eddy scales found in the boundary layer, we see that the simulation provides the correct streak spacing (approximately 100 wall units). Other possible outcomes of the simulation need to be weighed by the measured probabilities of occurrence of the angles, convection velocities, and length scales of the typical eddies in the turbulent boundary layer to enable us to obtain a picture of the most probable forms of the interactions, and to gain insight into the causes of the interactions which occur with lower probability, that may contribute significantly to the transport. It appears that turbulent boundary layer control leading to drag reduction can be realized by fostering the conditions suggested by the simulations which will increase the probability of having stable interactions.

All the results discussed in this chapter are from the flow visualization of the vortex ring/moving wall interaction simulations. Flow visualization, however, can only give partial information at best. The three major reasons for this are:

- a) flow visualization is strictly valid only in highly energetic motions,
- b) flow visualization has characteristics to leave vortical remnants which may lead to incorrect conclusions about the flow kinematics, and
- c) the conventional flow visualization techniques are valid for only short time, since once the dye marker has been removed from a given region no information about

the kinematics in that region may be obtained.

Thus, in order to verify the conclusion drawn from the flow visualization and to answer some questions which were not answered through the flow visualization such as the initial conditions in the vortex ring/moving wall interactions: vorticity distribution over the Stokes' layer and vorticity distribution associated with the vortex ring, the velocity distribution associated with the streaky structure, and the streamwise vorticity distribution associated with the streaky structure, it was necessary to make quantitative measurements. The Laser Induced Photochemical Anemometry (LIPA) technique was accessed in this quantification. The results of which are given in the following chapter.

CHAPTER 5

QUANTITATIVE REFINEMENT OF THE VORTEX RING/MOVING WALL INTERACTION MODEL

5.1 INTRODUCTION

As mentioned in chapter 4, the vortex ring/moving wall interaction model provided a conceptual picture (shown in Fig. 4.22) describing the spatial information of all visual features observed in the wall region of wall bounded turbulent flows. The flow shown in Fig. 4.22 is completely unsteady and three-dimensional. The best existing probe techniques are not enough in helping us to answer the questions listed in the conclusion of chapter 4. To the author's knowledge, the photochromic techniques are the unique techniques that enable us to measure nonintrusively the instantaneous fluid dynamic quantities such as velocities, vorticity, circulation, and strain rates over a two-dimensional domain in such a flow field.

We applied both single tracer technique and grid tracing technique to quantify the vortex ring/moving wall interaction model. First, we measured the Stokes' layer flow and also checked the accuracy of the grid tracing technique. Then, we applied those techniques to more complicated measurements associated with the Type II interaction of the vortex ring/moving wall simulation including:

- a) vortex ring flow,
- b) velocity distributions in the wall region, and
- c) streamwise vorticity distribution in the wall region.

5.2 STOKES' LAYER MEASUREMENT

5.2.1 Introduction

In this section we first discuss the measurement of a Stokes' layer which was approximated by a rapidly started moving belt and was used to simulate the viscous wall layer in the vortex ring/moving wall interaction mentioned in chapter 4. Although the Stokes' layer flow is the simplest unsteady flow, the measurement is somewhat difficult; so far no measurement has yet been made. Since the Stokes' layer flow is one-dimensional in space (only has diffusion in y-direction), an exact solution of the Navier-Stokes equations is available. By applying the photochromic grid tracing technique we were able to obtain the instantaneous velocity distribution, velocity gradients, and vorticity distribution across the layer and were also able to test the accuracy of this technique against the exact solutions.

5.2.2 Experimental details

Fig. 5.1 presents the schematic representation of the setup of Stokes' layer measurement; the moving belt system is similar to what was used in the water tank. The width of the belt is 17.8 cm, and the distance between the rollers is 152.4 cm with the test position 90 cm downstream of the leading roller. All experimental data were obtained before the leading edge effects reached the test position. Furthermore, the aspect ratio is sufficient to prevent the disturbances generated in the corners from reaching the center of the belt when the data were taken. Therefore, the wall layer flow measured was one-dimensional. The working fluid was deodorized kerosene in which 10 ppm of the photochromic chemical was dissolved. Fig. 5.2 shows the optical set-up for generating the photochromic grid. Because only spanwise vorticity components were to be measured, the depth of field looking into flow was not crucial. The best orientation for the incident beam is also shown in Fig. 5.2.

Fig. 5.3 shows the flow chart of the control system of the Stokes' layer

measurement. Time delay # 1 initiates the excimer laser to generate a photochromic grid as well as calculating time (t) involved in the exact solution of Stokes' layer, while time delay # 2 initiates the data acquisition system which includes a 35 mm high speed Photo-Sonic movie camera and background lighting. Usually we start the movie camera 2.5 seconds prior to the data acquisition because the surge time of the camera to its full speed is 1.5 second. The data were recorded on Kodak Tmax ASA 400 film through a micro lens at 200 frames per second. The films were analyzed on a NAC motion film analyzer which is accurate to 0.05 mm.

5.2.3 Results

Fig. 5.4 shows two photos from the result of the Stokes' layer measurement which are 0.05 seconds apart; these photos were taken under conditions with $U_w = 12.7$ cm/sec and belt running time $t = 5.25$ seconds; the belt moved from right to left. Fig. 5.5 shows the non-dimensional velocity profile for two belt running speeds; the solid line represents the exact solution. Results of the velocity gradient $\partial u / \partial y$ obtained from double differentiation and of the spanwise vorticity obtained from circulation approach are shown in Fig. 5.6, where they are compared with the exact solution. Everything is non-dimensional by the similarity variables of the exact solution. In theory, the spanwise vorticity ω_z is equal to $-(\partial u / \partial y)$ in Stokes' layer since $\partial v / \partial x$ is equal to zero. Because the flow is one-dimensional, incompressible, and does not change with the streamwise coordinate, x , the continuity equation reduces to $\partial v / \partial y = 0$. A check of this across the Stokes' layer is also shown in Fig. 5.6. The mean value of $(\partial v / \partial y)^*$ across the layer is -0.011 and the standard deviation is 0.095, which corresponds to 1/second.

5.2.4 Discussion and Summary

By applying the photochromic grid tracing technique, we obtained the

instantaneous velocity distribution and, for the first time, the vorticity distribution across the Stokes' layer. There is an agreement among the velocity profiles in Fig. 5.5 except in the vicinity of the edge of the Stokes' layer. This may be caused by the free surface effect, the small disturbance from the driving system, and the reading error. The errors involved in the calculation of velocity gradient, the vorticity distribution and the check of continuity equation are of similar magnitude. The absolute value of the error is $\pm 2/\text{sec}$ which is consistent with the design error analysis. The deviation of the experimental profile in the near wall region is a consequence of the grid mesh being too large (the largest mesh in vertical direction in Fig. 5.4 is about 0.15δ) to adequately resolve the large value of the gradient $\partial u / \partial y$. On the whole, the results are very encouraging, which indicates that by using the exact solutions of Stokes' layer we can estimate the velocity, velocity gradient and spanwise vorticity distribution associated with the undisturbed viscous wall layer for different belt speeds in the vortex ring/moving wall interactions as long as the leading edge effect of the belt does not reach the test position.

The demonstrated accuracy of the photochromic grid tracing technique in Stokes' layer measurement is more than adequate for many fluid dynamic problems. As speed increases 100-fold the accuracy can, in principle, be maintained, since the calibration depends only on a time and a length scale. There is further room for improvement through the use of high resolution image processing. At present, this technique is accurate enough to apply to more complicated flow measurements which will be mentioned in the following sections in the chapter.

5.3. VORTEX RING MEASUREMENT

5.3.1 Introduction

The second item to be quantified in the vortex ring/wall interaction is the vortex ring, the source of the excitation. The vortex ring represents a class of flow fields that are of particular importance in turbulent and unsteady flow. Several techniques had been attempted to measure the detailed structure of the vortex ring. The hydrogen bubble technique was attempted by Maxworthy (1972), but the results were inaccurate due to strong axial gradients and associated radial velocities. Hot wire measurements are hampered by probe interference and difficulty of calibration. Recently, numerous investigators such as Sullivan and Widnall (1973), Maxworthy (1977) and Didden (1979) used a two-component laser doppler velocimeter (LDV); although this technique has taken care of the intrusive problem, it is still a single point measurement, and can only be used to get the circulation distribution, not the local vorticity. By using the photochromic grid tracing technique we can obtain instantaneous velocity distribution and vorticity distribution, allowing us to gain deeper understanding of the dynamics of vortex ring flow.

5.3.2 Experimental details

The experimental set-up used to generate and measure the vortex ring is shown in fig. 5.7. The same ring generating system applied in the water tank was used. The flow chart of the control system for vortex ring measurement is shown in Fig. 5.8. In order to match the Reynolds number of the vortex ring which was used in the vortex ring/moving wall interaction in the water tank, a 19mm inner diameter orifice was used. The kerosene in the reservoir was dyed with chlorophyll to mark the vortex ring (Fig. 5.9 shows the lower half of ring marked with the dye). This enabled us to easily locate the frames that needed to be analyzed. The flow was axisymmetric, so that we needed only to align our grid through an axis of symmetry and to measure the flow in half of the ring. The measuring window was at four ring bubble diameters downstream

of the exit of the orifice.

5.3.3 Results

Fig. 5.9 shows two photos of the result which are 0.07 seconds apart. The instantaneous velocities distributed along two axes of the ring are shown in Fig. 5.10. The instantaneous circulation distribution of the ring is shown in Fig. 5.11, which also shows the results obtained by Sullivan et al. (1973) for different Reynolds numbers along with the Hill's exact solution of a spherical vortex, although there is no solution existing for the experimentally generated rings. Through the circulation approach we obtained the instantaneous vorticity distribution over a ring, which is shown in Fig. 5.12.

5.3.4 Discussion and summary

The vorticity distribution obtained from the photochromic technique is the instantaneous vorticity distribution associated with a vortex ring and no use of Taylor's hypothesis is required. To know the time evolution of a vortex ring we must simply generate the photochromic grid at different locations downstream of the orifice or use the moving grid generating system to follow a vortex ring.

Comparing the vorticity and circulation distributions with those obtained by Sullivan et al. (shown in Fig. 5.11 and Fig. 5.12) shows clearly the Reynolds number dependency, even though the ring generating systems are different. Interestingly, the comparison also shows that the circulation distribution associated with the low Reynolds number vortex ring is closer to that of the Hill's spherical vortex.

5.4 FLOW VISUALIZATION IN KEROSENE TANK

5.4.1 Introduction

By using the photochromic grid tracing technique we are able to quantify the Stokes' layer flow and the vortex ring flow separately. These are the two initially independent flow fields. To gain insights into their interaction, in other words, to obtain the optimal spatial and temporal information about interactions such as the strength of the streamwise vorticity associated with the streaky structure and how the streamwise vorticity changes with the time, we must have an overview of the interaction to determine where and when to make the measurements. Thus, flow visualization is needed to make sure that: 1) the same experiments can be repeated in the kerosene tank (required to use photochromic chemical) at the same Reynolds number, and 2) the measurement window is optimal, that is, we will measure most of the events of interest at the chosen position and time.

5.4.2 Experimental details

The experimental apparatus for flow visualization in the kerosene tank had the same arrangement and control system as that used in the water tank (see Fig. 4.3), but the scales and materials were different. The width of the moving belt was 17.8 cm; the inner diameter of the orifice was 1.9 cm and its center was located 3.8 cm above the wall. The incident angle of the vortex ring was set at 3 degrees with respect to the moving belt. The plate which supported the moving belt was Teflon, a kerosene resistant material. The kerosene in the reservoir was dyed with chlorophyll to mark the vortex ring. As far as the dye marker in the wall layer is concerned, we gently injected the chlorophyll dyed kerosene by a syringe to cover some part of the belt before each run and waited long enough to let the injected dye settle.

The primary visual data consisted of plan and side view time resolved images which were collected by using a 35 mm Photo-Sonic movie camera with a micro-lens on Kodak Tri-X 400 ASA film. The side view was illuminated by a 300 watt flood light

diffused through a white color filter. The top view was illuminated by two 300 watt flood lights from underneath and the white teflon plate worked as a white color filter. The frame rate of the movie camera was 20 frames/sec.

5.4.3 Results

Fig. 5.13 shows one set of photos with both top view and side view describing the time evolution of vortex ring/moving wall interactions in the conditions of $U_r/U_w = 0.26$, 3 degrees of incident angle, $\delta/D \approx 0.18$ and $U_w = 15.5$ cm/sec. The non-dimensional ring diameter was 120 wall layer units. These pictures show clearly the same features which were visualized in the Type II interaction in the water tank under the same flow condition. A pair of streaks with spacing 140 wall layer units were observed, which is consistent with that shown in Fig. 4.21. Besides, the hairpin liftup and pocket also were observed. This consistency gave us confidence that no appreciable changes during startup resulted because of the factor of two increase in viscosity. Through the evolution of the interaction we were able to locate the position where the photochromic tracer or grid will be sent.

By sending a single photochromic tracer parallel to the moving wall at $y^+ \approx 16$ we obtained the visual result of the interaction shown in Fig. 5.14 which is the same as that obtained from the hydrogen bubble technique used by many other researchers, such as Kim et al.(1971) or Smith et al.(1983).

5.4.4 Discussion and summary

The result of the flow visualization of the vortex ring/moving wall simulation in kerosene tank showed the same features which were observed in the Type II interaction in the water tank. Those visual results also provided the information to locate the optimal position for the velocity measurement. Furthermore, the vortex ring/moving

wall interaction model could produce the same visual features which were visualized through the hydrogen bubble technique in the near wall region of wall bounded turbulent flows.

5.5 VELOCITY DISTRIBUTION ASSOCIATED WITH THE VORTEX RING/ MOVING WALL INTERACTION

5.5.1 Introduction

Even though the flow visualization in the vortex ring/moving wall interaction model did show clearly the formation of a pair of streaks, it did not provide information on the characteristics of the streaks except for the spacing between the streaks. If the model is good, the velocity measurement (temporal and spatial information) will show quantitatively the same as that measured and observed in turbulent boundary layers. These measurements will be able to provide insights into how the viscous wall layer responds to the disturbance from the vortex ring during the interaction. Based upon the results obtained from the flow visualization in the kerosene tank, we figured out that if measurements are conducted only in one fixed location, then the location is 25.4 cm (i.e. $x/D = 8$) downstream of the exit of the orifice, where we will be able to monitor the major events of the interaction. In these measurements the photochromic tracer technique was used; it is the only technique available to obtain the velocity distribution precisely and efficiently for this particular flow field. We can generate photochromic tracers either perpendicular (in x-y plane) or parallel to the wall (in x-z plane) and obtain the associated velocity distribution in the mean flow direction.

5.5.2 Experimental details

We repeated the same experiment as we did for flow visualization in the

kerosene tank in Sec. 5.4. Fig. 5.15 shows the locations of measurement. Because we could only record one photochromic tracer for each run in the spanwise direction (z-direction), we needed to repeat the same experiment several times to obtain the whole information in the z-direction. The high repeatability of vortex ring/moving wall interaction did provide the reliability to put the measurements together from different runs (the variance of the velocities of the vortex ring and the moving belt are less than 5% for different runs). We only measured half of the flow field as shown in Fig. 5.15, because the flow field was symmetric about the center line (see Fig. 5.15 also). A special optical apparatus was designed for this purpose; a movable carriage which was controlled precisely by a threaded rod carried a set of optical components including one 500 mm focal lens and two reflecting mirrors to accurately guide the laser light beam to the measuring positions. Fig. 5.16 shows the details of the optical configuration. The Excimer laser was set to pulse 10 times per second and the 35 mm Photo-Sonic movie camera was also set at 10 frames per second. We synchronized the belt running system and data acquisition system. As the switch was turned on, the belt, camera, background lighting (a 300 watt flood light) and movie camera started simultaneously. The instantaneous time lines which represented the instantaneous velocity distribution in the streamwise direction were recorded on T-MAX 400 ASA film through a micro-lens. The films were processed with Microdol-X at 70 degrees F for 10 minutes and were digitized by a NAC film analyzer. For each frame we could measure the non-dimensional velocity components, $U(y)/U_w$, at different y positions.

5.5.3 Results

We analyzed the data for each measurement point and obtained the spatial and temporal velocity information of the wall layer as follows:

- a) Fig. 5.17 (a) through (d) show the time evolution of the non-dimensional

streamwise velocity distribution at the measurement points. The dotted lines represent the undisturbed velocity profiles of the Stokes' layer. The visual information corresponding to Fig. 5.17 is shown in Fig. 5.13; the arrows indicate the measured location.

b) Fig. 5.18 (a) through (d) show the time evolution of the constant streamwise velocity lines in y-z plane. Again, the dotted lines represent the constant velocity levels of the undisturbed Stokes' layer.

5.5.4 Discussion and summary

Fig. 5.17 shows that the wall layer fluids are accelerated, decelerated, and then lifted up. The results shown in Fig. 5.18 indicate that there is a distinct region of high momentum fluids being pumped away from the wall. As the results shown in Fig. 5.18 are compared with those obtained from flow visualization shown in Fig. 5.13, we found that the long streaks observed by the flow visualization in the vortex ring/moving wall interaction simulation (discussed in Sec. 4.3.1.2, 4.4.1 and 5.4) were the high speed region. This phenomenon also confirms what was observed in the three-view flow visualization in Sec. 4.4.1 (see the laser illuminated end view in Fig. 4.21), where a pair of counter-rotating streamwise vortices associated with each streak was observed. The pair of counter-rotating streamwise vortices pumped the high momentum fluids away from the wall. Again, the width of each streak is also about $30 z^+$ (see the hump in Fig. 5.18 (c)).

As the results shown in Fig. 5.17 and 5.18 were observed from the point of view of the turbulent boundary layer by performing the Galilean transformation (see Fig. 5.19), we see clearly that the vortex ring/moving wall interaction model can simulate the characteristics of the low speed streaks observed in wall bounded turbulent flows.

The data shown in Fig. 5.19 represent the velocity defect or gain with respect to the undisturbed wall layer (i.e the layer after performing the Galilean transformation shown in the lower half of Fig. 5.19 (a)) at different y^+ . The characteristics of the low speed streaks found in Fig. 5.18 and 5.19 are listed as follows:

- a) the spacing (distance between the peak of humps)
is about the size of the vortex ring (see Fig. 5.18(c),
5.19(c) and Fig. 4.26); note that the ring bubble
diameter in this measurement was 3.18cm (1 1/4 in);
- b) the region and the percentage of the velocity
defect is clearly shown; for example, a 30 % of
velocity defect is found at $y^+ = 15$ (Fig. 5.19(c));
- c) the width of each streak (if it is defined as the
region in which the velocity defect is over 10 %)
is about $30 z^+$ at $y^+ = 10$ (Fig. 5.19 (c) and is
about $20 z^+$ at $y^+ = 10$; and
- d) the extent of coherent liftup may reach about $y^+ =$
40 (see Fig. 5.18 and 5.19).

These results compare well with those obtained from turbulent boundary layer flows. (see Smith & Metzler 1983)

Besides, the results shown in Fig. 5.18 precisely define the spanwise location of the test window for measurement of the streamwise vorticity associated with the streaky structure.

5.6. STREAMWISE VORTICITY MEASUREMENT ASSOCIATED WITH THE VORTEX RING MOVING WALL INTERACTION

5.6.1 Introduction

From the result of the three-view visualization of the vortex ring/moving wall interaction in water tank, we observed the vortical structure associated with the streaks, which showed that a pair of counter-rotating streamwise vortices accompanied each single streak in the later stage of the streak formation. This phenomenon is similar to what was found by Blackwelder and Eckelmann (1979). The morphological comparison was mentioned in Sec. 4.5.3. Blackwelder and Eckelmann (1979) studied the vortex structures associated with the bursting process as defined by VITA and estimated the streamwise vorticity by using hot-film sensors and flush mounted wall elements. They found that the streamwise vorticity was one order of magnitude less than that of spanwise vorticity and the middle of the vortex structures lay approximately at $y^+ = 20-30$. In this section, we quantify the streamwise vorticity associated with the streaky structure in Type II interaction of the vortex ring/moving wall simulation such that we may have further comparison with the information obtained from the turbulent boundary layers. By using the photochromic grid tracing technique we are able to obtain the spatial and temporal information on streamwise vorticity distribution as well as on the Reynolds stress distribution.

5.6.2 Experimental details

The same experiment which was conducted in Sec. 5.4 and in Sec. 5.5 was repeated in this section. The initial conditions of this vortex ring/moving wall interaction result in a Type II interaction: the incident vortex survives and the pair of streaks break up.

The test area, located at the same position which is 25.4 cm downstream of the exit of the orifice. Because the test area of the photochromic grid tracing technique is limited, we adjusted it to cover a single streak and its adjacent area. It covered from 25 to 80 z^+ from the center line of the flow and up to 40 y^+ from the moving wall. Fig. 5.20 shows the optical configuration and the orientation of the laser beam. In this experiment we took advantage of the test area being close to the side window of the kerosene tank, so that we could adjust the laser beams in the grid to be almost orthogonal. This kind of optical arrangement will provide better resolution in the direction which is perpendicular to the wall than that of the diamond shape grid box used in vortex ring and Stokes' layer measurements.

The side view of the data acquisition and lighting system is shown in Fig. 5.21 including the Photosonic 35 mm movie camera, one 300 watt projector light bulb, and white color filter. A F1.2 Nikon lens and a 2.0 x QUANTARAY 7 ELEMENT Auto Tele Converter were used to magnify the image; the background lighting was set at 60% of the output through a potentiometer and was concentrated by a convex lens. The repetition rate of the excimer laser was 2.5 Hz, that is, a fresh photochromic grid was generated every 0.4 seconds. The images were recorded at 50 frames/second on Kodak 400 Tmax films and were processed in Microdol-X for 10 minutes at 70 F. The film was digitized through the NAC film analyzer.

5.6.3 Results

Fig. 5.22 (a) and (b) show the results of the streamwise vorticity measurement, the first photo of each set shown in Fig. 5.22 was photographed at 6.8 and 7.6 seconds respectively after belt started, which corresponded to $t^* = 55.3$ and 61.8 respectively. Those photos are selected from the same sequence of movie in one experiment. Two photos of each set were 0.02 second apart which corresponded to 0.5 t^+ apart.

Following the procedures mentioned in Chapter 2, the data were deduced from each set of the photos and the corresponding contour plots of the instantaneous streamwise vorticity distribution were obtained, which are shown in Fig. 5.23.

Fig. 5.24 (a) through (f) represent the instantaneous Reynolds stress distributions which were also obtained from the same data base as that of Fig. 5.23 (a) through (f).

5.6.4 Discussion and summary

In the early stage (see Fig. 5.23 (a) and (b)) of the formation of streamwise vortices, the maximum value ($O(1/\text{sec.})$) is about the noise level of this technique. Even at this moment the visualization already shows the nicely-formed streaks at the test area (Fig. 5.23 (a)-(d) almost correspond to the vortical structure shown in the end views of Fig. 4.21 (a)-(d)). It means that even though the level of the streamwise vorticity is very low, it is able to gather the dye marker together to form streaks. However, the velocity information (see Fig. 5.17 (d)) shows that the velocity profile in the mean flow direction appears to have a very strong defect in spanwise direction, that is, it has a very big $\partial u / \partial z$.

As we follow the time evolution of the streamwise vorticity distribution shown in Fig. 5.23 (a) and (b), a pair of counter-rotating streamwise vortices induced themselves up to about $y^+ = 20$, their strength, ω_x^* was about 0.19. which is about one order of magnitude less than the spanwise vorticity (the mean spanwise vorticity, ω_z^* , in the wall layer was about 1.04). A photo taken 0.02 second before $t^* = 58.6$ (shown in Fig. 5.25 (a)) indicates that a pair of counter-rotating streamwise vortices formed from the wall and moved upward. The old photochromic dye marker showed a blurry region in the vicinity of the wall. It means that the fluid in this blurry region has relatively higher

speed because it comes from the near wall region and has high momentum. If we look at this from the point of view of the turbulent boundary layer, this is just the low momentum fluid ejected from the near wall region; this argument is also supported by the velocity measurement shown in Fig. 5.17 (c) and (d) (sliced view of velocity distribution in x-z plane shows the corresponding low momentum region). As soon as the edge of the pocket reached the measuring window (it started shortly before $t^* = 55.3$, evidence of this came from the result of visualization both in the water tank and in the kerosene tank; see Fig. 4.21 (b)), this pair of streamwise vortices was dominated by the pocket vortex which may come from the bending of existing spanwise vorticity (see the difference between Fig. 5.23 (c) and (d)). The results show that the contribution from $\partial w/\partial y$ and $\partial v/\partial z$ are almost equal; it may suggest this bending of an existing vortex line from the spanwise direction to the streamwise direction. The fast outward spreading of the edge of the pocket suggested that there was a strong pressure perturbation from the incident vortex ring and a strong $\partial w/\partial y$ contributed to ω_x .

The maximum ω_z associated with the vortex ring used in this interaction was 35/sec and the maximum measured ω_x was about 15/sec which corresponded to about 1/2 of the ω_z existing in the wall layer. The ratio $(\omega_x/\omega_z)_{\max}$ is about 0.43.

The total circulation of the strong vortex (the region with positive sign shown in Fig. 5.23) increased dramatically from $t^* = 58.6$ to $t^* = 65.1$, which is shown in Fig. 5.26. The turning of the direction of the pocket vortex (see Falco 1980b) to the streamwise direction (i.e. the streamwise vorticity component will increase) is a possible reason for the increase of the circulation (see Fig. 5.27). And the area of this strong vortex may be caused by the shape of the pocket vortex as well as the viscous diffusion. It separated about $20 t^+$ between $t^* = 58.6$ and $t^* = 65.1$; the viscous diffusion can do something within $20 t^+$. This also can explain the decreasing of the peak value of the

streamwise vorticity ω_x^* from 1.47 to 0.83 within $20 t^+$ (see Fig. 5.23 (d) and (f)).

The vorticity contours also show the strength of the hairpin which was originally the pair of streamwise vortices associated with each single streak. One leg of this hairpin merged with the pocket vortex and the hairpin vortex was as a whole unit induced by the pocket vortex (Fig. 5.28 shows the possible merging process). Fig. 5.23 (c)-(e) shows the time evolution of this emerging. Fig. 5.26 also shows the total circulation of one leg of this hairpin vortex (the region with negative sign shown in Fig. 5.23). The maximum strength of the streamwise vorticity, ω_x^* , associated with this lifted hairpin was about 0.62. and the associated instantaneous Reynolds stress $vw/u_\tau u_\tau$ was low compared with that associated with pocket vortex (see Fig. 5.24 (d), Reynolds stress distribution). This means that the Reynolds stress associated with the streaky structure was low and was about 30% of that of the pocket vortex. Thus, we have a detailed breakdown of the contributions of the long streaks and the pockets to streamwise vorticity and the Reynolds stress produced by it.

5.7 Summary

5.7.1 The photochromic technique - an accurate and powerful technique

Data derived by the photochromic technique has been used throughout this chapter. Using a photochromic mesh of small enough size, instantaneous fluid dynamic quantities over a two-dimensional field can be measured. The predicted accuracy through the classical error analysis described in Chapter 2 has been confirmed in the Stokes' layer measurement. Using this technique we have quantified the velocity and vorticity distributions of the two originally independent fluid flows (i.e. the Stokes' layer and the vortex ring) of the vortex ring/moving wall interactions. We have also

measured both temporal and spatial information pertaining to the velocity distributions and streamwise vorticity distributions associated with the vortex ring/moving wall interaction.

5.7.2 Further understanding of turbulence production process through the vortex ring/moving wall interaction model

The visual and photochromic technique derived results of the vortex ring/moving wall interaction simulation indicate that this model not only demonstrates qualitative agreement with the near wall boundary layer phenomena but also quantitatively captures the correct kinematical magnitudes associated with this phenomena. This was demonstrated in the velocity measurements associated with the vortex ring/moving wall interaction in that the characteristics of the low speed streaks were fully revealed. Furthermore, the model studies show that the streamwise vorticity associated with the streaky structure is about one order of magnitude less than the mean spanwise vorticity. We realized that the pocket vortex plays a very important role through the streamwise vorticity measurements. The pocket vortex is apparently responsible for the instability of the streaks, and it is the major contributor to the Reynolds stress. The secondary hairpin vortices which formed on the low speed streaks are not as important, in terms of both vorticity and Reynolds stress, as the pocket vortex.

CHAPTER 6

CONCLUSION AND FURTHER COMMENT

6.1 Conclusion

As addressed in chapter 1 this study is a combination of both the technical development of LIPA technique and its application towards understanding the basic physics of the bursting process in turbulent boundary layer flows. The major findings of this two phase experimental study can be summarized as follows:

1) A major extension of LIPA (Laser Induced Photochemical Anemometry) that enables the instantaneous velocity, velocity gradient, vorticity, and Reynolds stress to be obtained over a two-dimensional domain of a fluid flow has been developed and demonstrated. Calibration depends only upon a time and a length scale. Comparison of measurements with the exact solution in a Stokes' layer indicates that its accuracy can be predicted by classical analysis, and is comparable or better than that achievable with the best single point probe techniques. Furthermore, the LIPA is not restricted to slowly varying flows as are so many flow visualization techniques. Using the LIPA technique we have also quantified both temporal and spatial information pertaining to the velocity distributions and streamwise vorticity distributions associated with the vortex ring/moving wall interaction.

2) The LIPA technique has been applied to measure the local skin friction on both a stiff surface and a compliant surface. Eight percent skin friction reduction has been found on low damping elastic gelatin at $Re_\theta \cong 1200$. At the skin friction reduction conditions the observed onset surface deformation on the compliant surfaces was local,

three-dimensional, small scale, and short lived. This was found at approximately the same value of K , 0.6, for three different coating thicknesses. Results show that at conditions which lead to skin friction reduction, the surface response is a response to turbulence. The measured length scale, time scale, and the velocity scale associated with the observed pocket-like depressions correlate very well with those of the bursting process in wall-bounded turbulent flows.

3) The vortex ring/moving wall simulation incorporates all the evolutions and structural features associated with the turbulence production process. It dramatically demonstrates that streamwise vortices are not required to produce streamwise streaks. When the streak spacing obtained in the simulation is conditioned by the probability of occurrence of typical eddy scales found in the boundary layer, we see that the simulation provides the correct streak spacing (approximately 100 wall layer units). It also appears that turbulent boundary layer control leading to drag reduction can be realized by fostering the conditions suggested by the simulations which will increase the probability of having stable interactions.

4) The visual and LIPA technique derived results of the vortex ring/moving wall interaction simulation indicate that this model not only demonstrates qualitative agreement with the near wall boundary layer phenomena, but also quantitatively captures the correct kinematical magnitudes associated with this phenomena. This was demonstrated in the velocity measurements associated with the vortex ring/moving wall interaction, in that the characteristics of low speed streaks were fully revealed. Furthermore, the model studies show that the streamwise vorticity associated with the streaky structure is about one order of magnitude less than the mean spanwise vorticity. And finally, the model studies also realize that the secondary hairpin vortices formed on the low speed streaks are not as important, in terms of both vorticity and Reynolds

stress, as the pocket vortex.

6.2 Further comment

1) The calibration of the LIPA technique depends on only a time and a length scale; there is further room for improvement. In practice, determining the intersecting points of the grid lines is limited by the grain size of the film used, and the distortion of the developing process. Improvements in the grain limitation can be made by using a large format still camera with a shuttering mechanism that will enable a double exposure of the grid to be made on one plate. Image processing techniques have also been demonstrated to increase the accuracy and repeatability of the results.

2) Current limitations of the LIPA technique include the need to work in organic liquids, which are required to dissolve the chemicals, and available penetration of the laser beam into the liquid. The way to generalize this technique to be used in popular fluid media is ongoing at the Turbulence Structure Laboratory, Michigan State University. This ongoing research includes the study of new chemicals which can be used for water, and the scanning technique which can be used to improve the penetration problem.

3) The 'moving' LIPA technique can be used to obtain the Lagrangian information in many turbulent and unsteady flows. Its future is very promising!

FIGURES

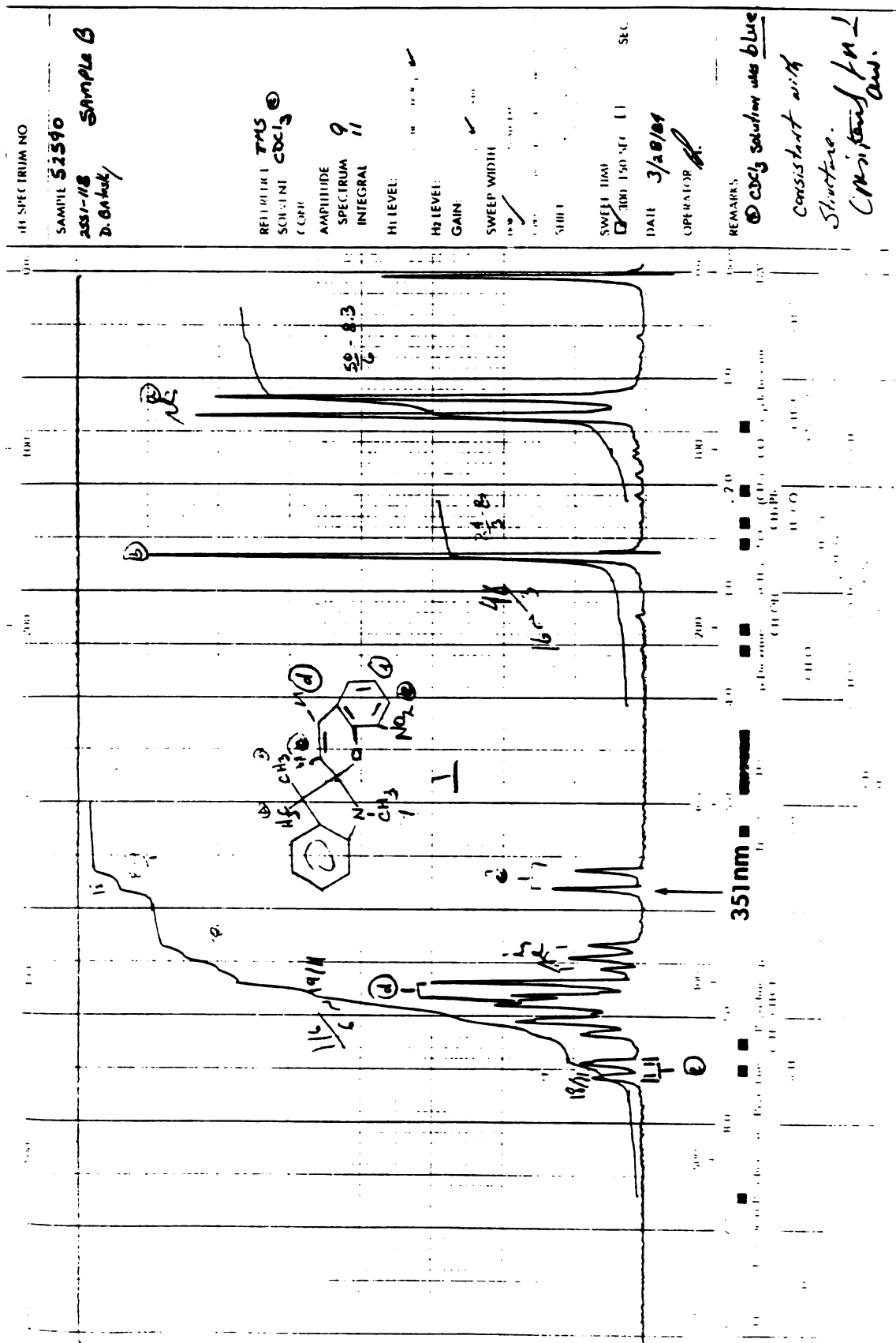


Fig. 2.1 The associated absorption and emission spectrum of the photochromic chemical used in this study.

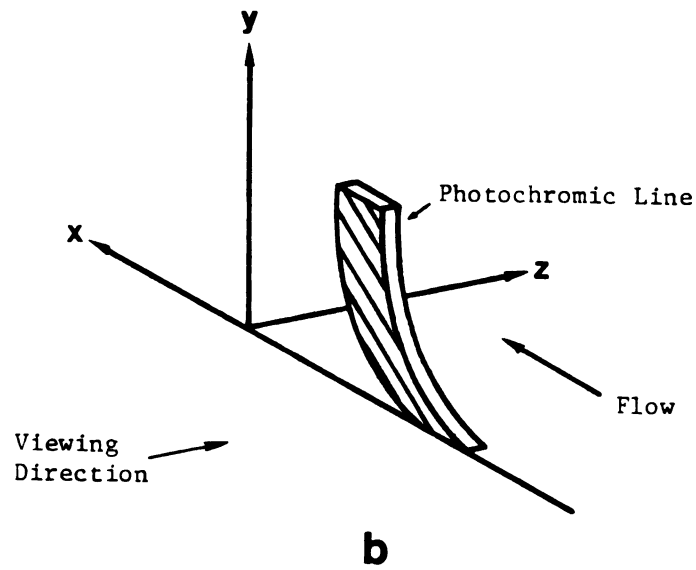
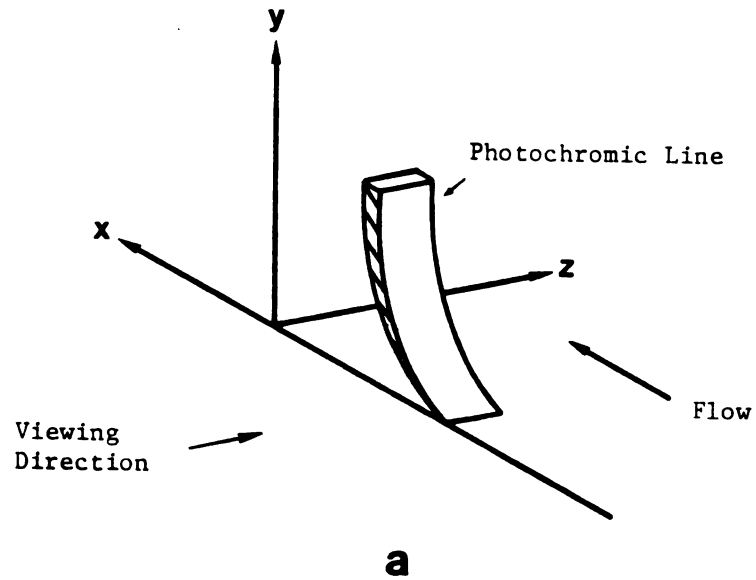
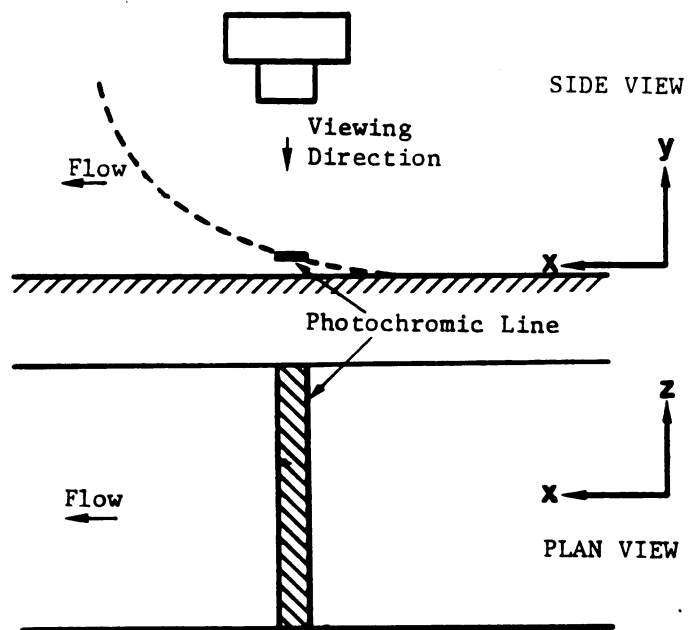


Fig. 2.2 A schematic of the stretching of the photochromic line in shear flow.



a

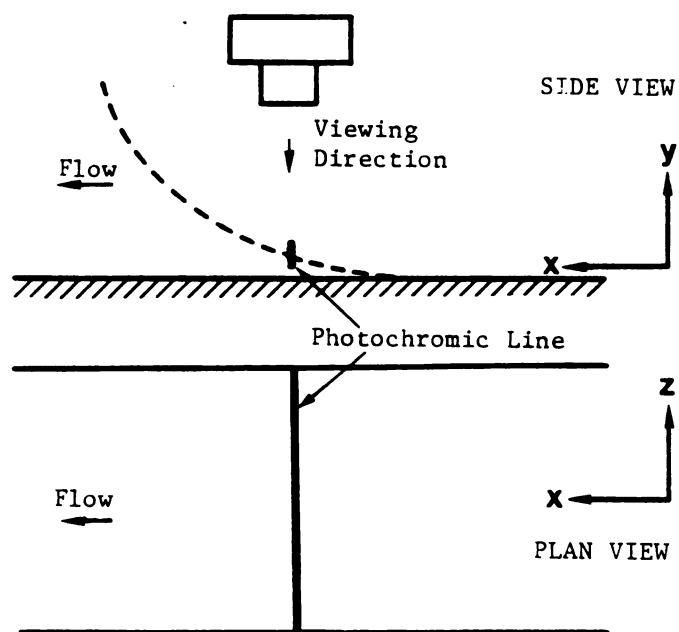


Fig. 2.3 The dependence of the quality of photochromic line on its orientation in shear flow.

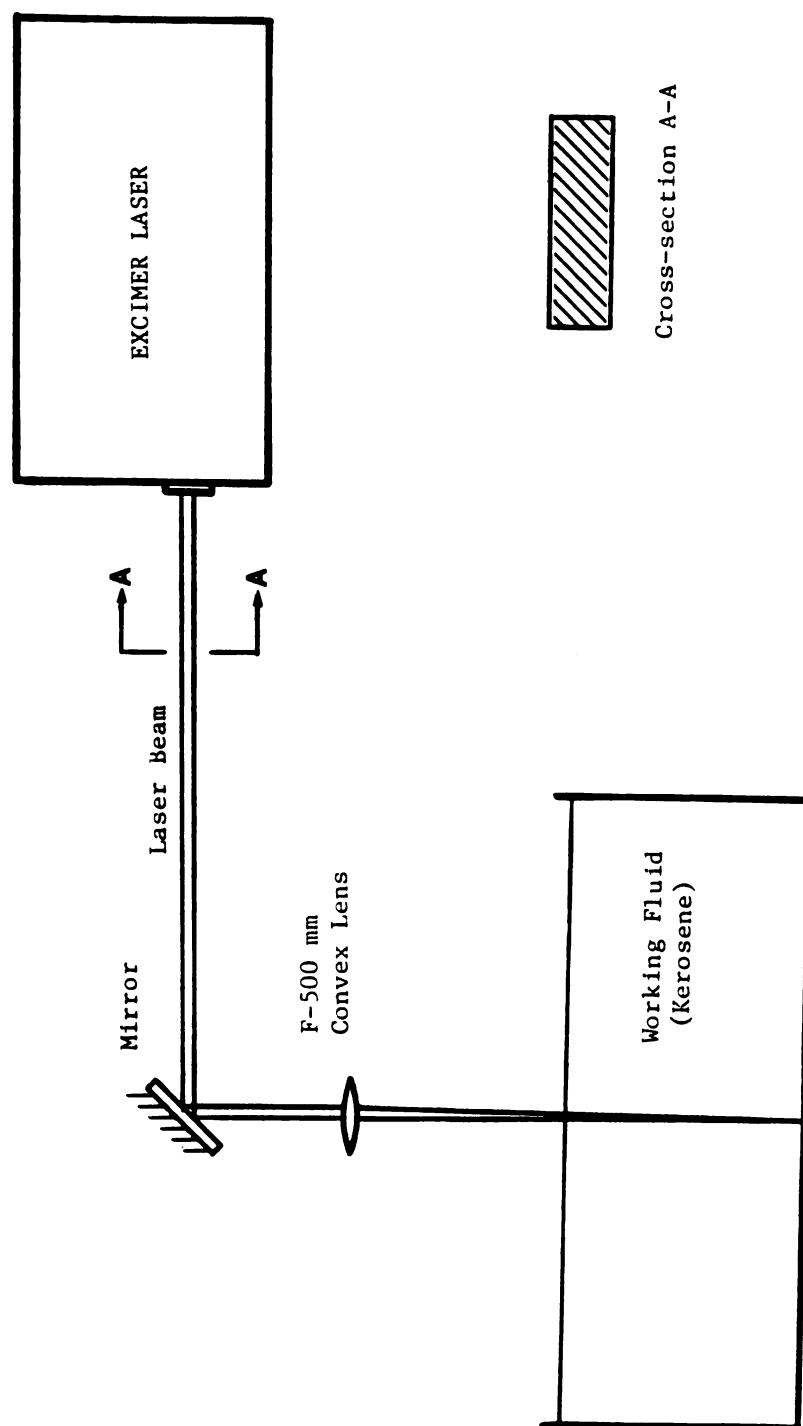


Fig. 2.4 A schematic of experimental configuration for one of the laser beam orientations.

351NM WAVELENGTH, 500 MM CONVEX LENS
 INPUT BEAM DIAMETER: \square - 20 mm, ∇ - 7 mm.

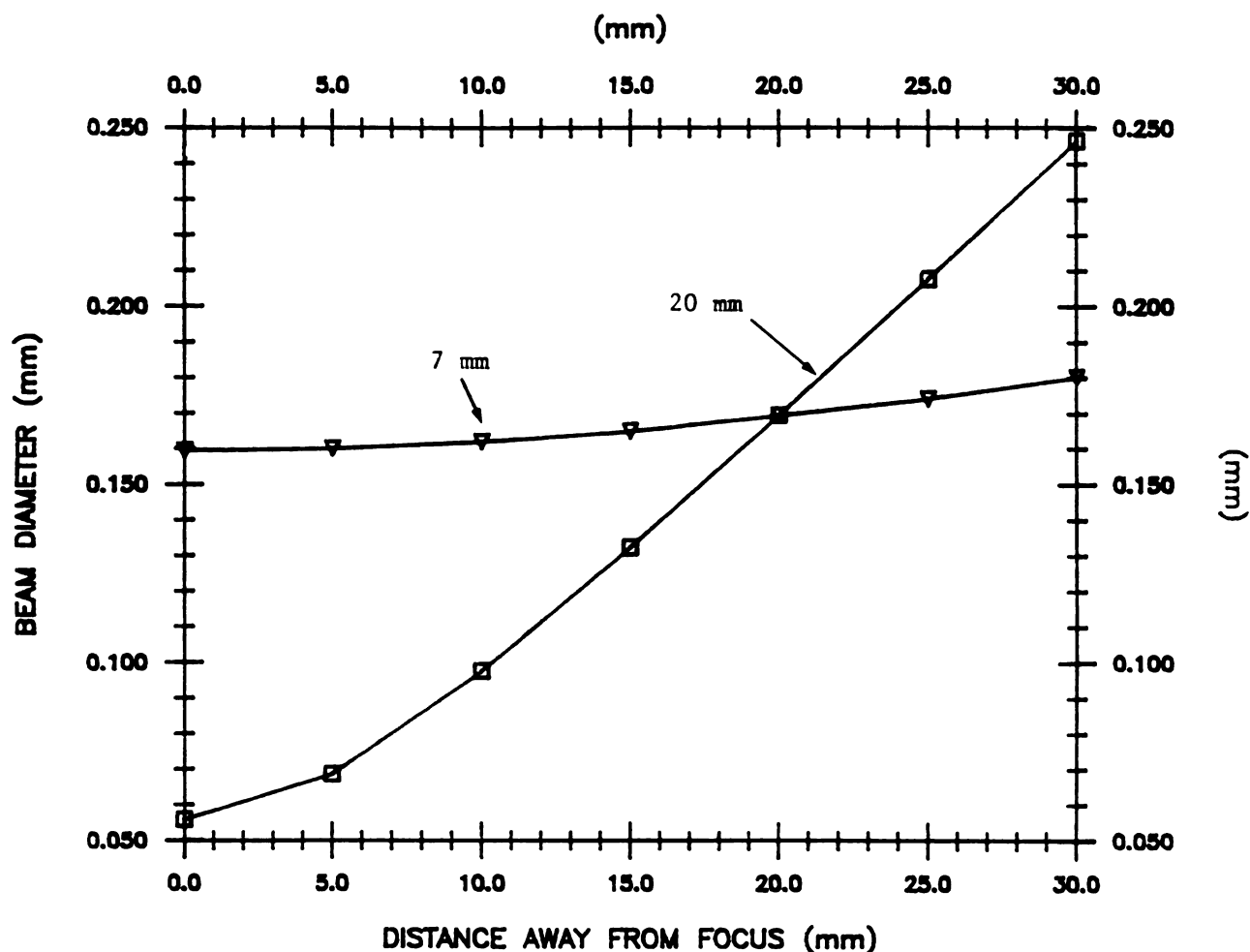


Fig. 2.5 The divergence characters of the laser beam after a F-500mm convex lens.

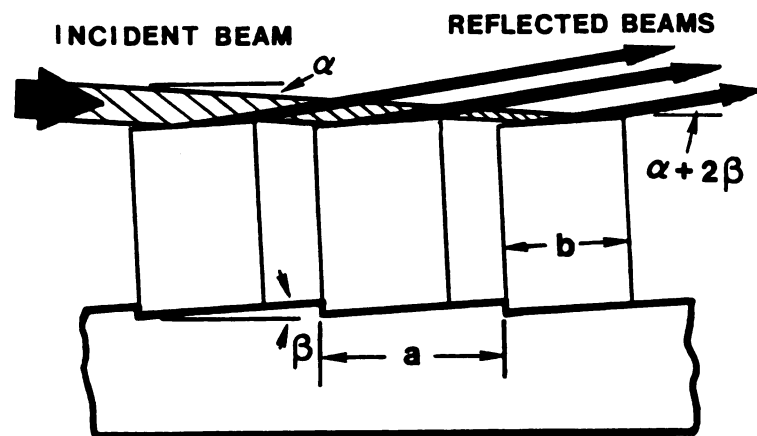


Fig. 2.6 The specular reflection from the beam divider.

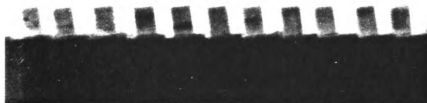


Fig. 2.7 A photo of the beam divider.

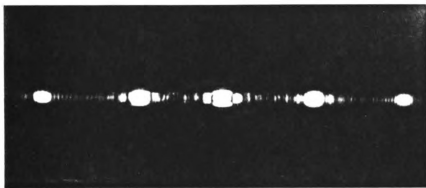


Fig. 2.8 A photo of the output of the divider showing the Fraunhofer diffraction.

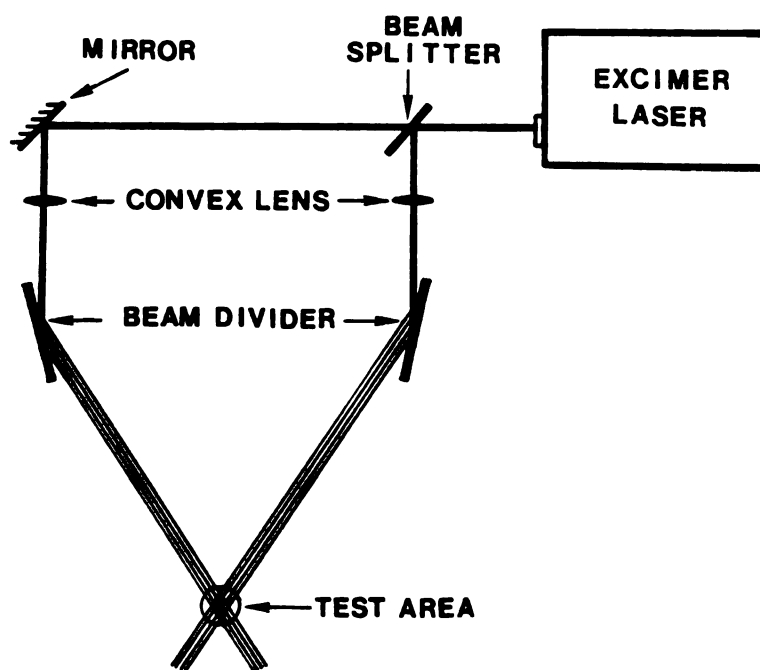
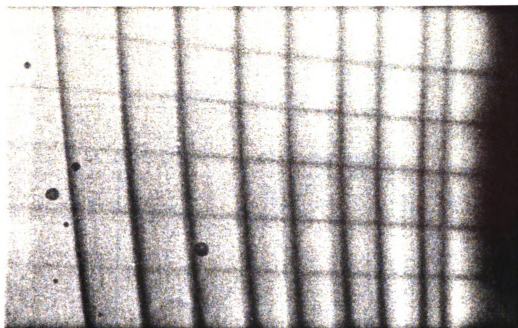
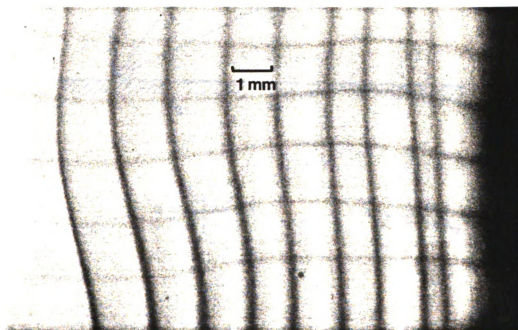


Fig. 2.9 A sketch of the optical configuration for generating a grid in Fig. 2.10 (a).

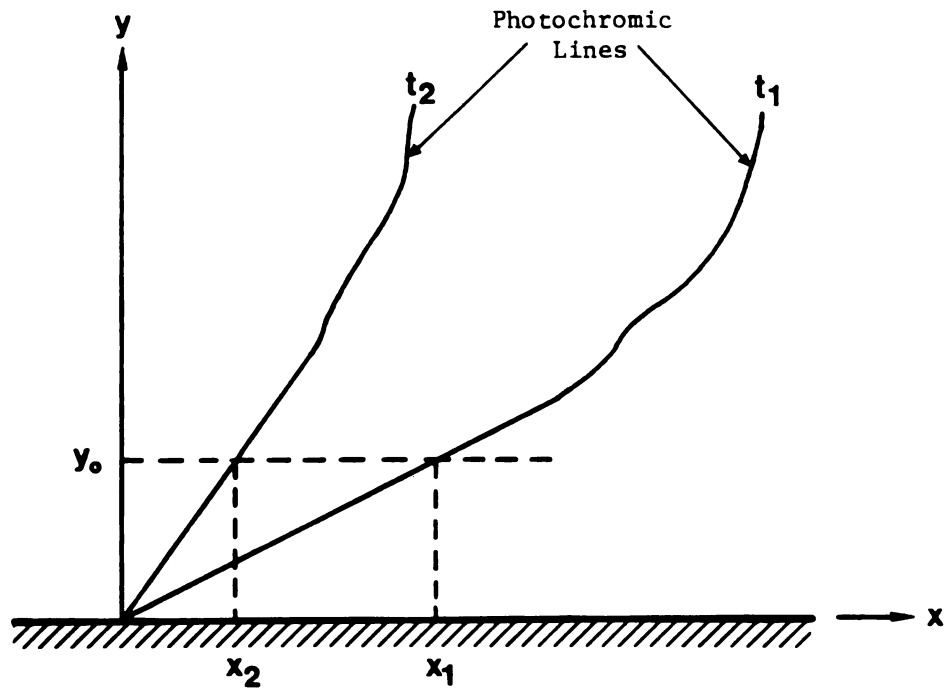


(a)



(b)

Fig. 2.10 A demonstration of the grid; a) shortly after the laser pulse, b) 0.4 seconds later.



$$u = \frac{x_1 - x_2}{t_1 - t_2}$$

$$\tau_w = \mu \left. \frac{\partial u}{\partial y} \right|_w \approx \mu \frac{u}{y_0}$$

Fig. 2.11 Algorithm to obtain the wall shear stress using photochromic technique.

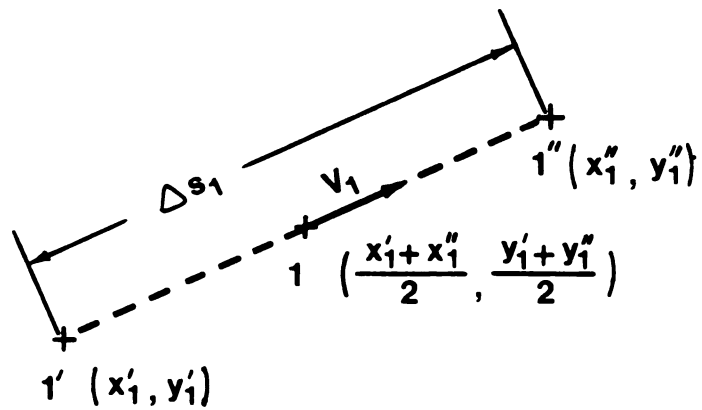
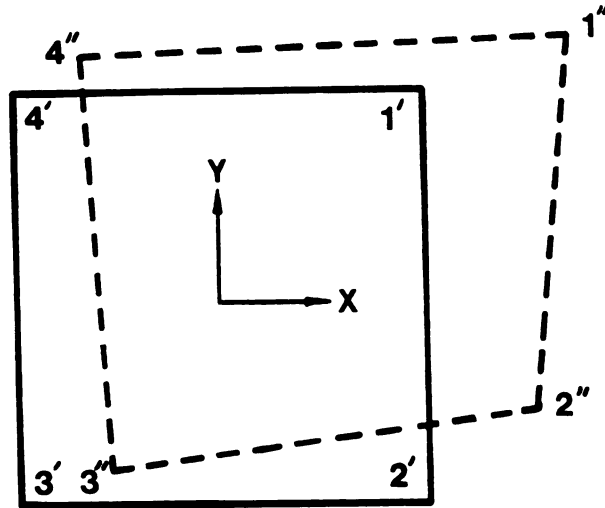


Fig. 2.12 Procedure for conversion of the displacement of a grid box to velocities.

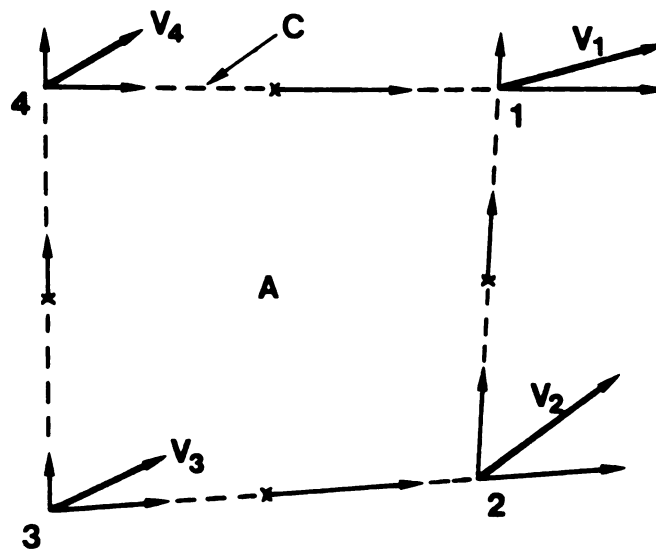


Fig. 2.13 Decomposition of the velocities used to calculate the circulation around a grid box.

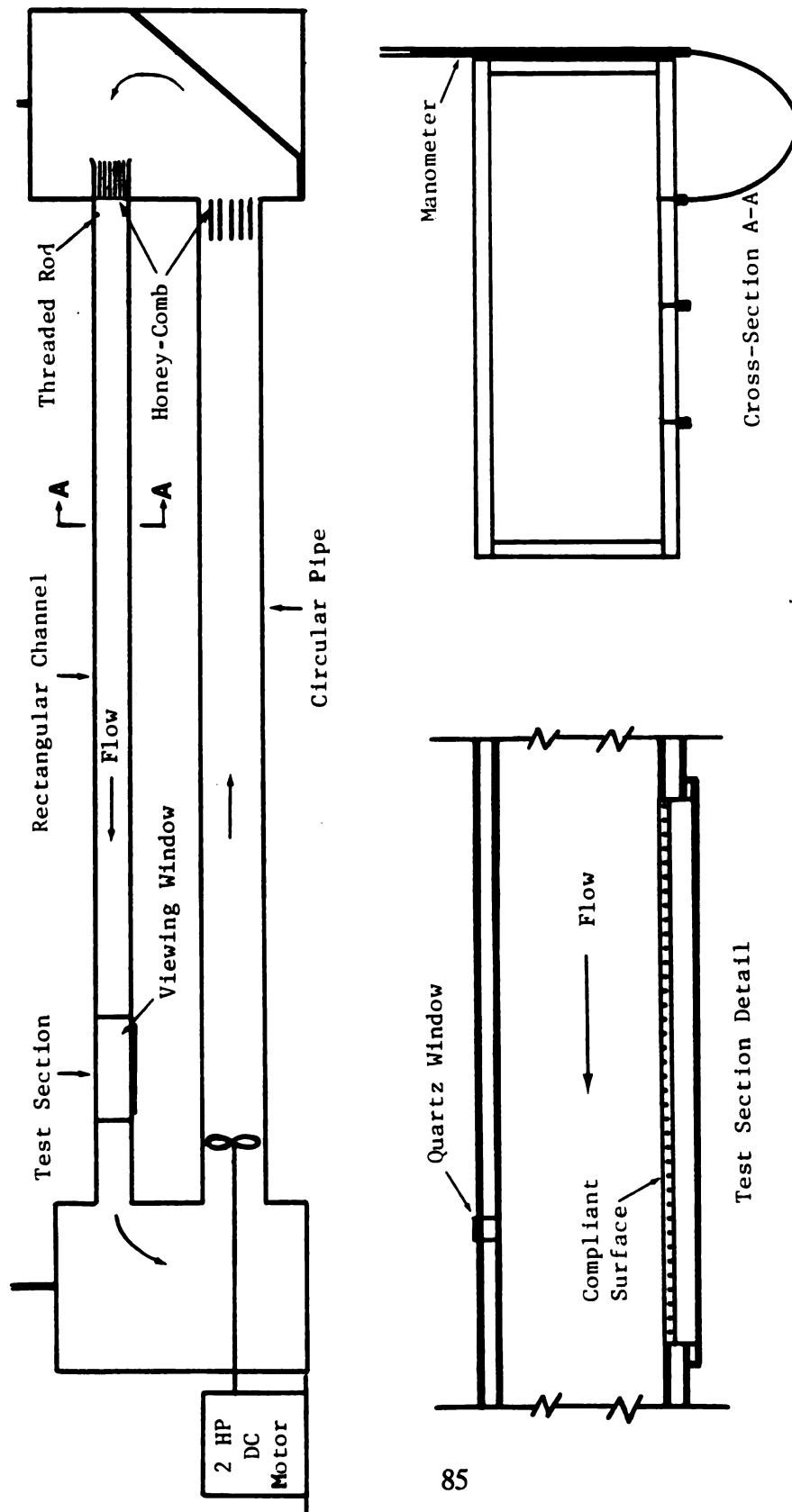


Fig. 3.1 A schematic of the kerosene channel flow facility.

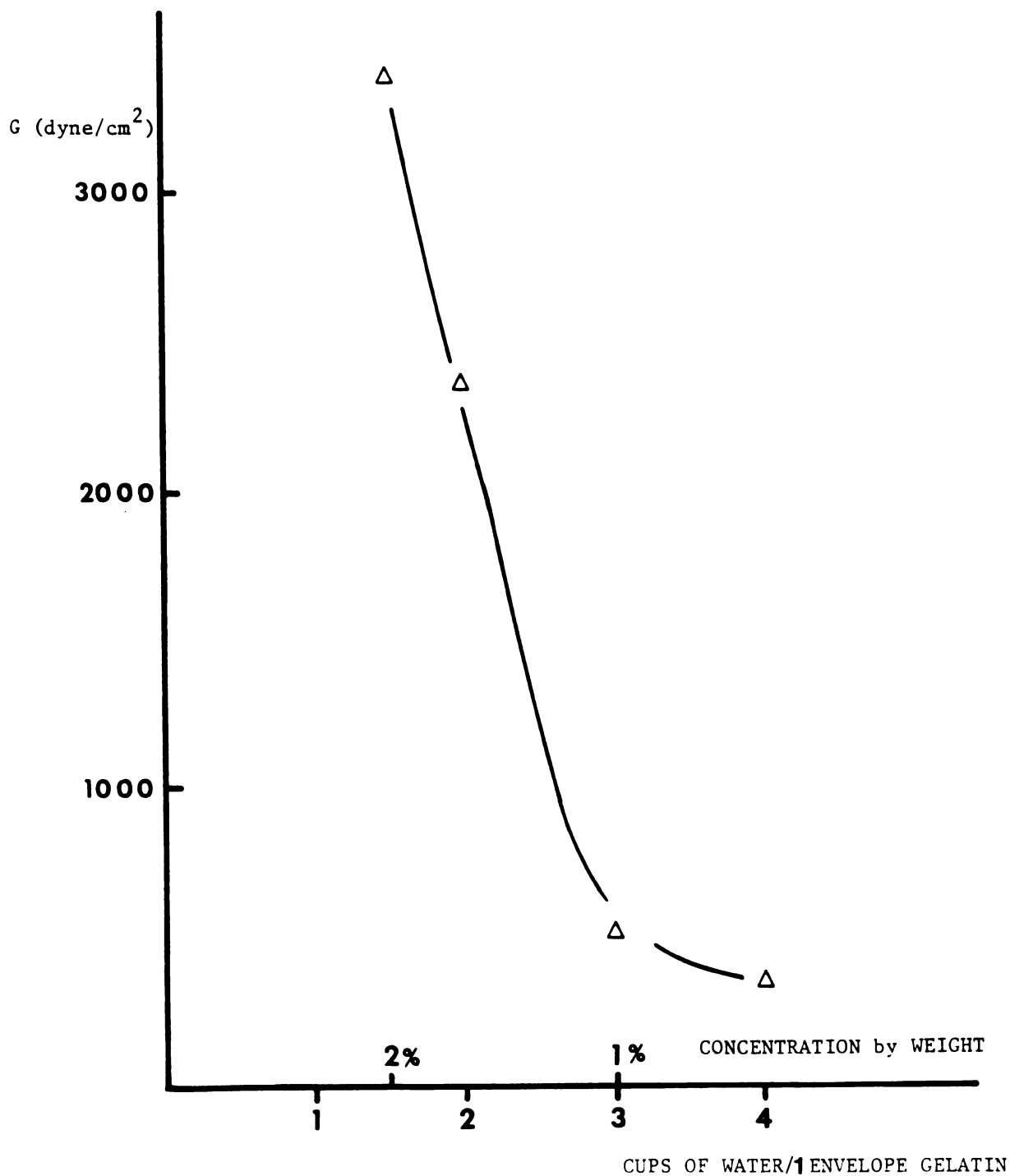


Fig. 3.2 The dependence of the shear modulus of gelatin on the concentration of gelatin and water mixture.

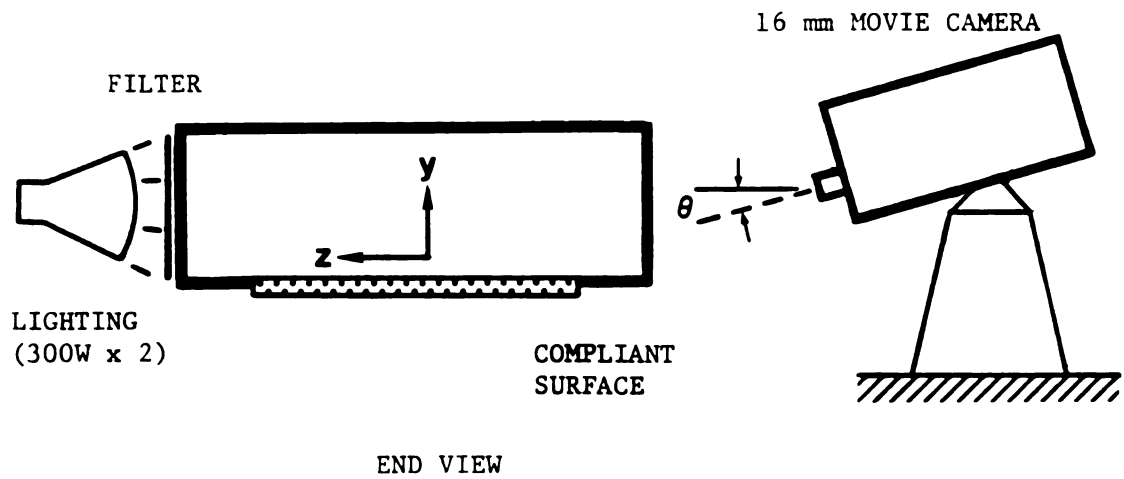


Fig. 3.3 A sketch of the experimental configuration used to capture the surface deformation under the turbulent channel flow.

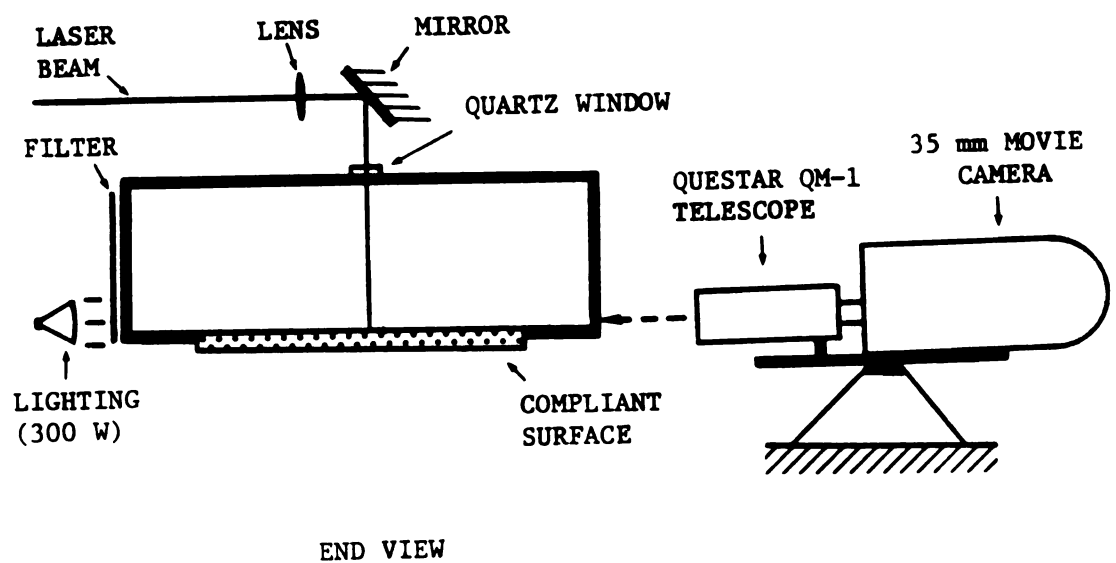


Fig. 3.4 The optical configuration of the wall shear stress measurement experiment.

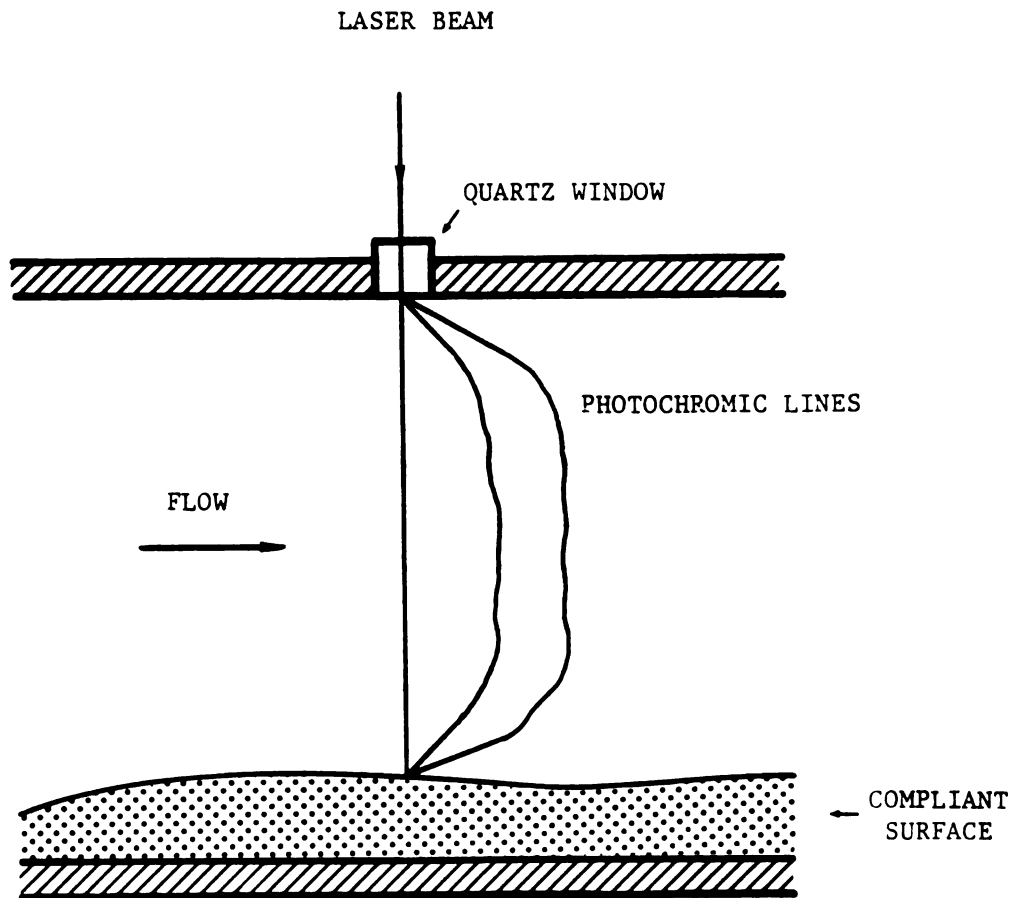


Fig. 3.5 A close-up of the technique used for the wall shear stress measurement on compliant surfaces.

INNERLAW VELOCITY PROFILE COLES $U+ = Y+ \text{ LINES}$ $R_\theta \approx 1200$

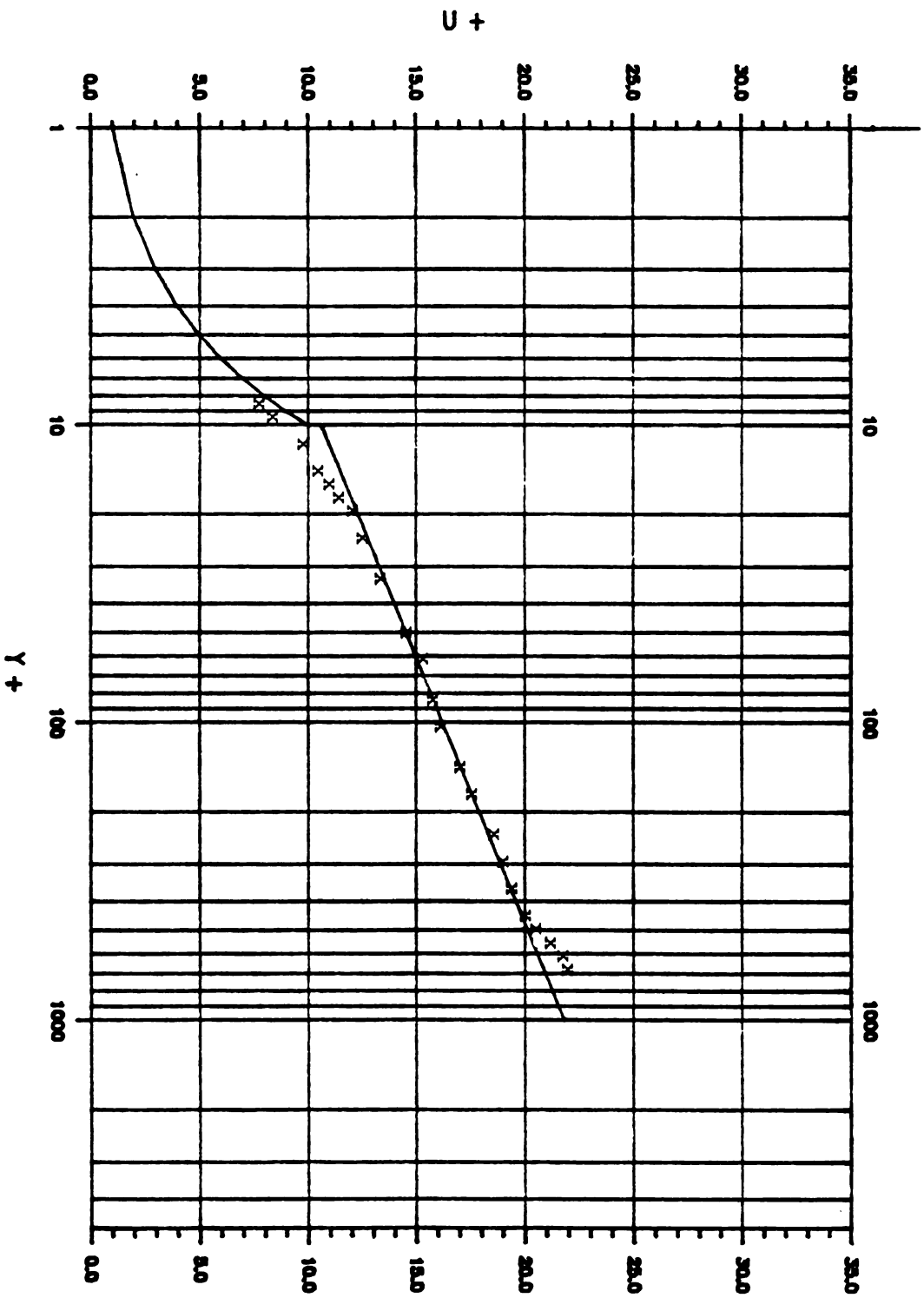


Fig. 3.6 The mean velocity profile over a stiff surface. (The centerline velocity is 0.341 m/sec yielding $R_\theta \approx 1200$).

$Re_u = \Delta: 11800 \text{ (Chu)}; x: 8200, 0: 5600 \text{ (Eckelmann)}$

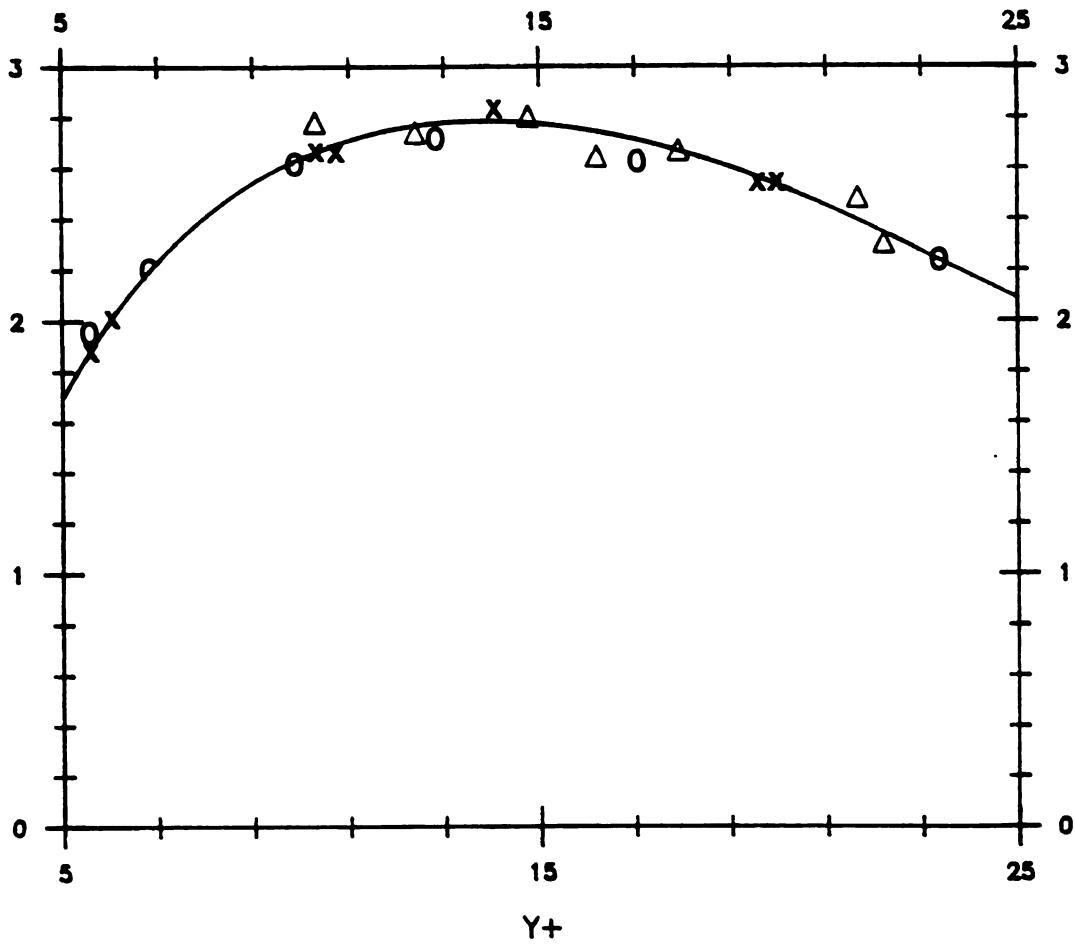


Fig. 3.7 The turbulent intensity profiles.

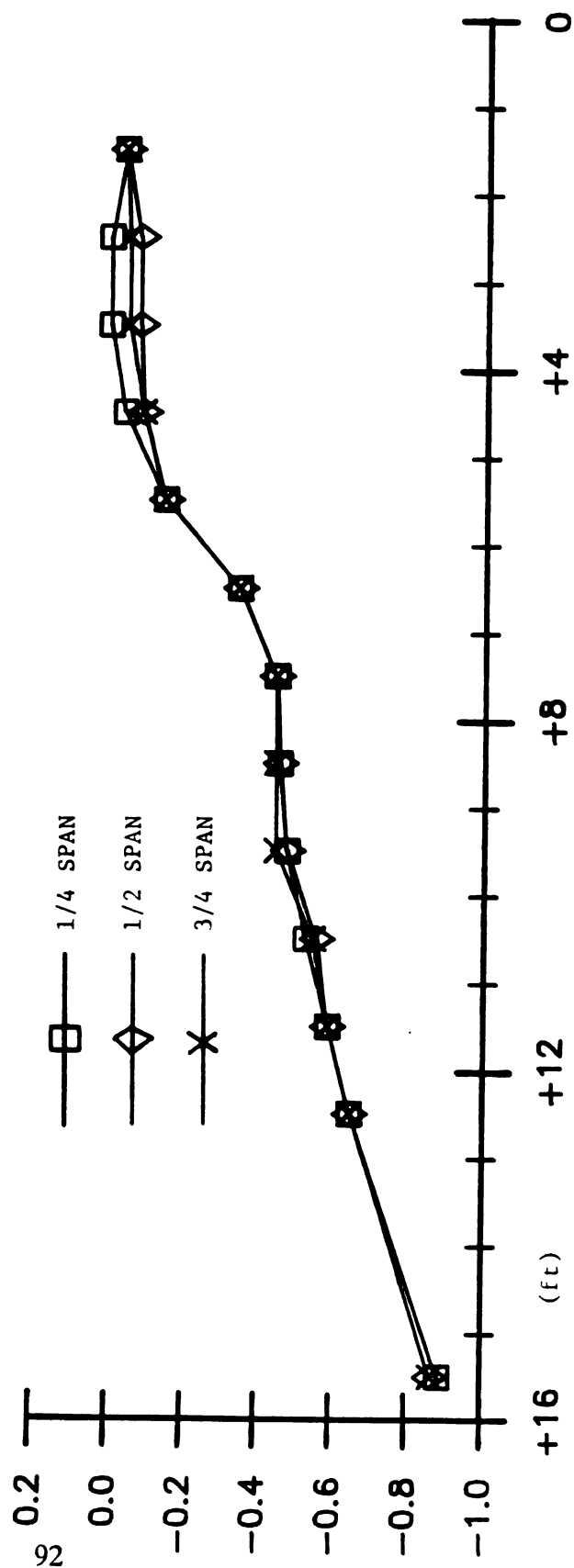
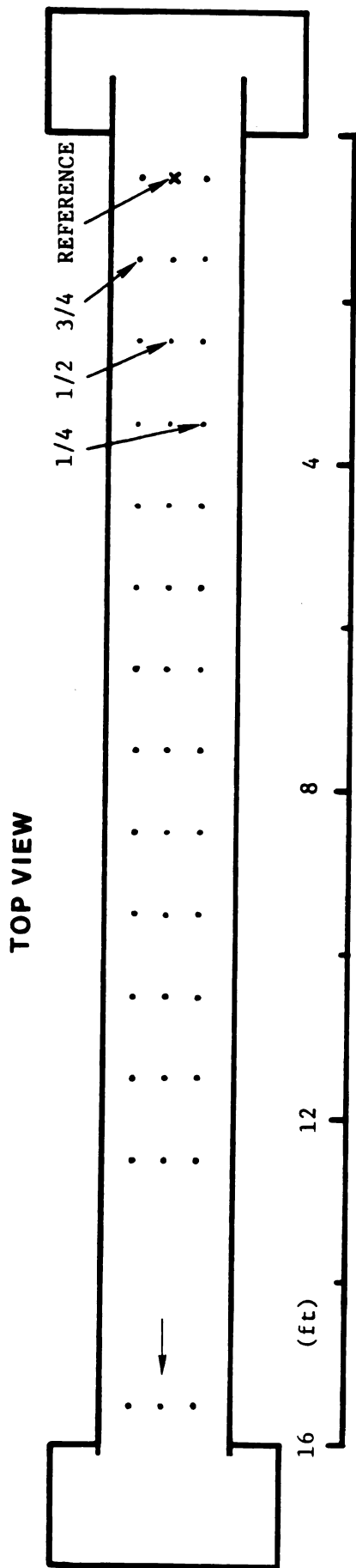


Fig. 3.8 The pressure distribution along the kerosene channel at $R_\theta \approx 1200$.

ONSET BOUNDARY WAVE.PDL

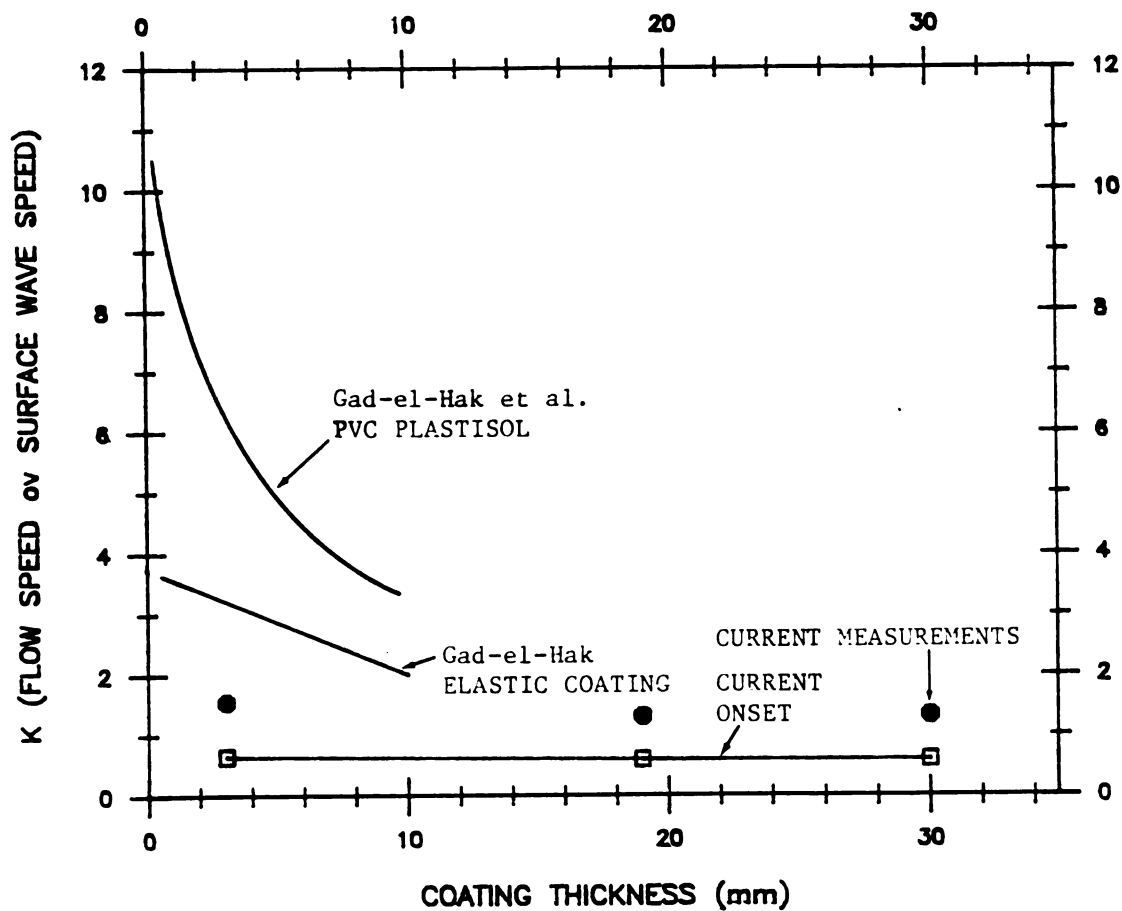


Fig. 3.9 The onset boundary for different compliant coatings.

SURFACE RESPONSE WAVE.PDL

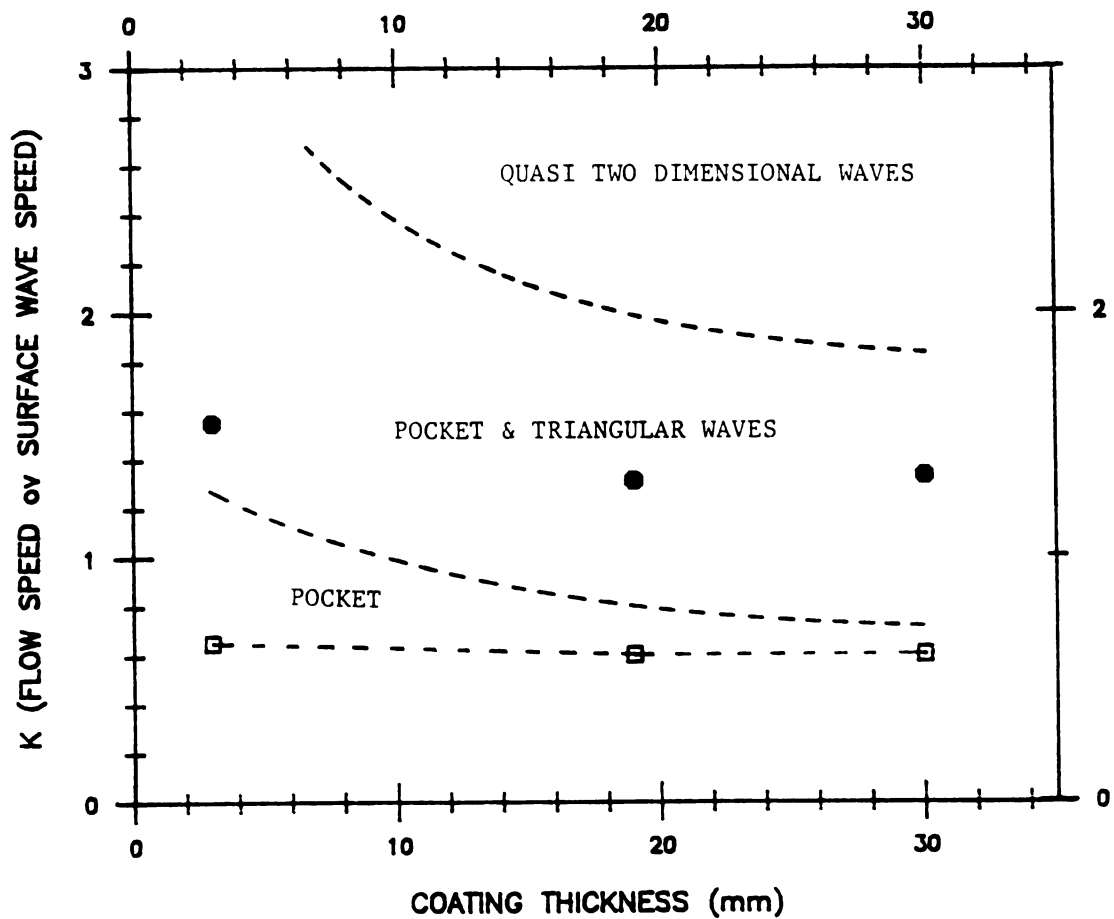


Fig. 3.10 The dependence of the occurrence of each element on both K and coating thickness.

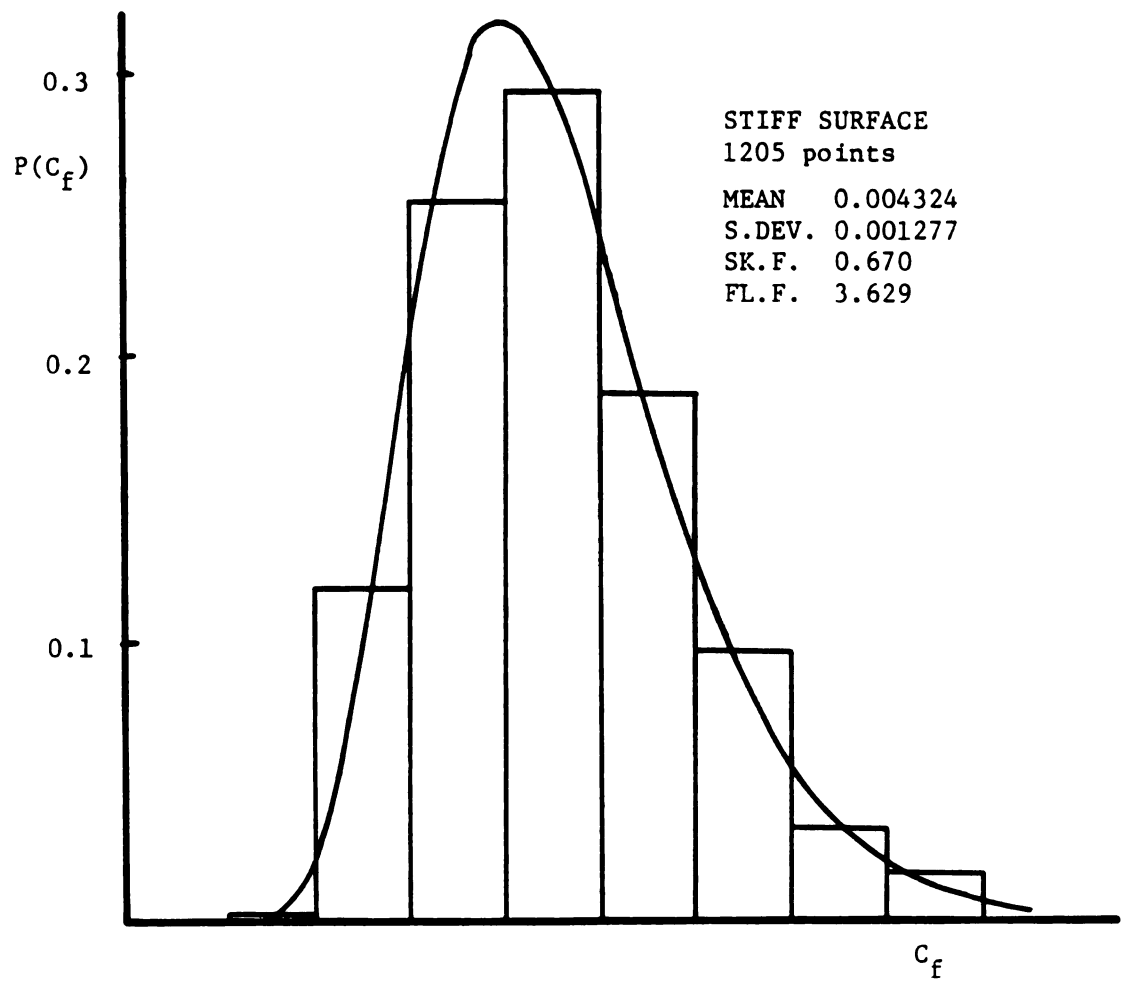
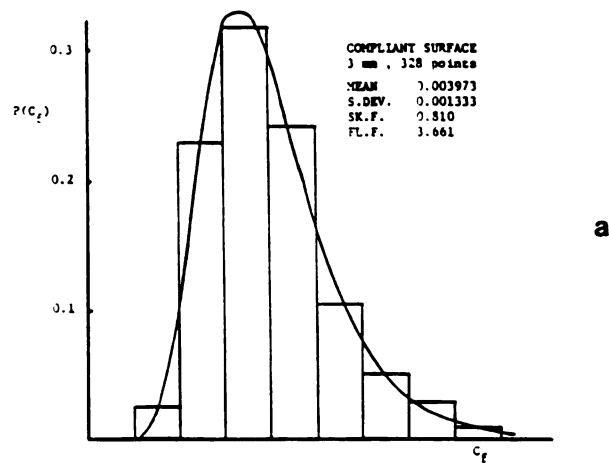
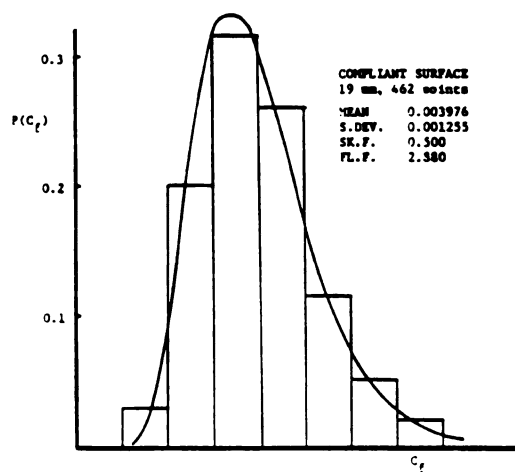


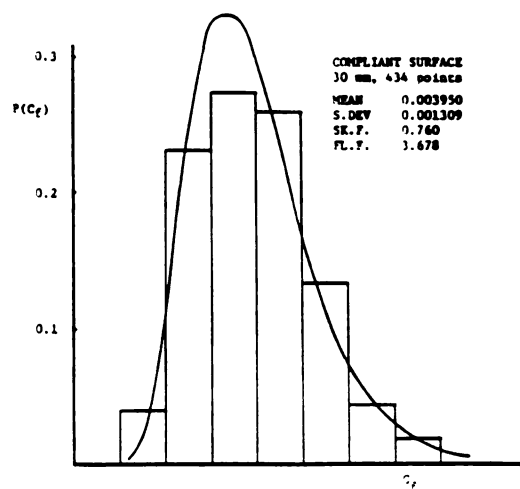
Fig. 3.11 The histogram of the skin friction obtained from 1205 samples over the reference stiff surface.



a



b



c

Fig. 3.12 The histograms of the skin friction associated with 3, 19 and 30 mm compliant coatings.

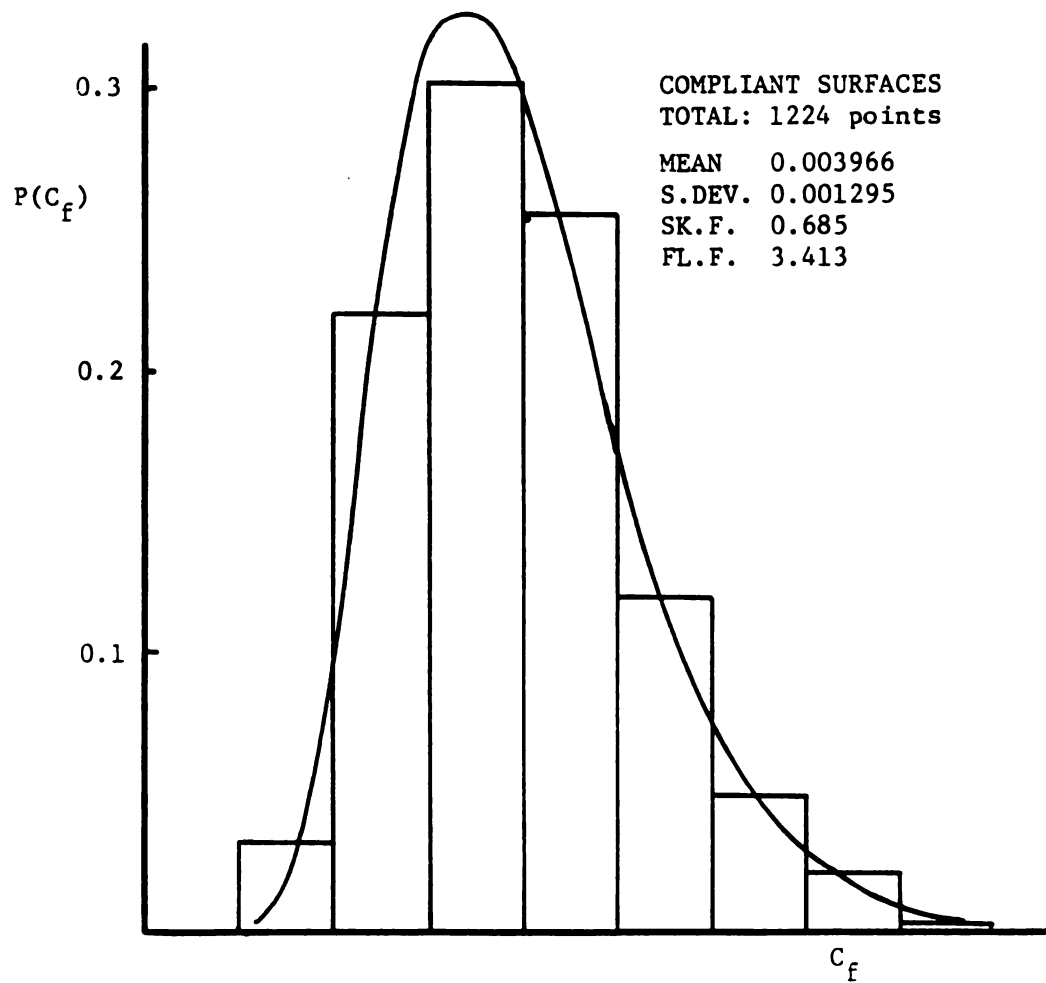


Fig. 3.13 The combination of Fig. 3.13 (a) through (c) regardless of thickness.

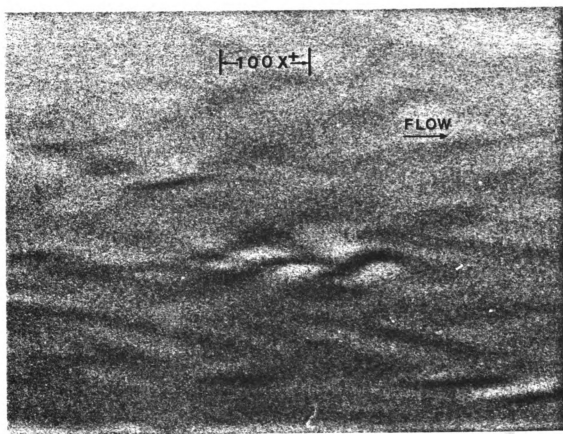


Fig. 3.14 A photo of the pocket-like depressions formed on the 3mm compliant surface.

TRANSVERSE LENGTH SCALE OF POCKET

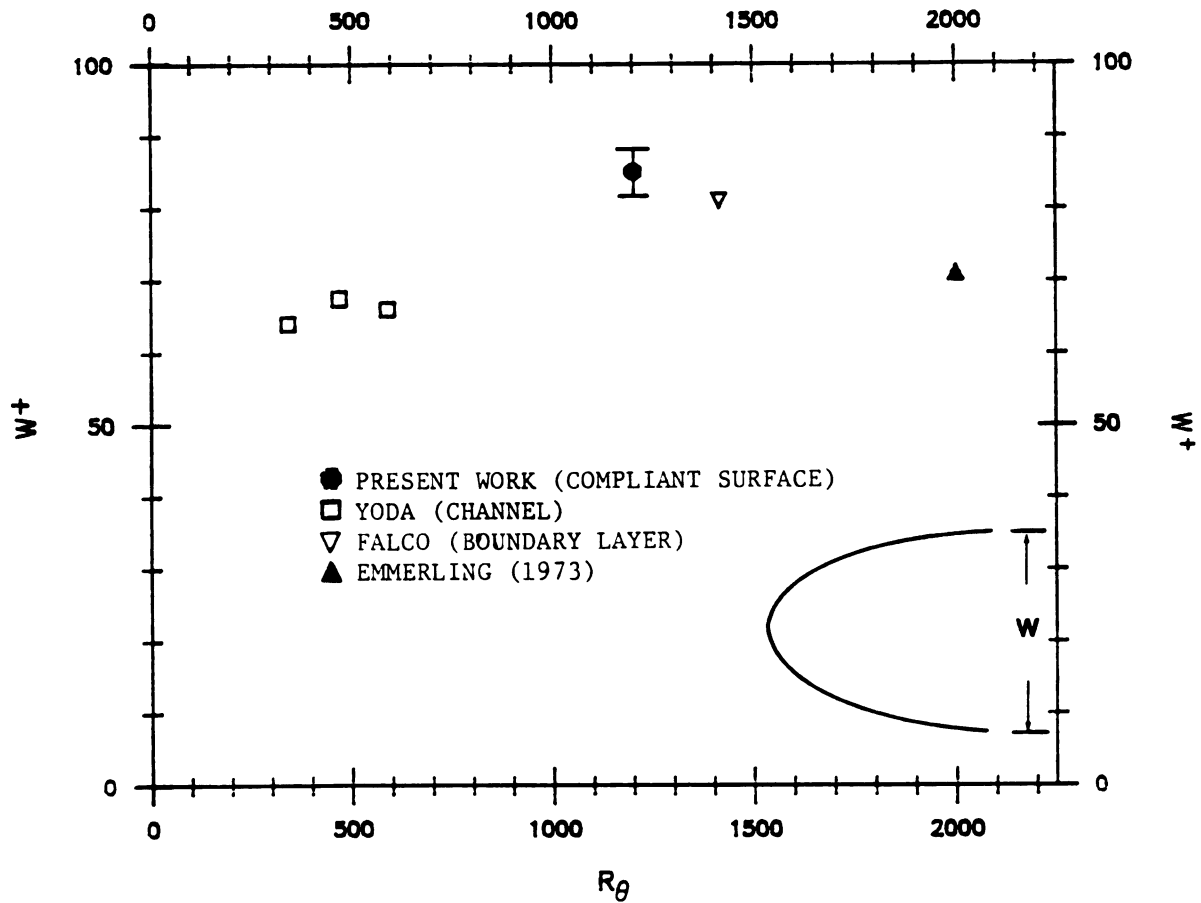


Fig. 3.15 The comparison of transverse length scale of depressions in compliant surfaces with the pocket footprints made on a solid surface.

TIME BETWEEN EVENTS

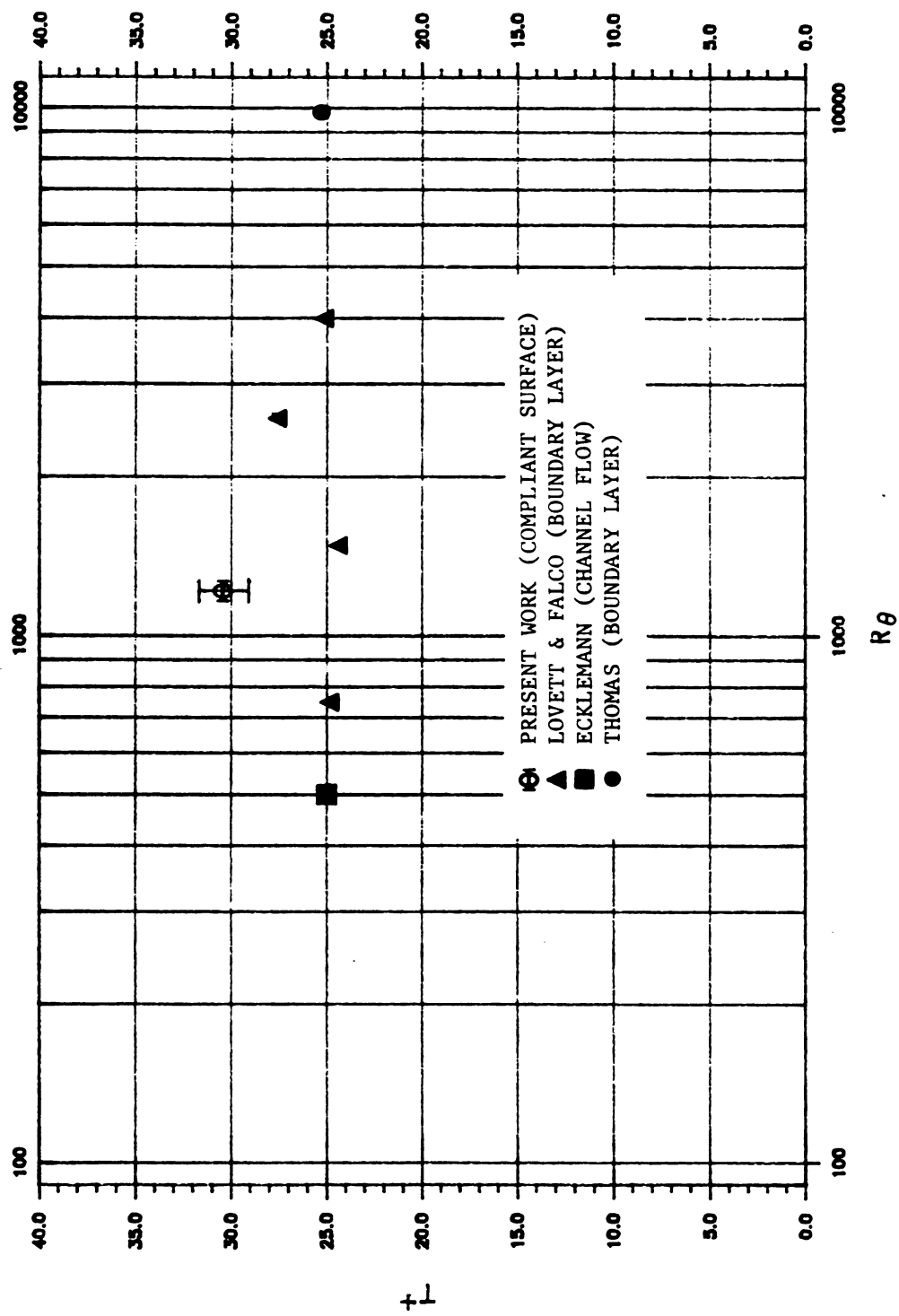


Fig. 3.16 The comparison of the time between pocket-like depressions in compliant surfaces with that obtained from boundary layer and channel flows.

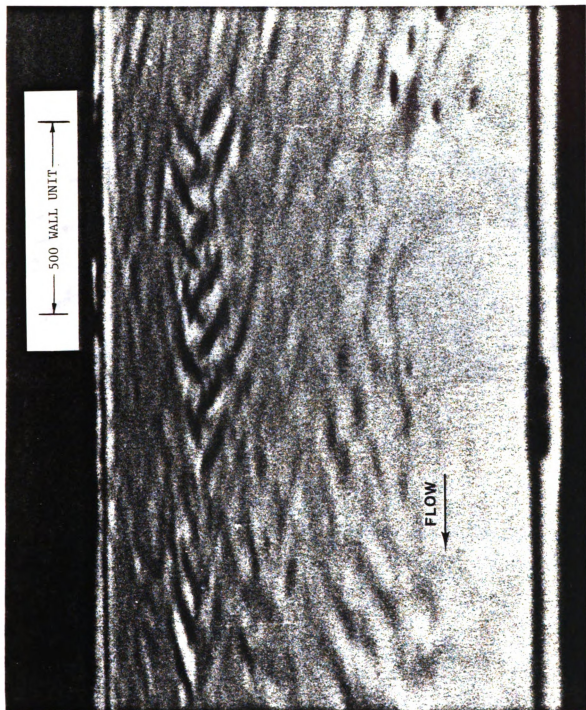


Fig. 3.17 A photo showing the triangle-like waves.

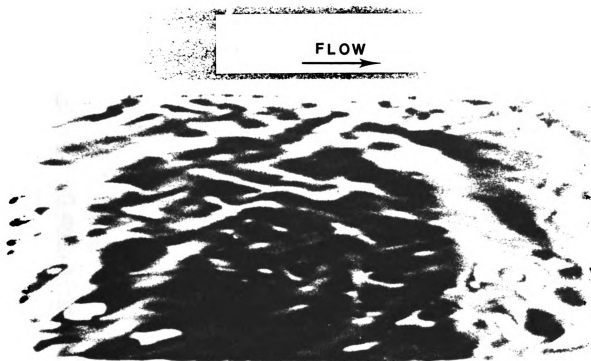
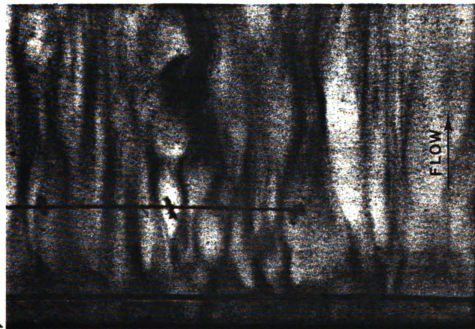
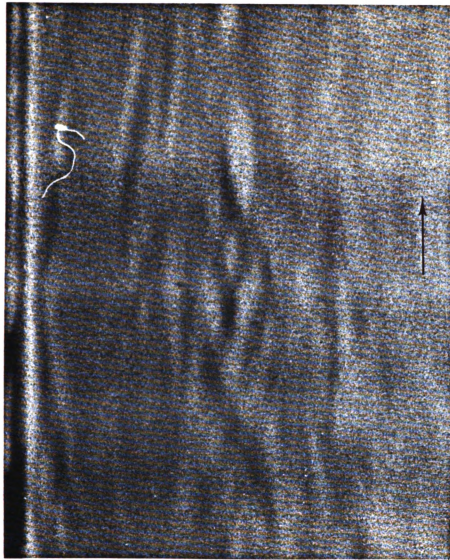


Fig. 3.18 A photo of the quasi two-dimensional large-scaled waves.

DYE SLIT



100 WALL UNIT



YODA (1981)

3mm COMPLIANT SURFACE

Fig. 3.19 A comparison of the visual phenomena on compliant surfaces with the flow visualization in the near wall region of channel flow by Yoda (1981).

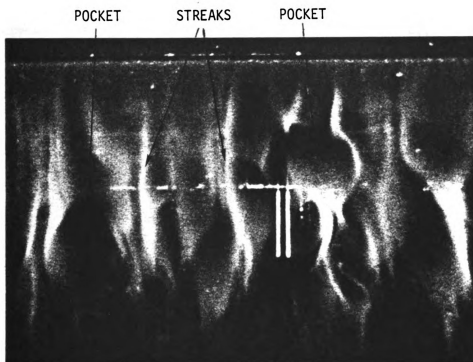
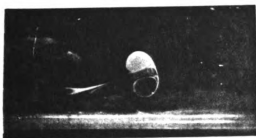
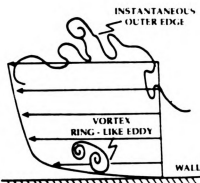


Fig. 4.1 Two pockets and a pair of streaks as seen in wall slit visualization of a turbulent boundary layer using smoke as the contaminant in air, the slit is at the top of the photo and the flow is from top to bottom. (Falco 1981)



a

Instantaneous turbulent boundary layer



b

Simulated vortex ring/wall shear layer



Fig. 4.2 The basic idea behind the simulation. Performing a Galilean transformation on the vortex ring/moving wall interaction makes in a model of the turbulent boundary production process; (a) instantaneous turbulent boundary layer; (b) simulated vortex ring/wall shear layer.

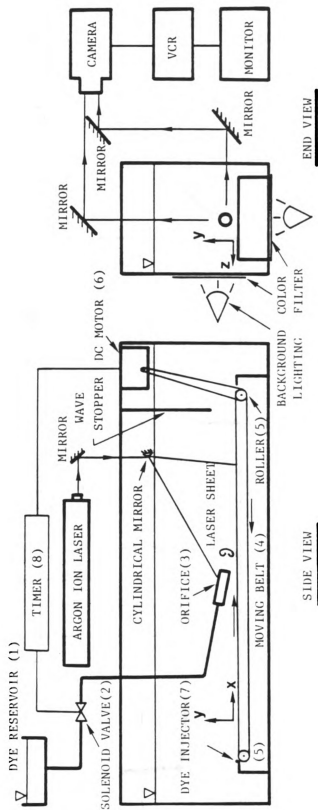


Fig. 4.3 A schematic of the side view and end view of the experimental apparatus used in the vortex ring/moving wall simulations.

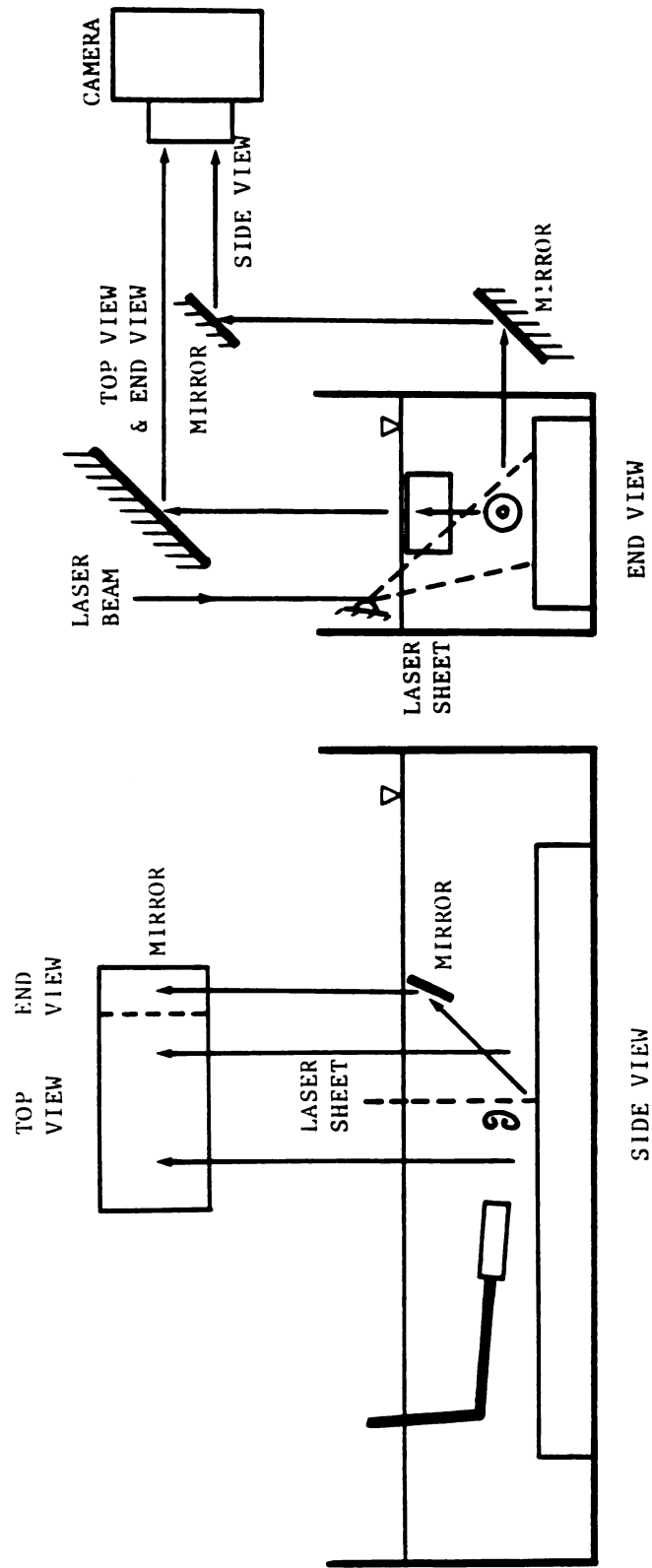


Fig. 4.4 A schematic of the three-view visualization system; note that only the end view was illuminated by the laser sheet.

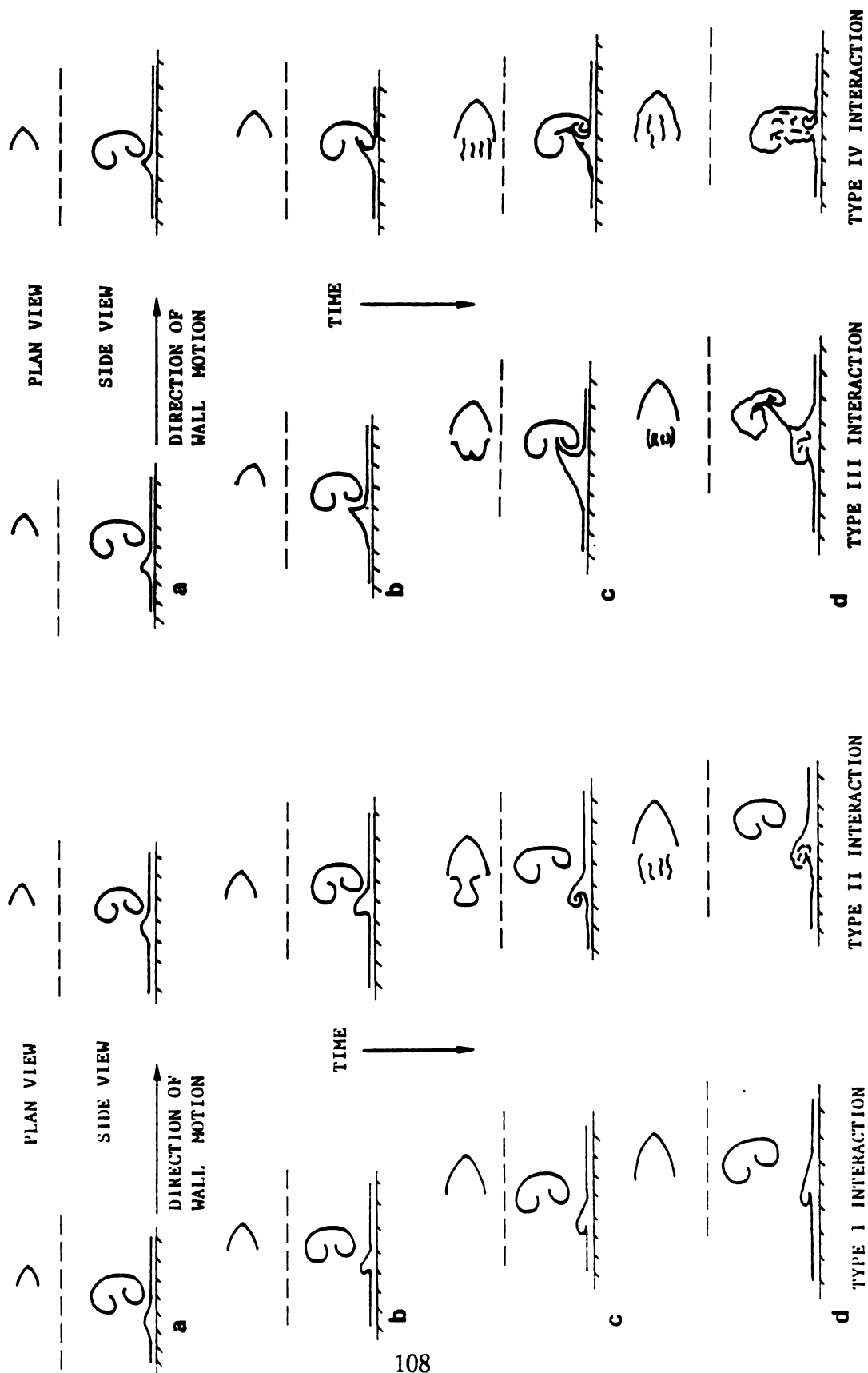


Fig. 4.5 Sketches of the four types of local vortex ring/moving wall interactions (see text for explanation).

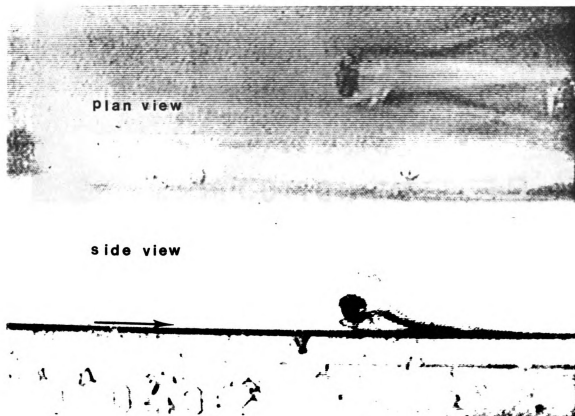


Fig. 4.6 Streaks form from the stretching of the lifted hairpin for $U_T/U_W \approx 0.8$.

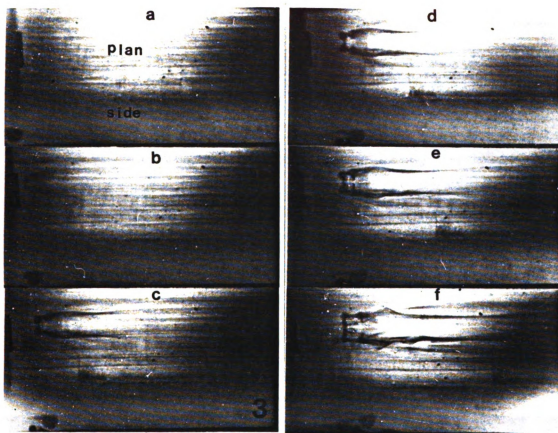


Fig. 4.7 Six photos of a vortex ring/moving wall interaction for $U_r/U_w < 0.35$ when the ring moves toward the wall at a 3 degree angle. Both plan and side views are shown. The ring and the wall are moving to the right and only the wallward side of the ring has dye in it. The interaction results in a pair of long streaks, a pocket and its associated hairpin lift-up, which then gets partially ingested into the ring.

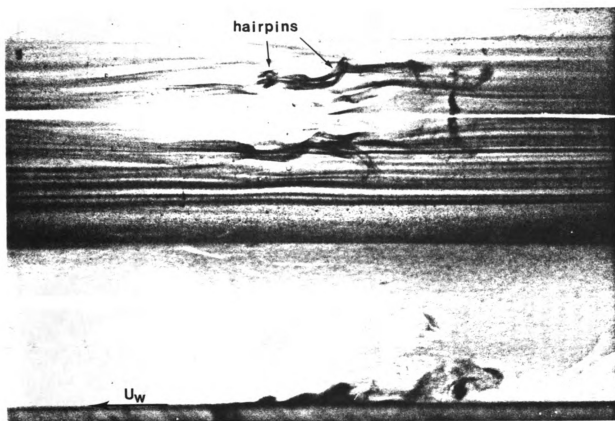


Fig. 4.8 Hairpins form over streaks.

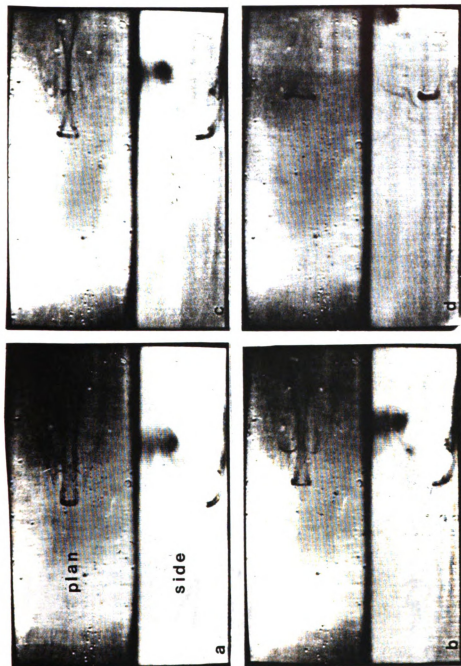


Fig. 4.9 Four photos of a vortex ring/moving wall interaction for $U_r/U_w > 0.45$ when the ring is moving away from the wall at a 2.5 degree angle. Both plan and side views are shown. The ring and the wall are moving to the right. A hairpin forms first. The long stable streaks which also form, come closer and closer together, indicating that the streamwise vorticity which caused them are of opposite sign. This evolution leads to "pinch-off" and the creation of a new vortex ring.

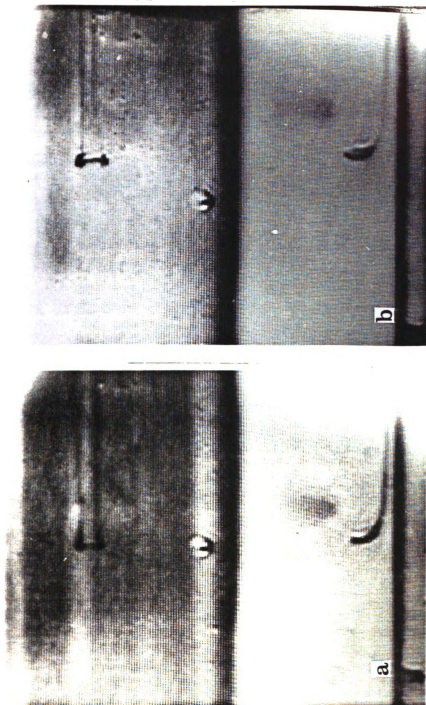


Fig. 4.10 Same conditions as Fig. 4.9, except that the wall layer is very thin. We obtain long stable streaks and a long stretched hairpin which does not pinch-off over 2500 wall layer distance of the facility. The time between each photo is approximately 50 wall units.

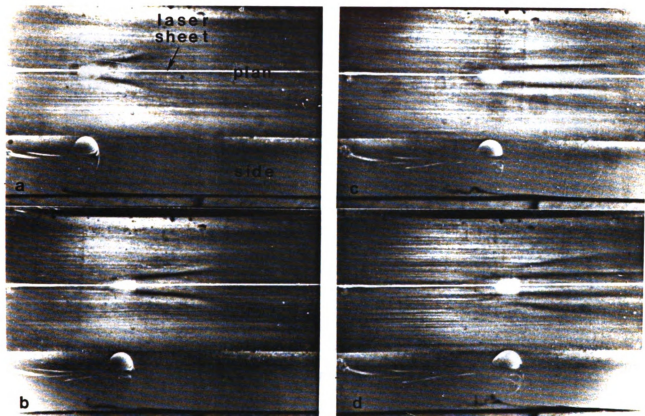


Fig. 4.11 Four photos of the evolution for $\delta/D > .15$. In this case a pocket does not form, and it appears that the hairpin has been generated by the initial vortex ring/wall interaction.

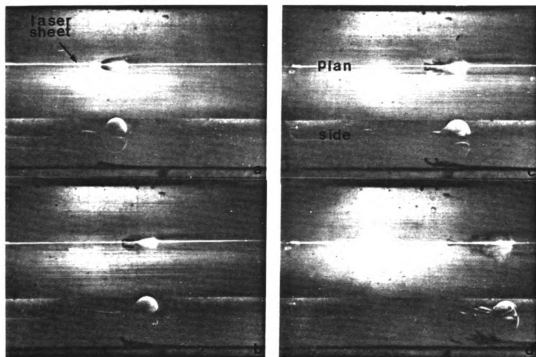


Fig. 4.12 Four photos of the interaction for $\delta/D < .15$. In this case pinch-off of a portion of the lifted hairpin does occur, creating a new small vortex ring.

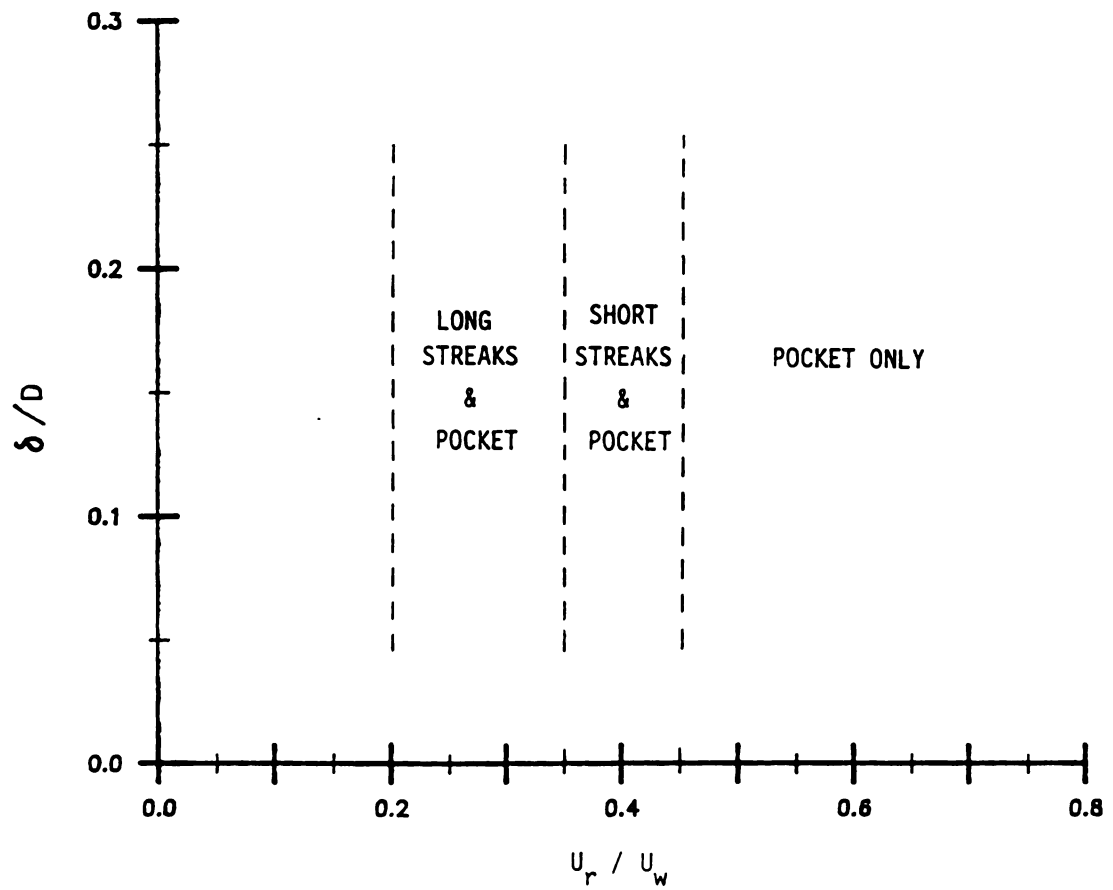


Fig. 4.13 The dependence of the formations and evolutions of streaks on δ/D and U_r/U_w for $D^+ > 250$ and a 3 degree incidence angle. The indicated boundaries between different evolutions are approximate.

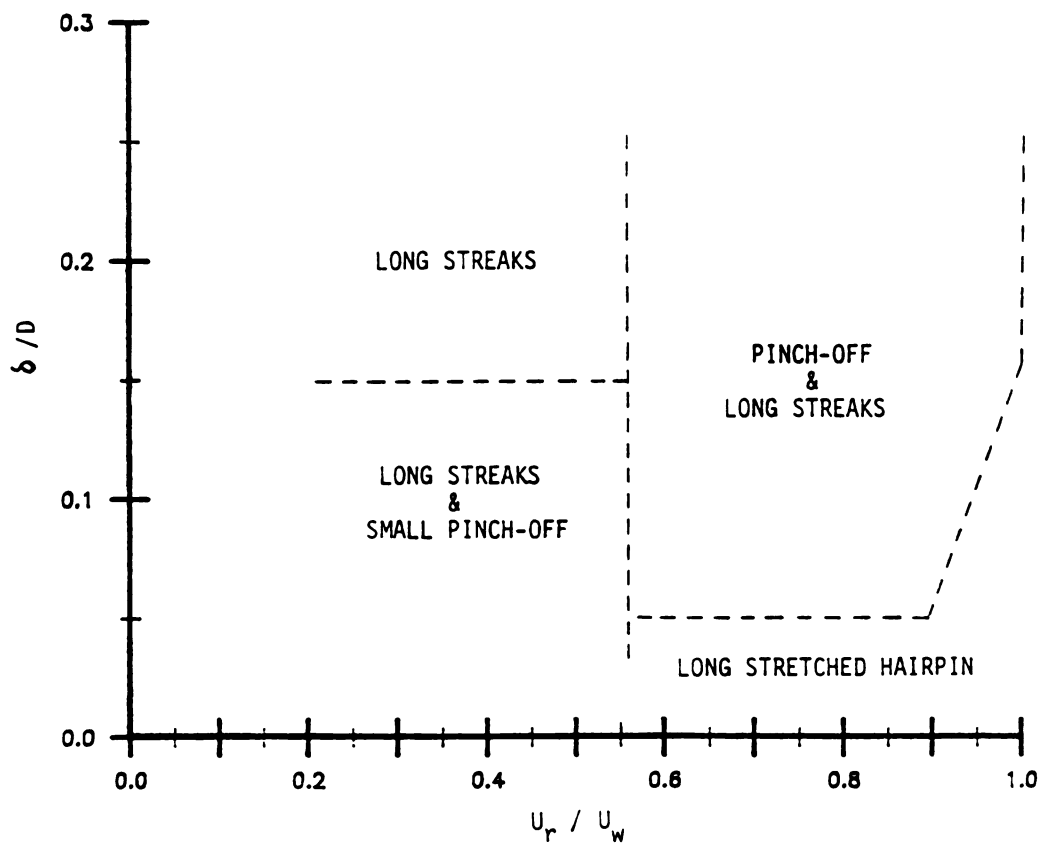


Fig. 4.14 The dependence of δ/D on U_r/U_w for rings moving away from the wall at 2.5 degrees. δ/D now plays a much more important role, and long streaks are generated over the entire speed ratio range studied.

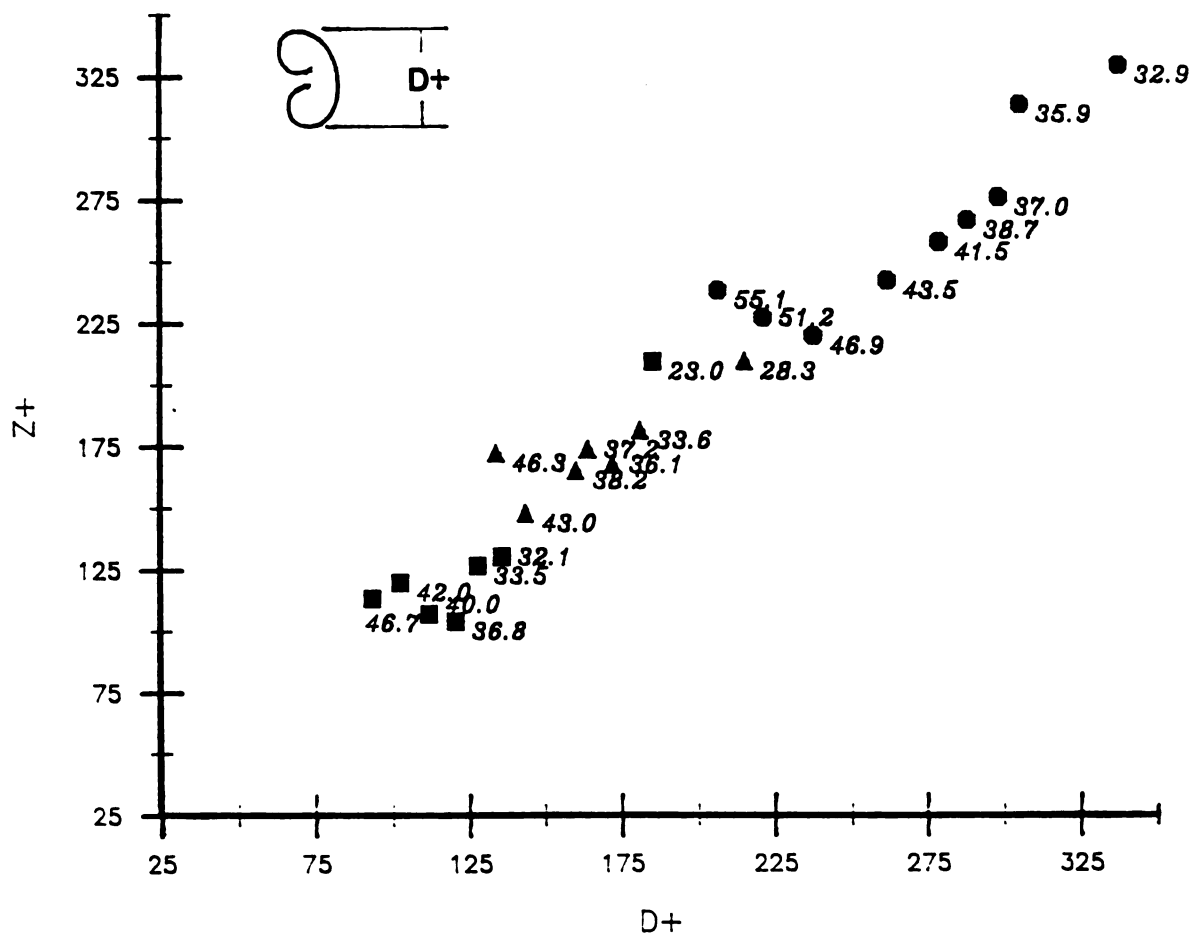


Fig. 4.15 The dependence of the streak spacing in wall units on the size of the vortex ring in wall units, for an incidence angle of 3 degrees and $U_r/U_w = .31$. The thickness of the wall layer (in wall units) is shown next to each data point.

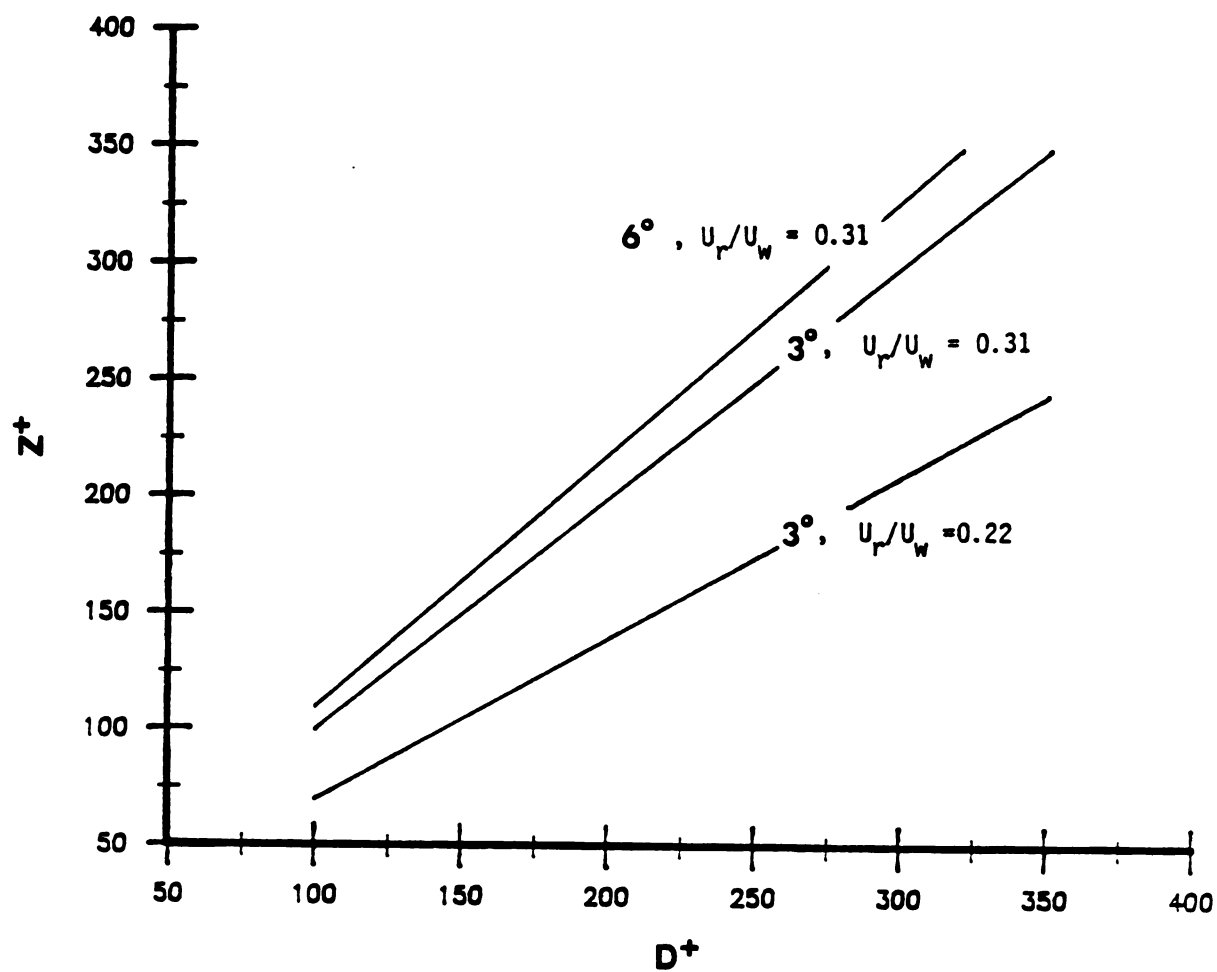


Fig. 4.16 The dependence of the streak spacing on the speed ratio and angle.

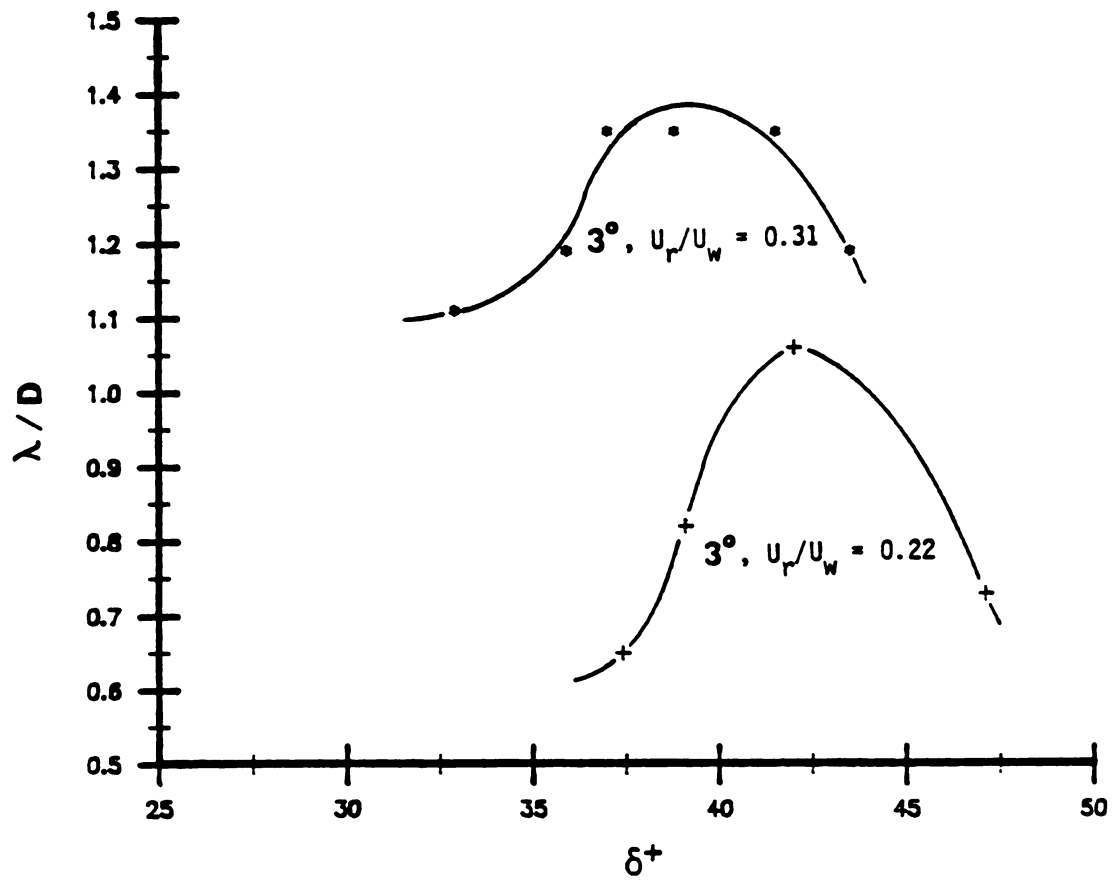


Fig. 4.17 The non-dimensionalized streamwise wavelength that sets in as a function of δ^+ for different U_r/U_w and angles.

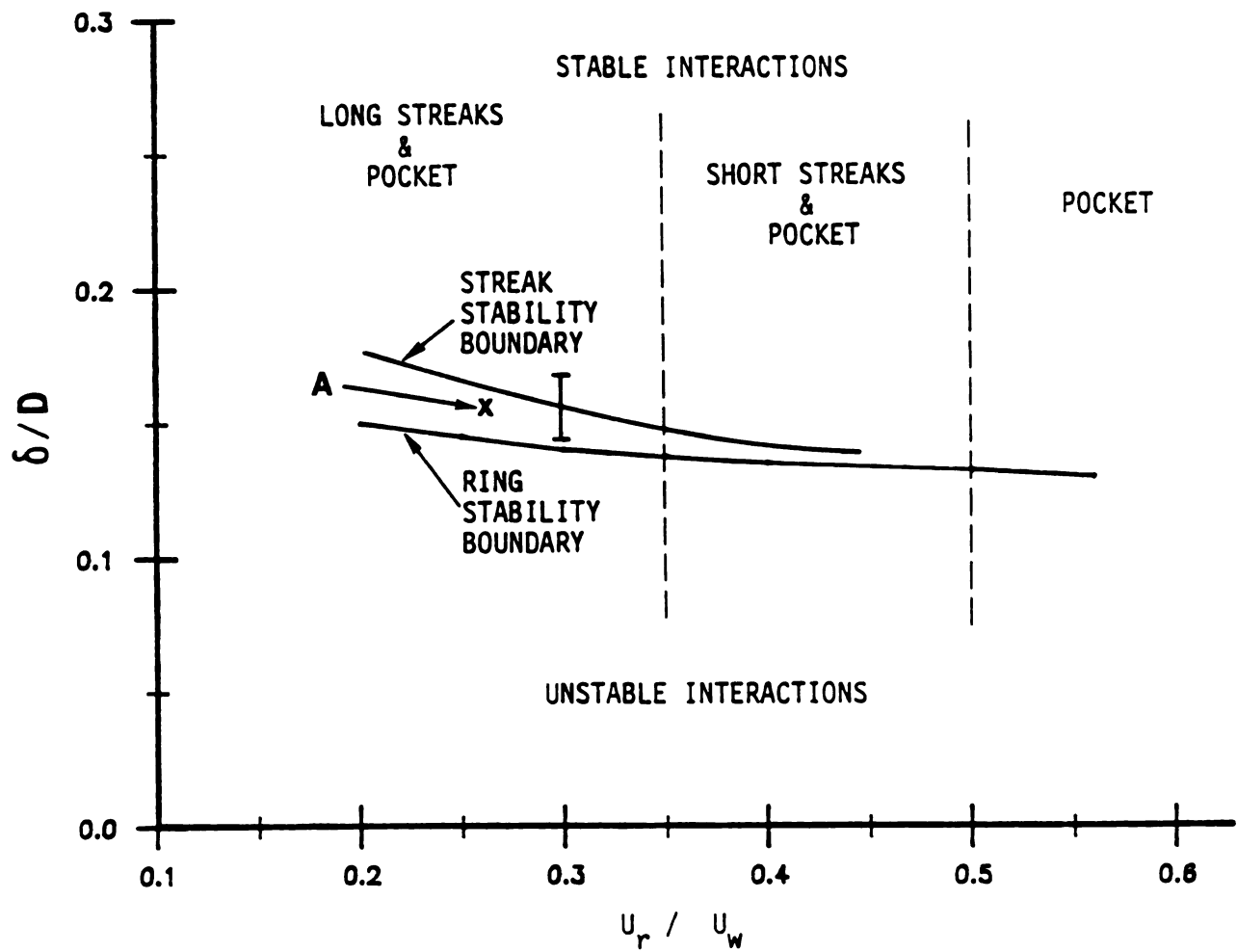


Fig. 4.18 A comparison between ring and streak stability the of a three degree ring moving towards the wall.

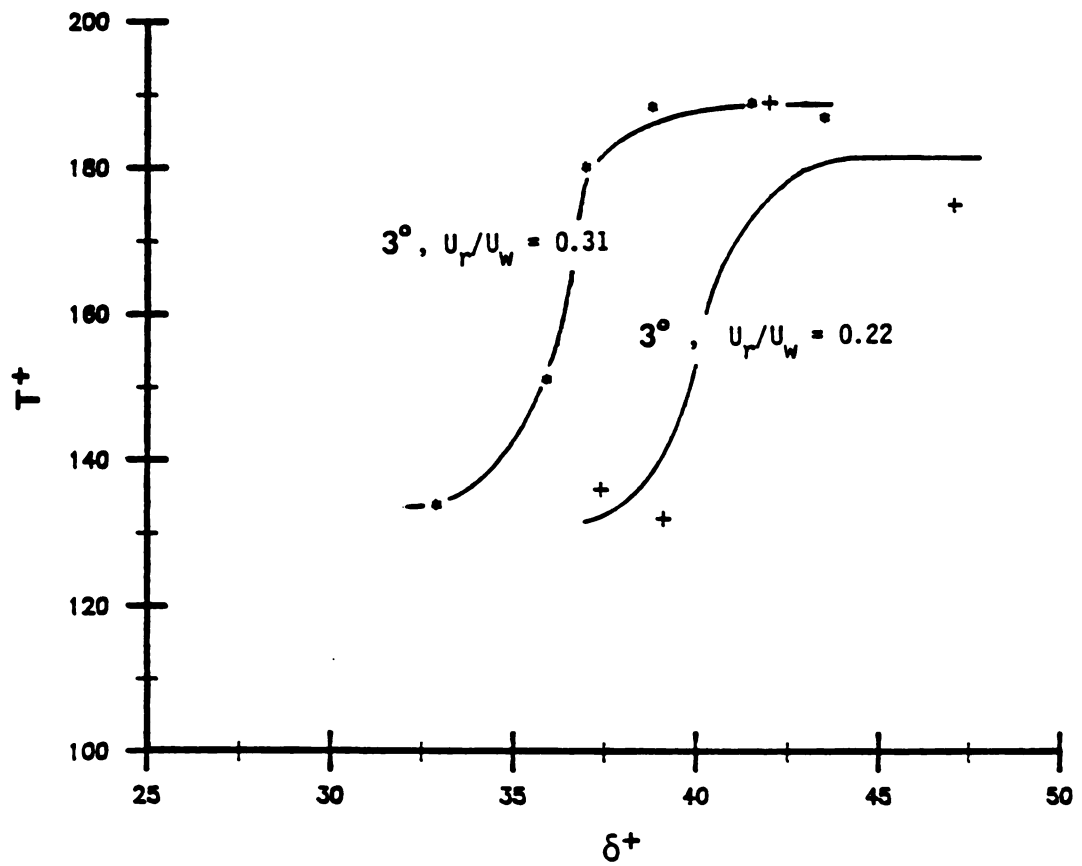
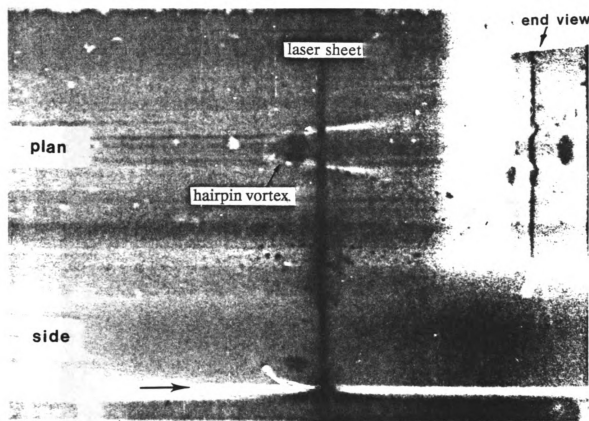
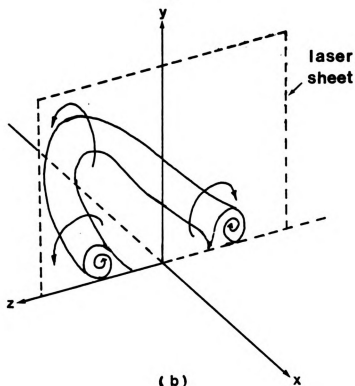


Fig. 4.19 The dependence of the time to instability of the streaks on the wall layer thickness (both quantities are non-dimensionalized by wall layer variables) for three degree incidence rings.



(a)



(b)

Fig. 4.20 (a) A photo of a hairpin vortex in three-view flow visualization;
(b) A sketch of the vortical motion of the hairpin vortex;
note that the arrows indicate the sign of rotation

end view

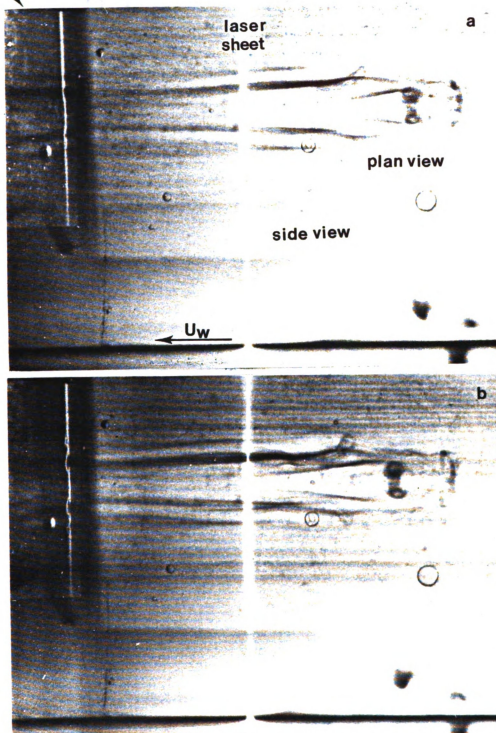


Fig. 4.21 Four photos of the three-view visualization; each photo is 10 t^+ apart.

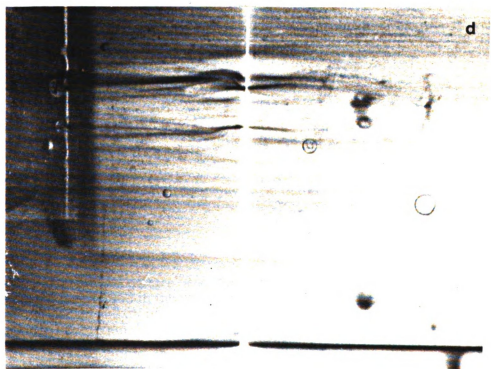
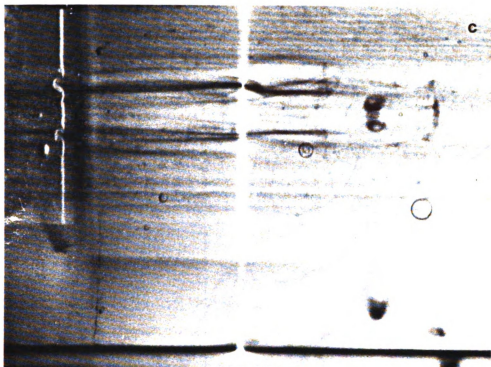


Fig. 4.21 Cont.

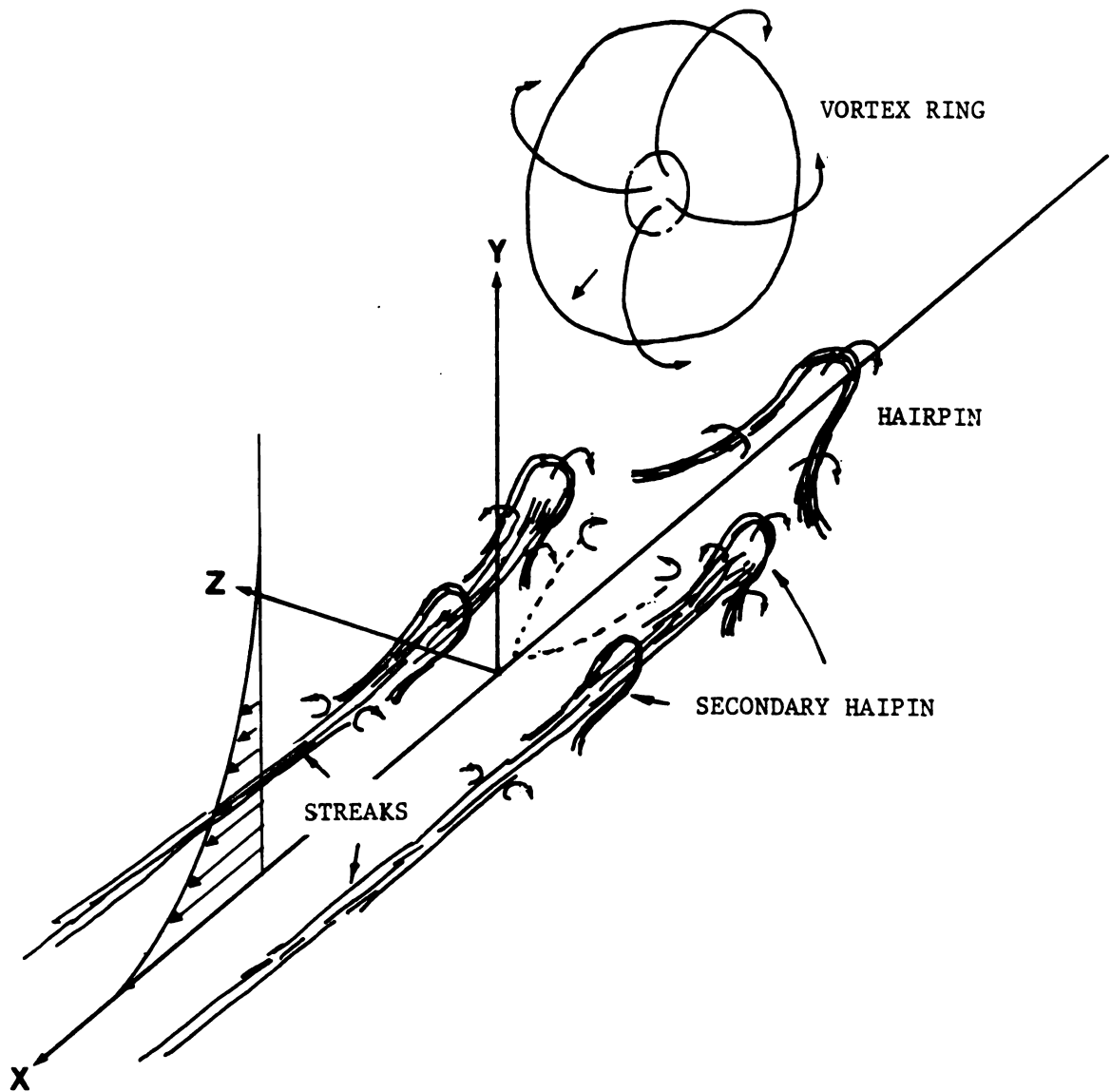


Fig. 4.22 A conceptual picture describing the spatial relationship of the formation of visual features observed in the vortex ring/moving wall interaction including the main hairpin vortex, secondary hairpin vortices, long streaks, and pocket; the arrows indicate the local flow direction.

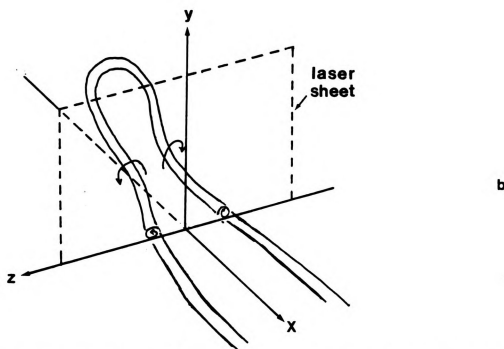
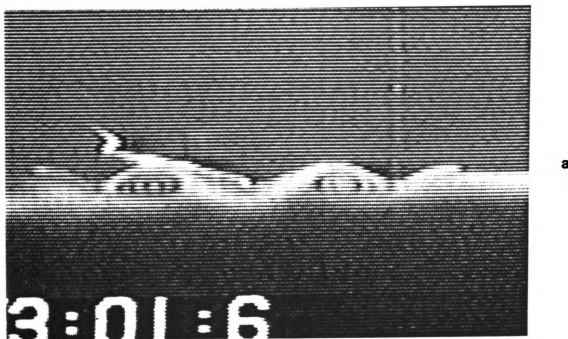


Fig. 4.23 A photo showing the laser illuminated end view flow visualization for a fast ring moving away from the wall. The observed long streaks were just the legs of the lifted hairpin vortex; they were one unit. The dye marker actually concentrated within the streamwise vortices. The sign of the vorticity shown in Fig. 4.23 (b) is consistent with that associated with the hairpin vortex shown in Fig. 4.20 (b).

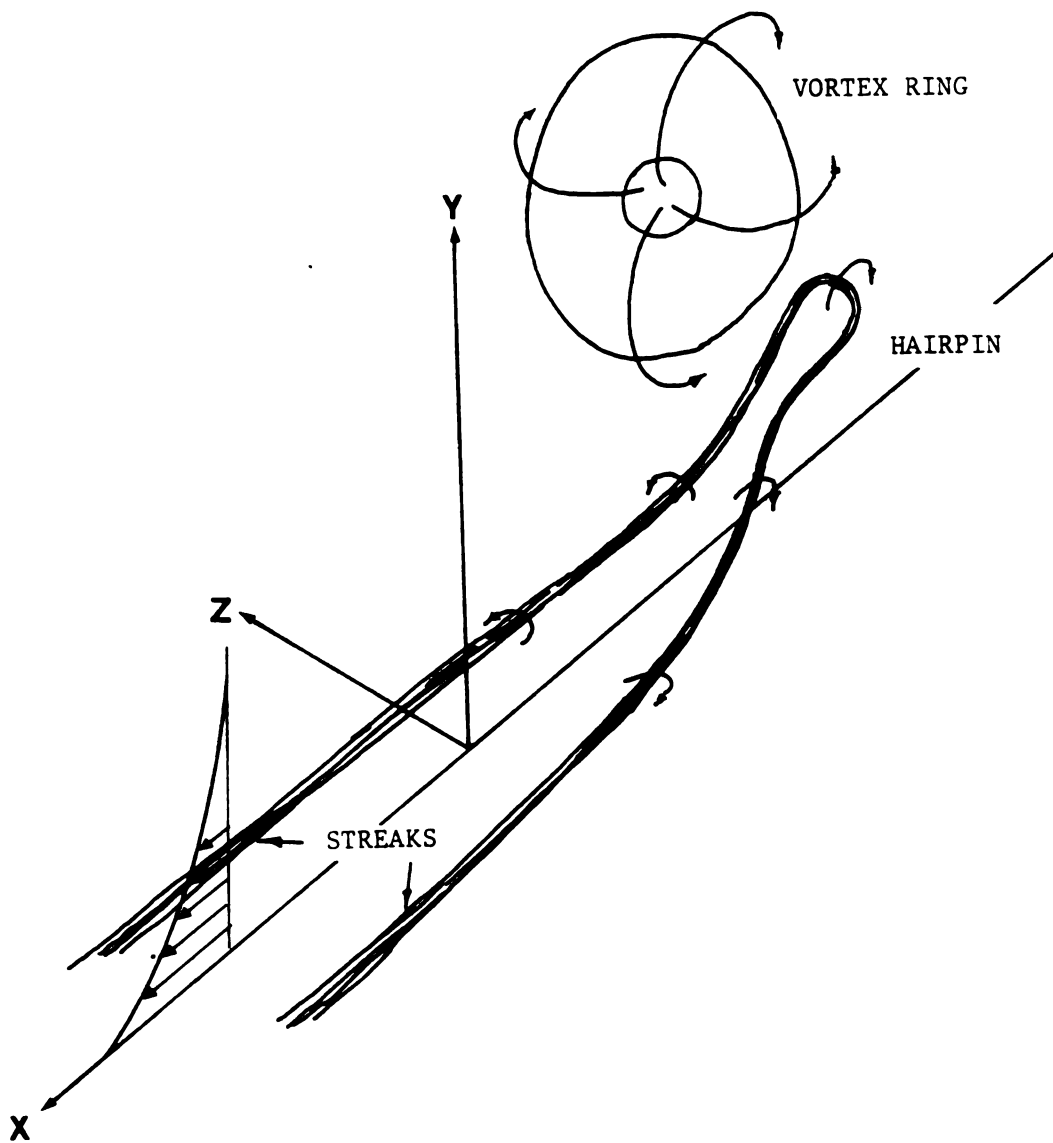
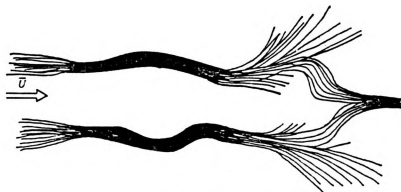
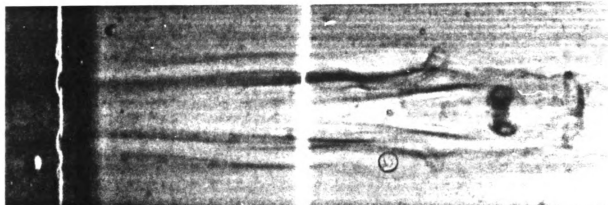


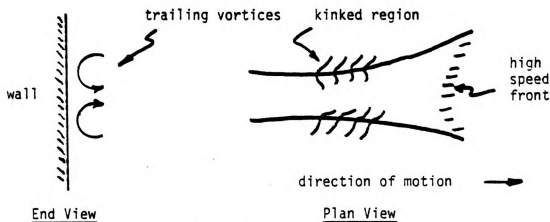
Fig. 4.24 The conceptual picture summarizing the spatial evolution of the vortex ring/moving wall interaction for $U_r/U_w > 0.6$ when the vortex ring moves away from the wall.



a. Offen & Kline (1975)



b. Chu (1987)



c. Smith (1978)

Fig. 4.25 Comparison among several investigators' observations.

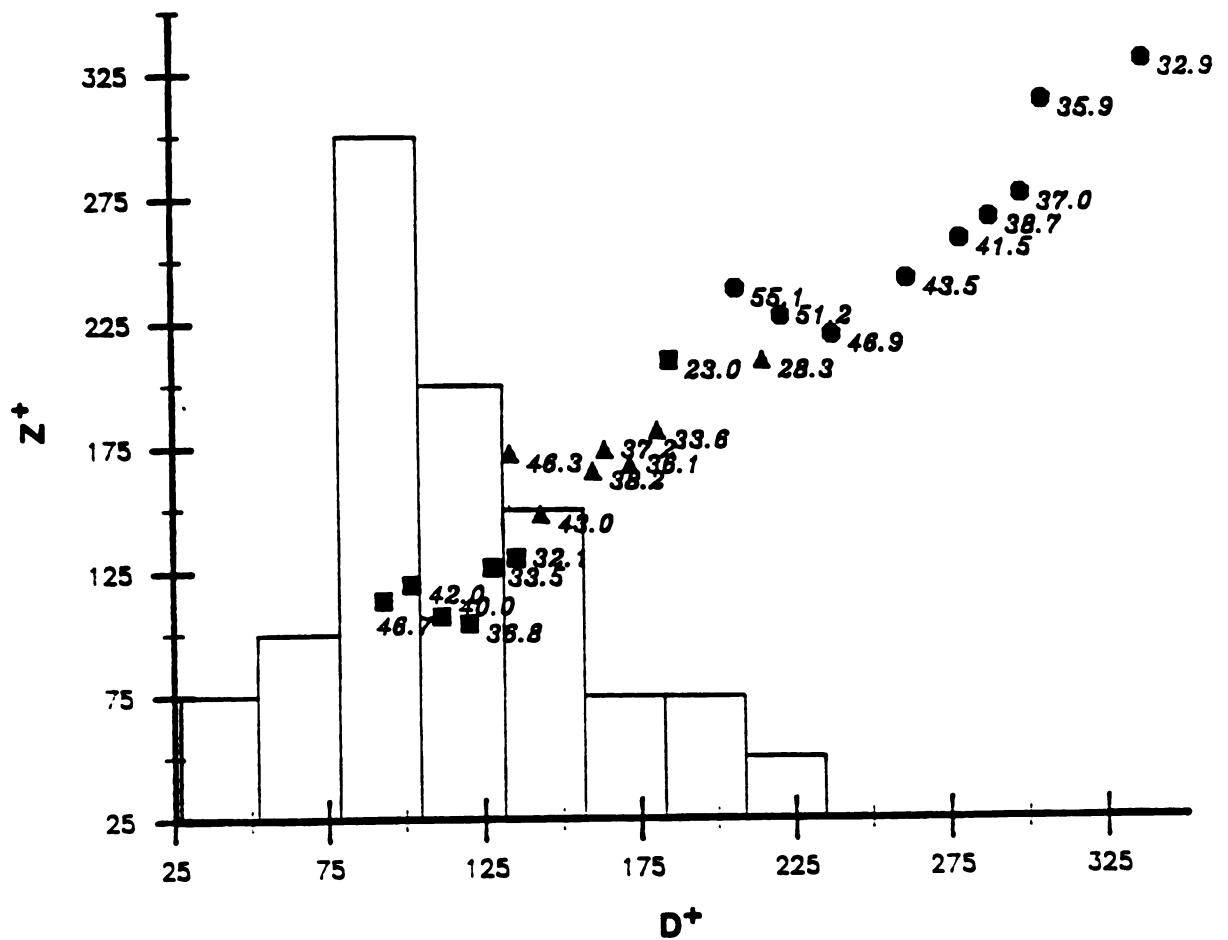


Fig. 4.26 The distribution of D^+ obtained from the diameter of the typical eddies of a turbulent boundary layer at $R_\theta = 1176$, superimposed upon the streak spacing obtained for various size rings.

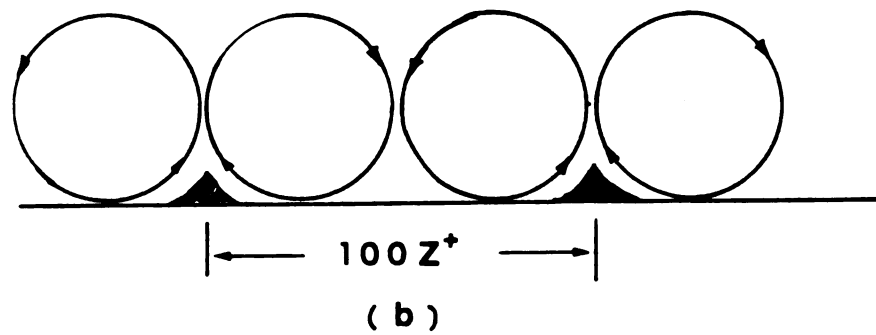
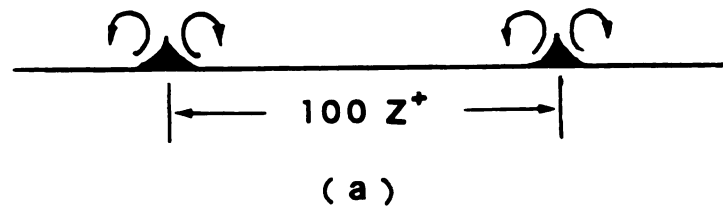


Fig. 4.27 (a) The vortical motions associated with the observed streaky structure in vortex ring/moving wall simulation; (b) The counter-rotating pair hypothesized by many investigators.

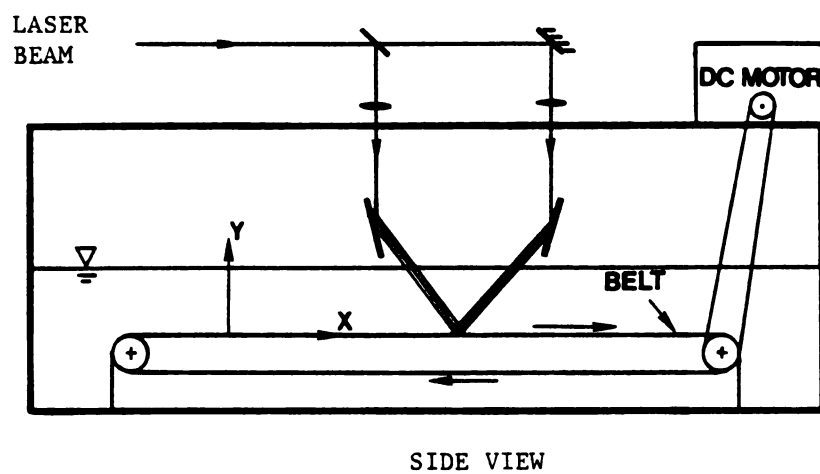


Fig. 5.1 A schematic of experimental apparatus of the Stokes' layer measurement; the moving belt system is similar to what was used in water tank.

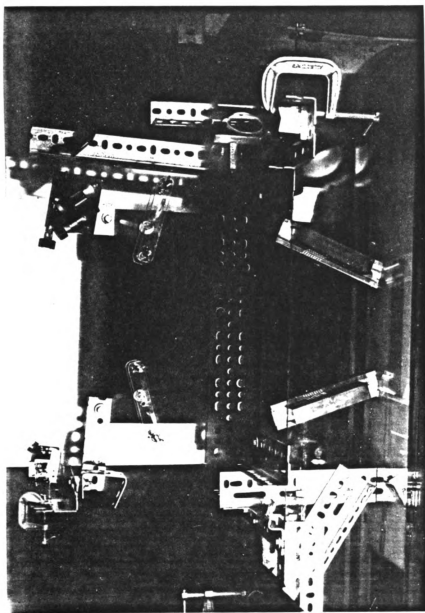


Fig. 5.2 The optical configuration for generating the photochromic grid.

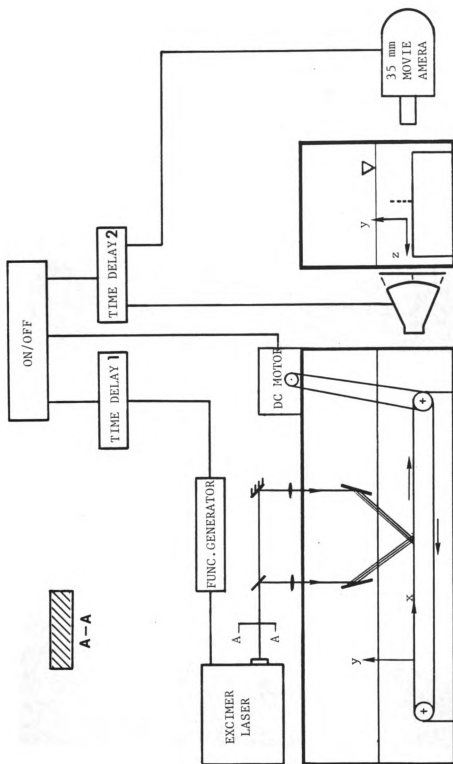


Fig. 5.3 The flow chart of the control system of the Stokes' layer measurement. The best orientation of the incident laser beam is also shown in this figure.

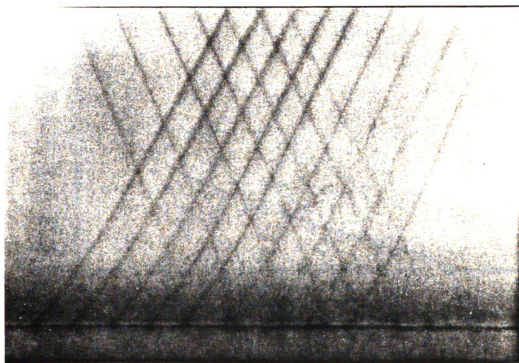
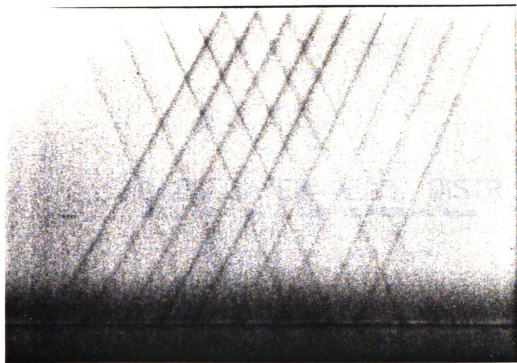


Fig. 5.4 Two photos from the result which are 0.05 second apart; these photos were taken for $U_w = 12.7$ cm/sec and belt running time $t = 5.25$ seconds; the belt moved from right to left.

STOKES' LAYER VELO. DISTR.

U0 : •, .. 0.417 fps; +.. 0.494 fps. t=5.25 sec. layusp

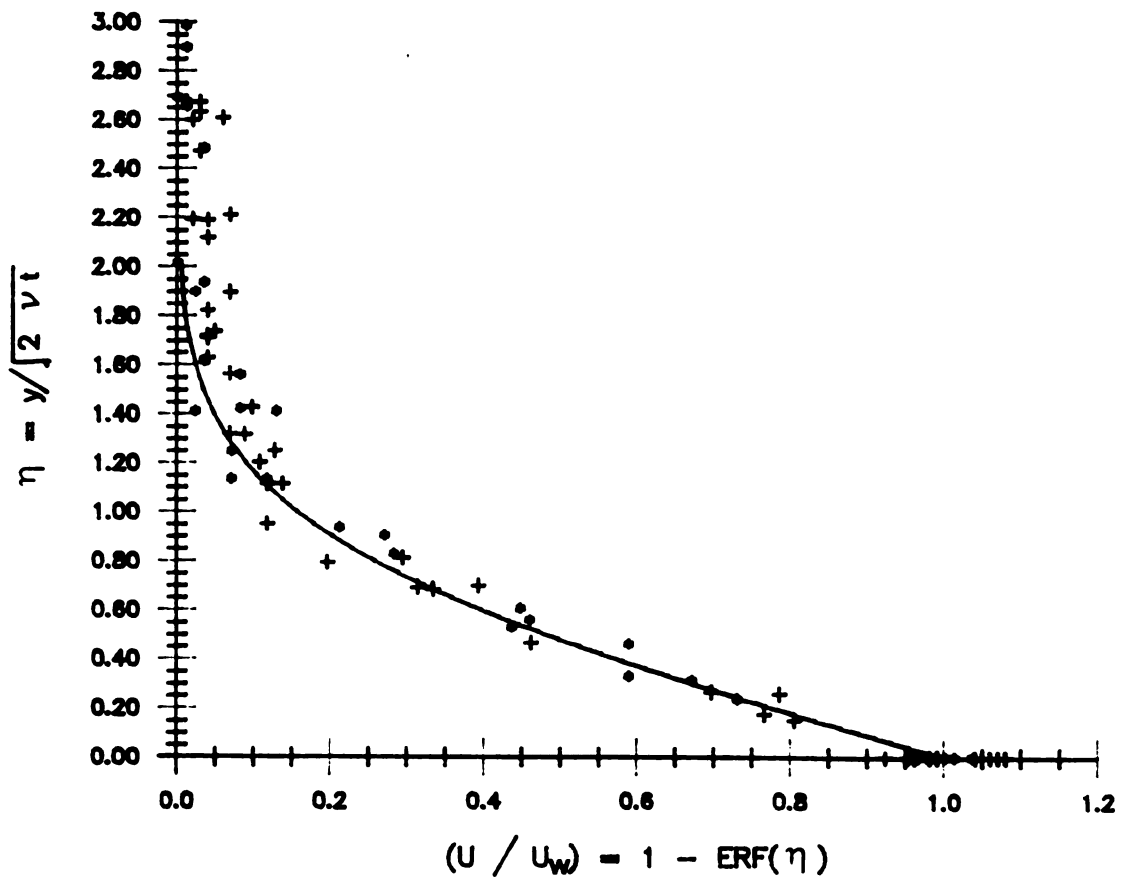


Fig. 5.5 The nondimensionalized velocity profile for two belt running speeds where the solid line represents the exact solution.

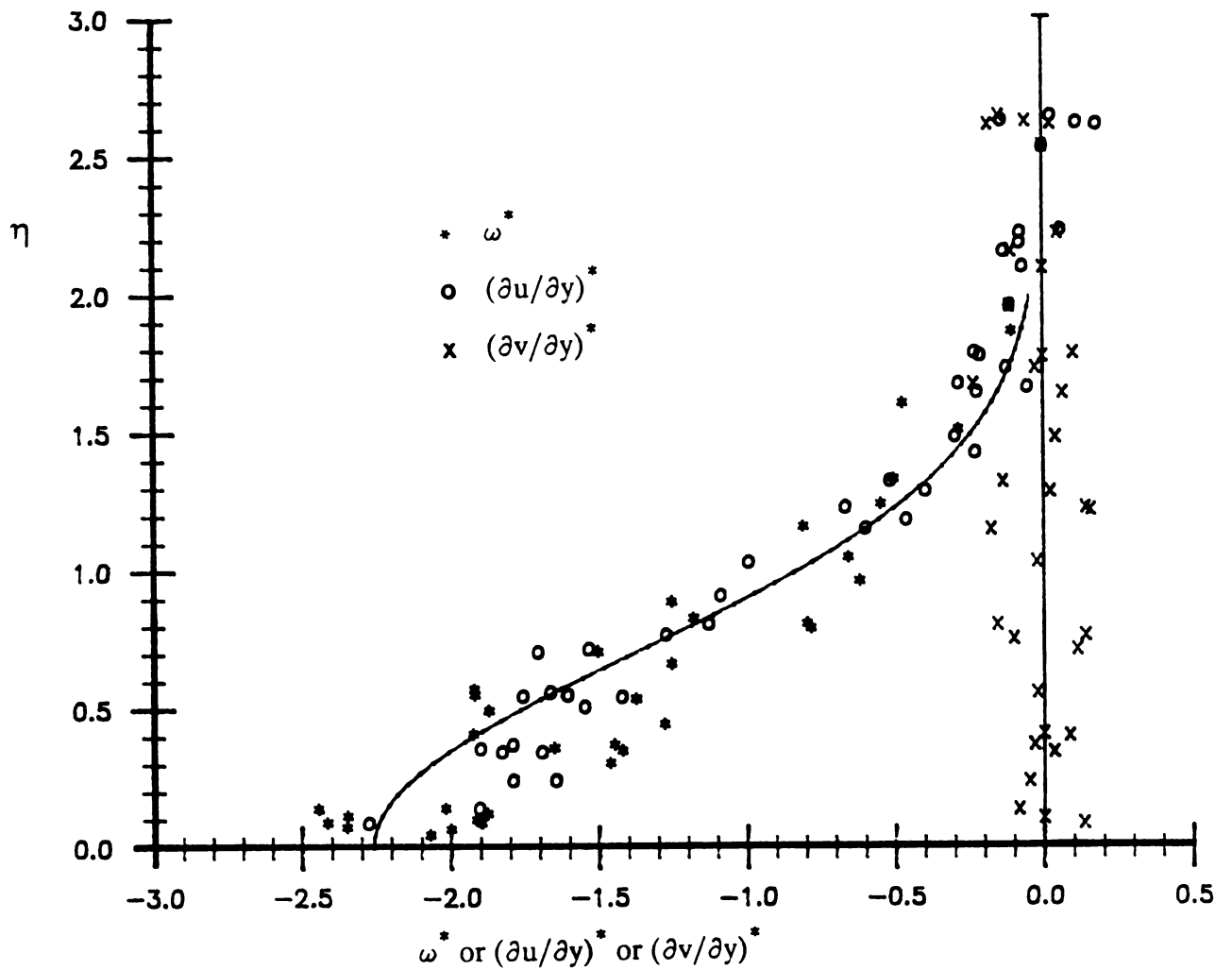


Fig. 5.6 Results of the velocity gradient $\partial u / \partial y$ obtained from double differentiation and of the spanwise vorticity obtained from circulation approach are shown in this figure where they are compared with the exact solution (represented by solid line). Everything is nondimensionalized by the similarity variables of the exact solution. A check of continuity equation is also shown in this figure.

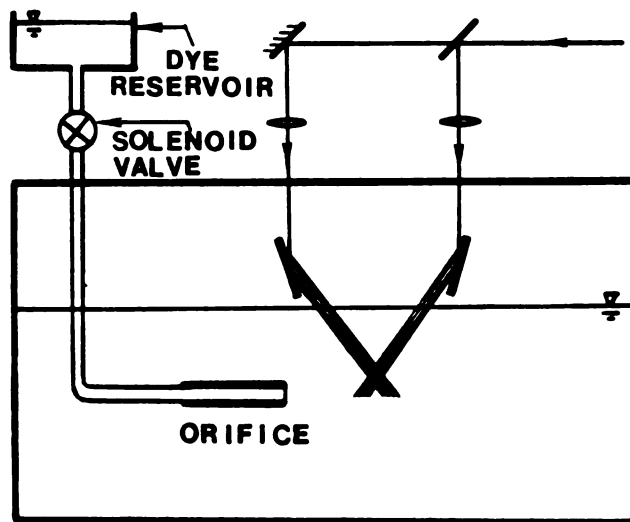


Fig. 5.7 A schematic of the experimental configuration used to generate and measure the vortex ring.

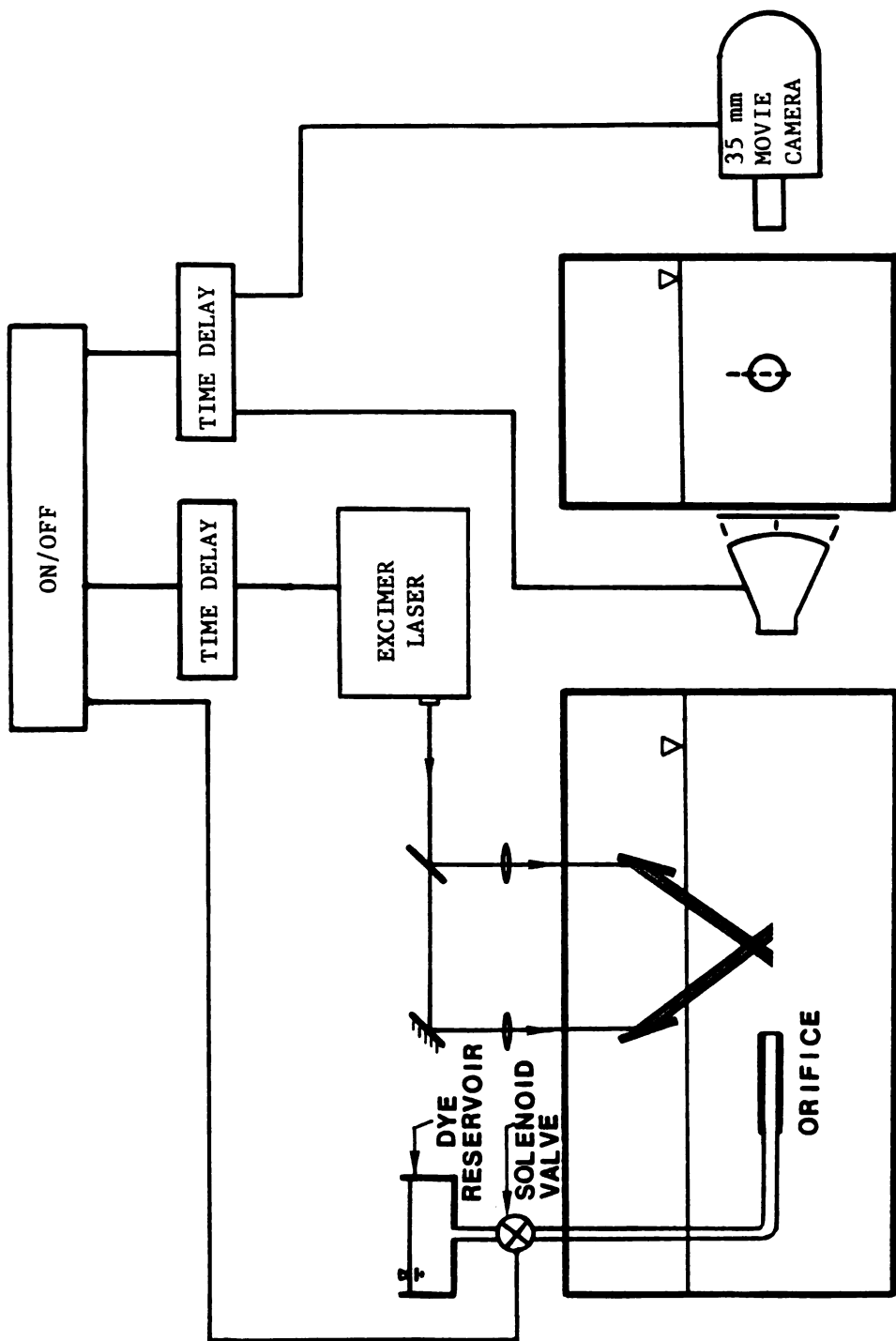


Fig. 5.8 The flow chart of the control system for vortex ring measurement.

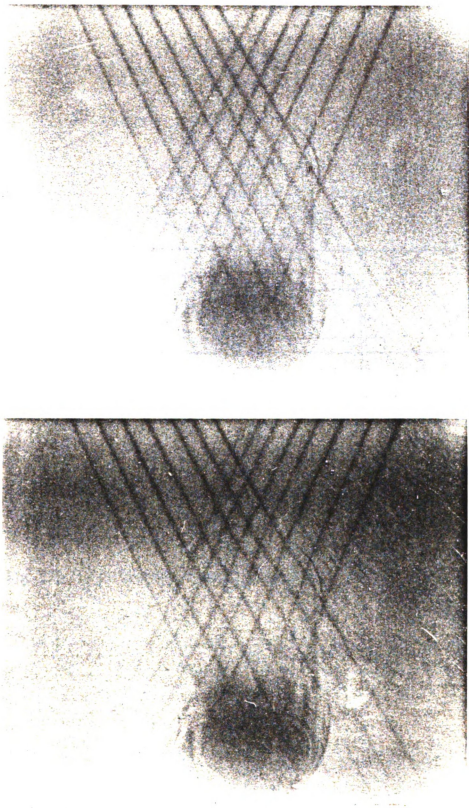


Fig. 5.9 Two photos of the result which are 0.07 second apart

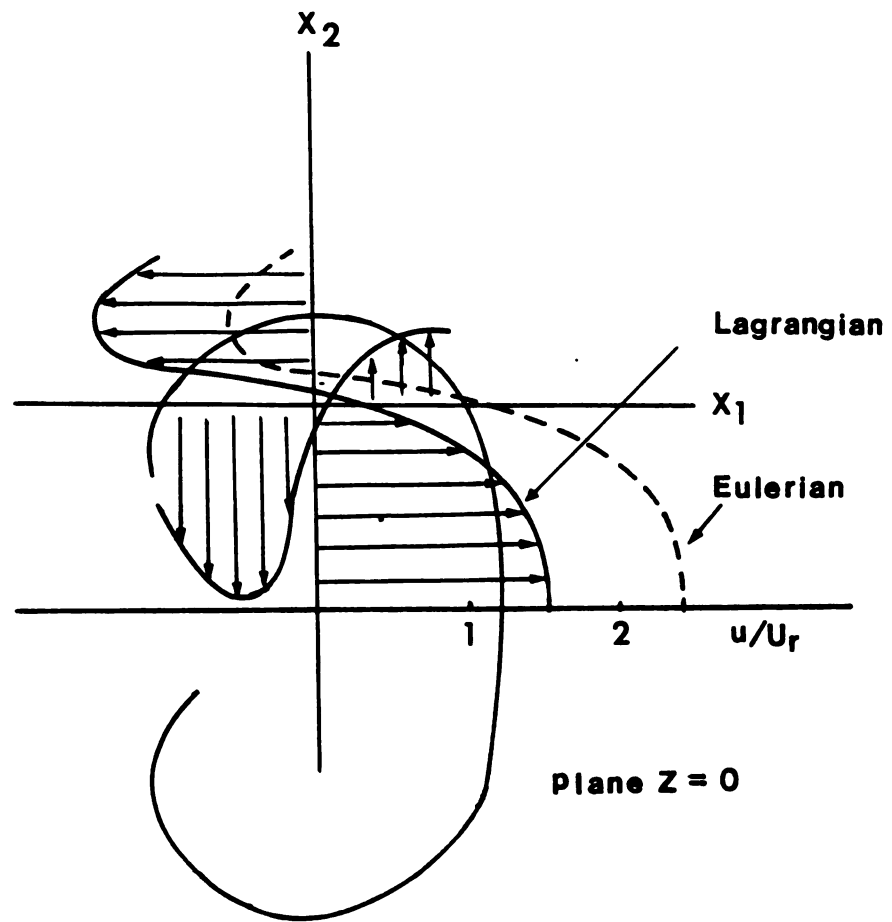


Fig. 5.10 The instantaneous velocities distribution along two axes of the ring.

CIRCULATION DISTRIBUTION

●..Current measurement, □.. Hill's, △▽..Sullivan et al.

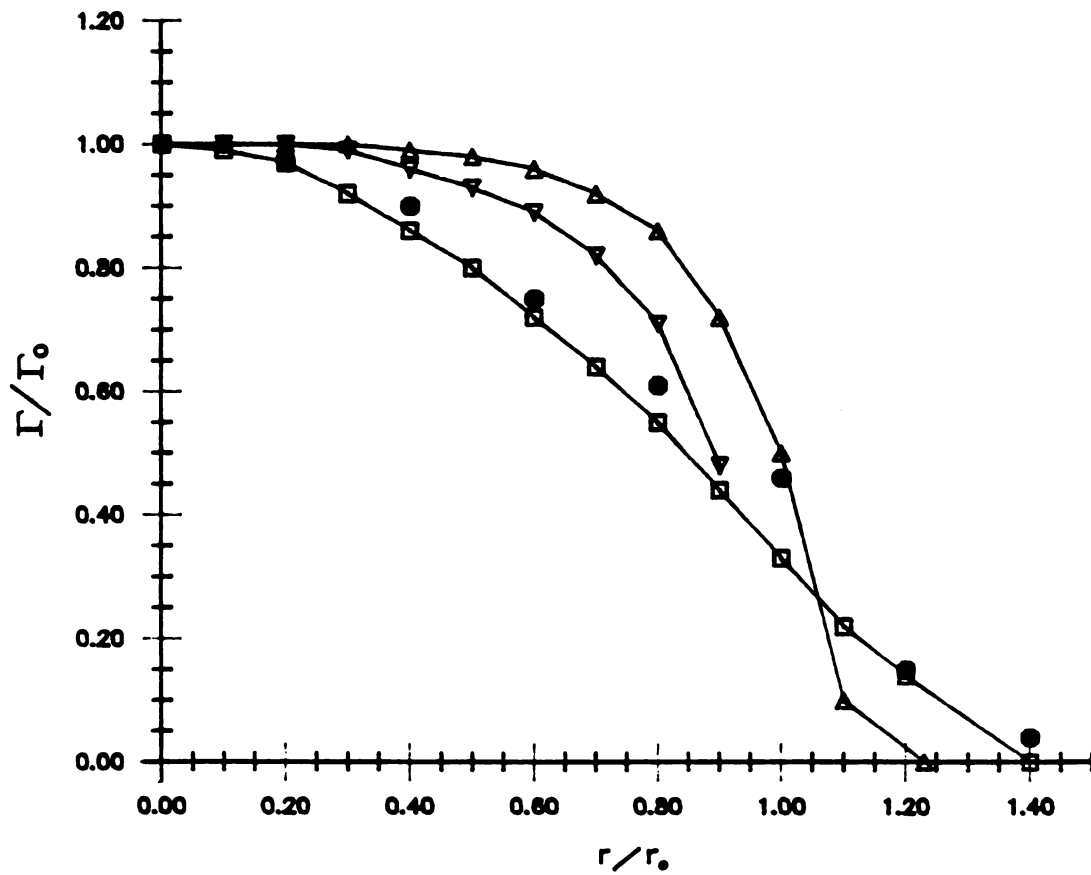


Fig. 5.11 The instantaneous circulation distribution of the ring, which also shows the results obtained by Sullivan et al. (1973) for different Reynolds numbers and shows Hill's exact solution of a spherical vortex.

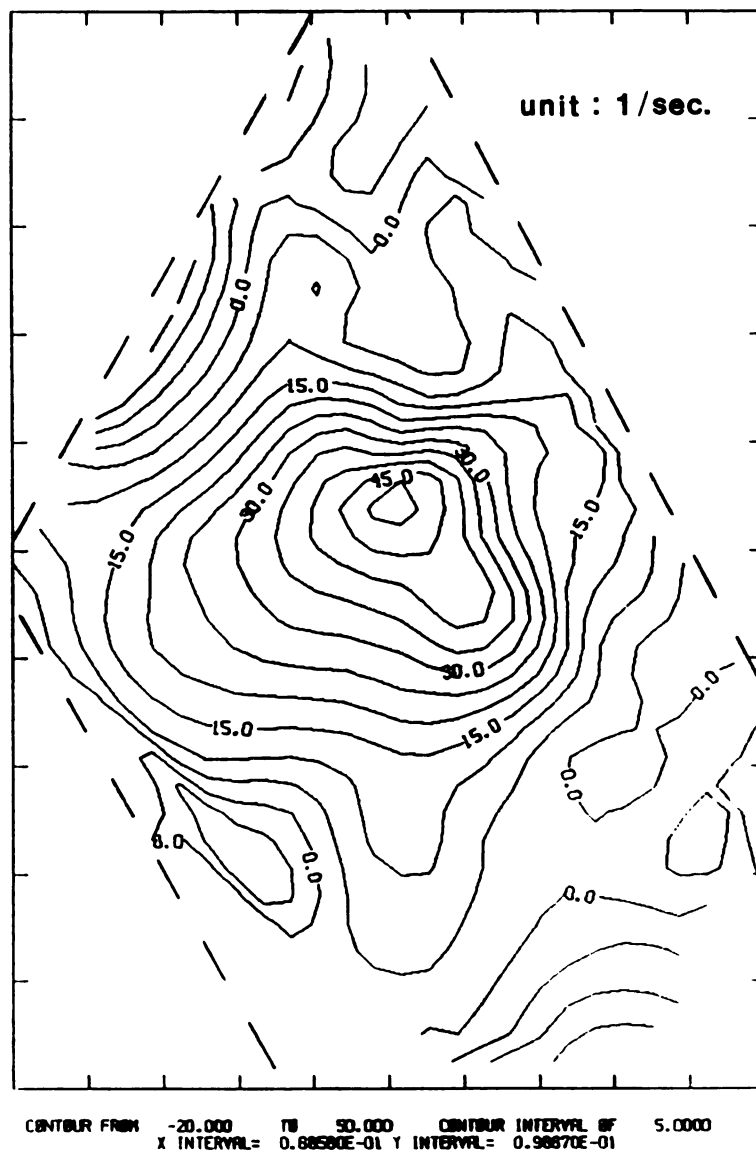


Fig. 5.12 The instantaneous vorticity distribution over a vortex ring.

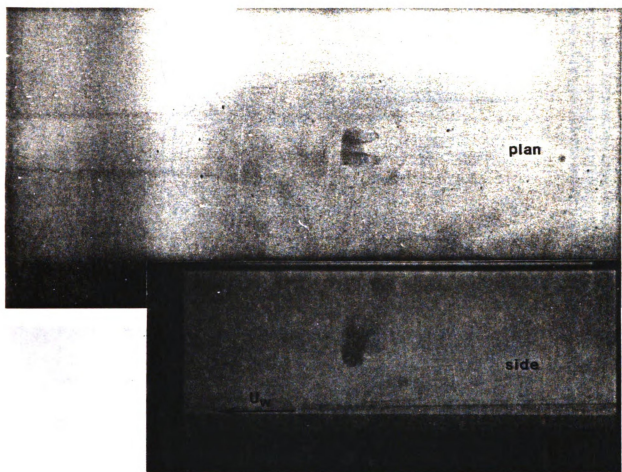


Fig. 5.13 Four sets of photos with both top view and side view describing the time evolution of vortex ring/moving wall interactions in the conditions of $U_r/U_w = 0.26$, 3 degree of incident angle, $\delta/D = 0.18$ and $U_w = 15.5$ cm/sec.

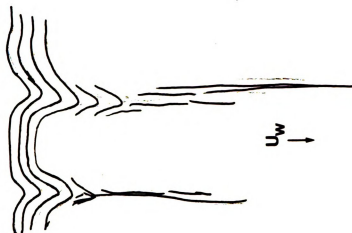
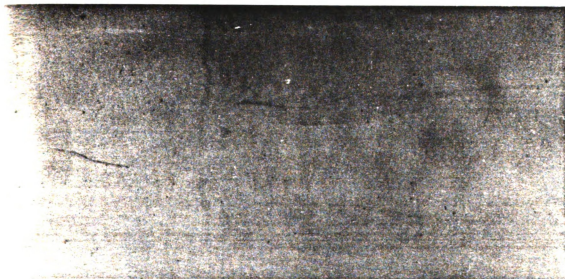


Fig. 5.14 By sending a single photochromic tracer parallel to the moving wall at $y+ \approx 16$ we obtained the visual result of the interaction shown in this figure, which is the same as that obtained from the hydrogen bubble technique by many other researchers, such as Kim et al.(1971) and Smith et al.(1983).

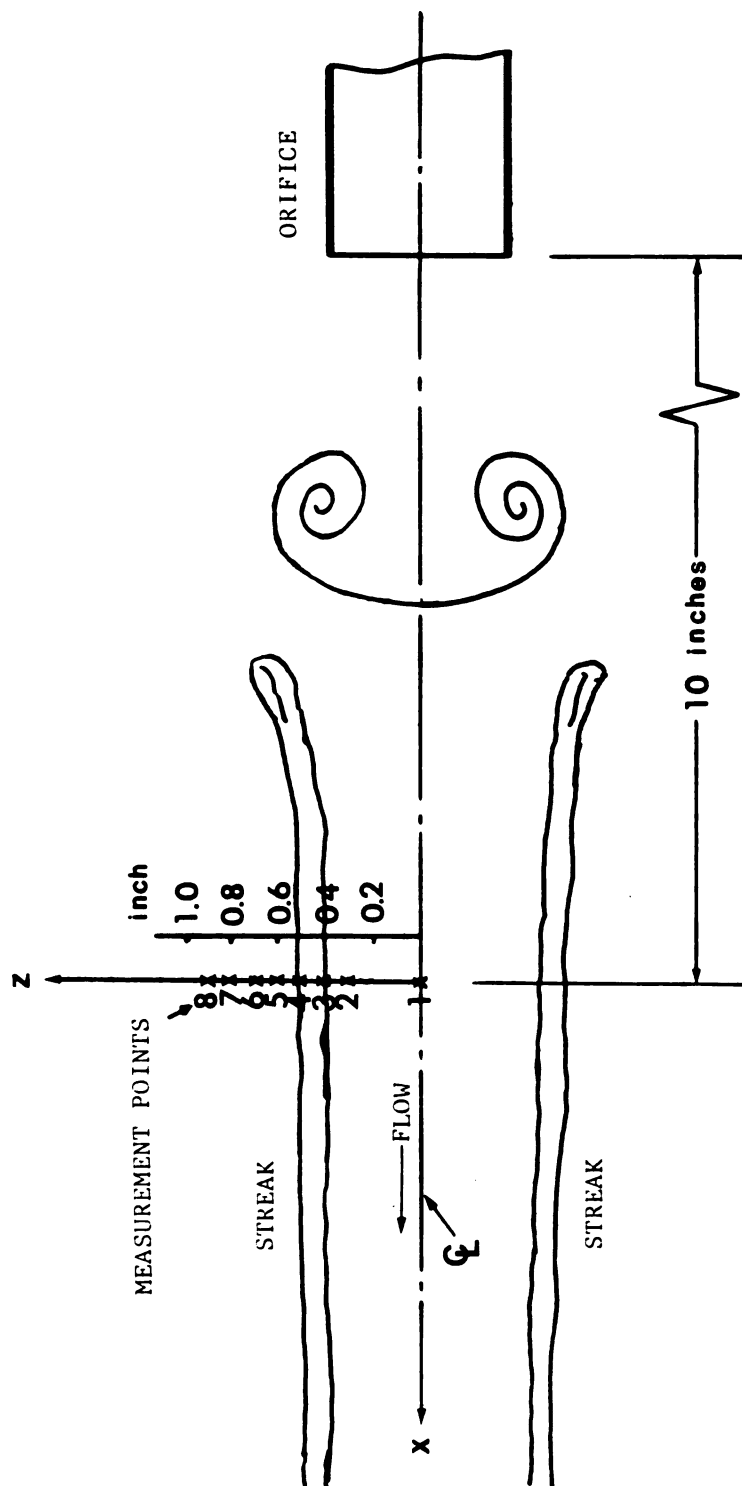


Fig. 5.15 The locations of velocity measurement.

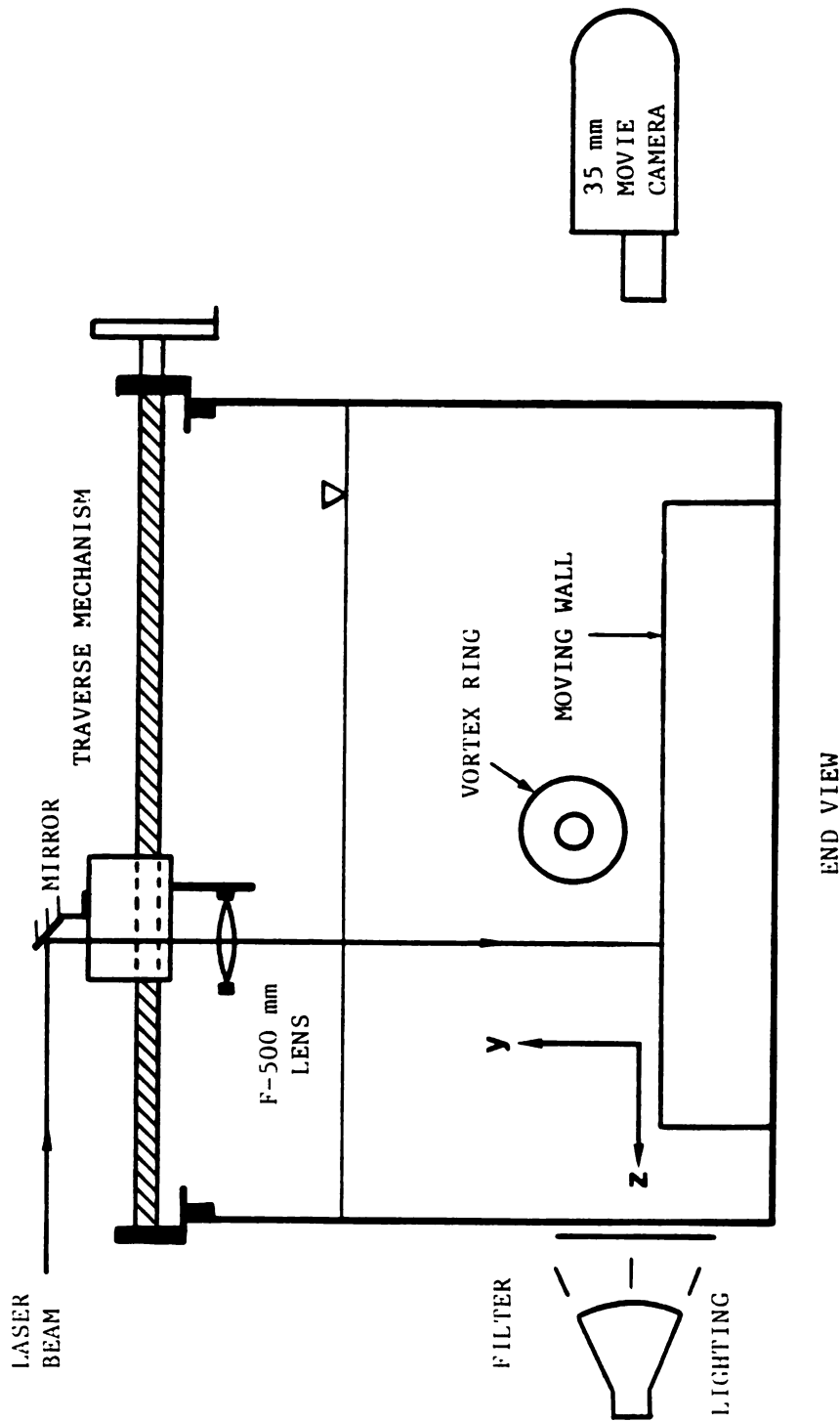
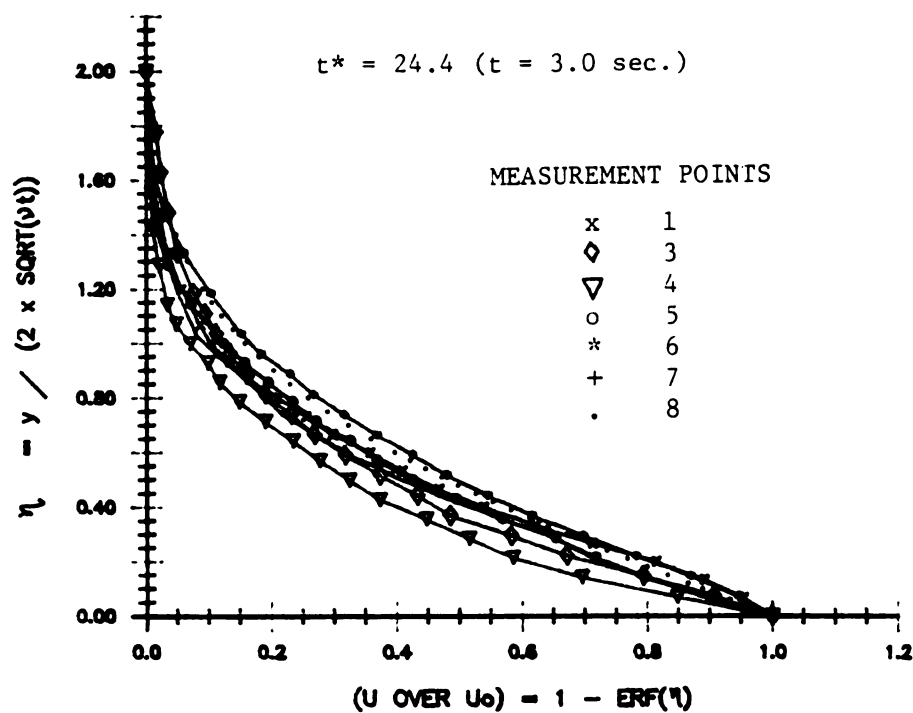


Fig. 5.16 The details of the optical configuration.

A



B

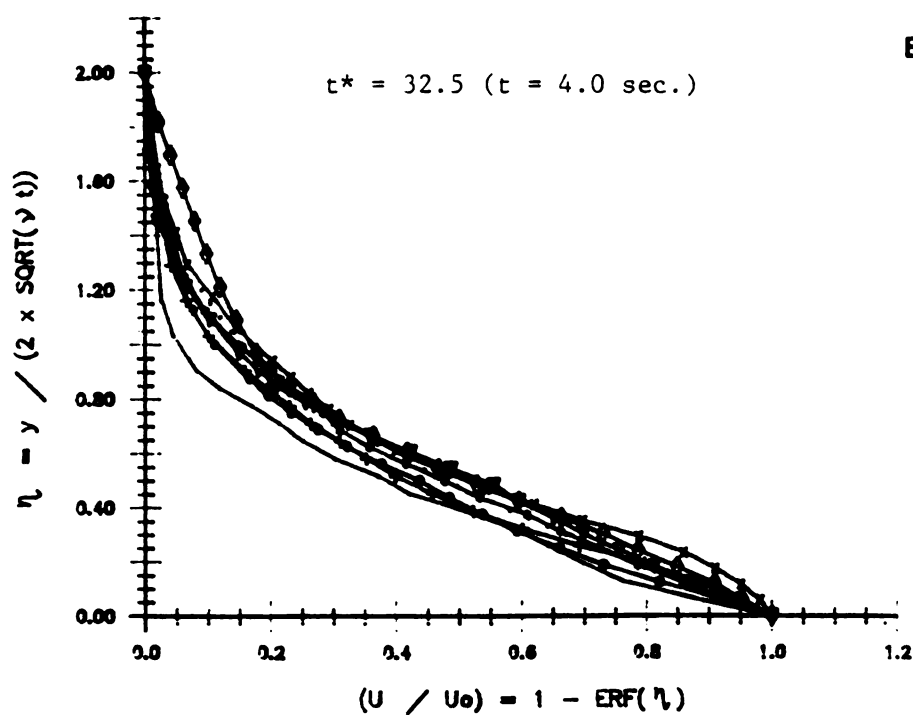


Fig. 5.17 The time evolution of the streamwise velocity distribution at the measurement points. The dotted lines represent the undisturbed velocity profiles of the Stokes' layer.

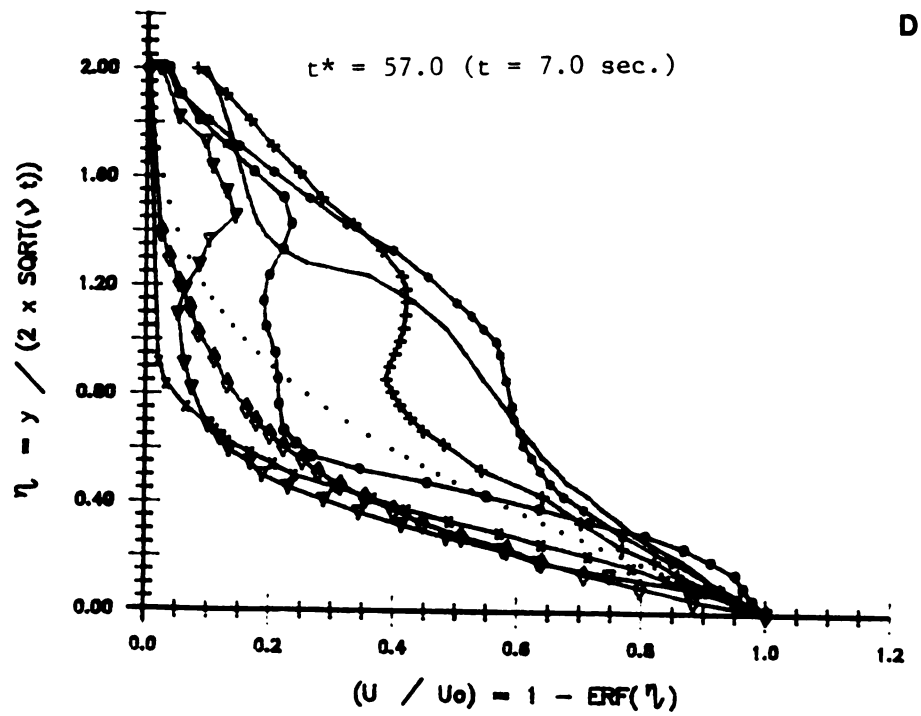
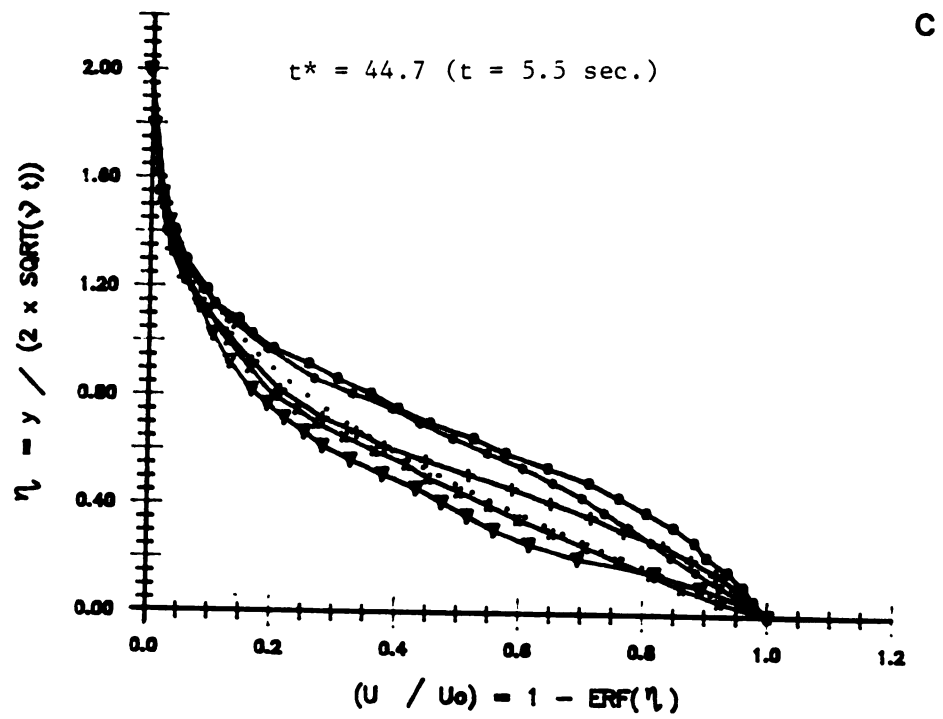
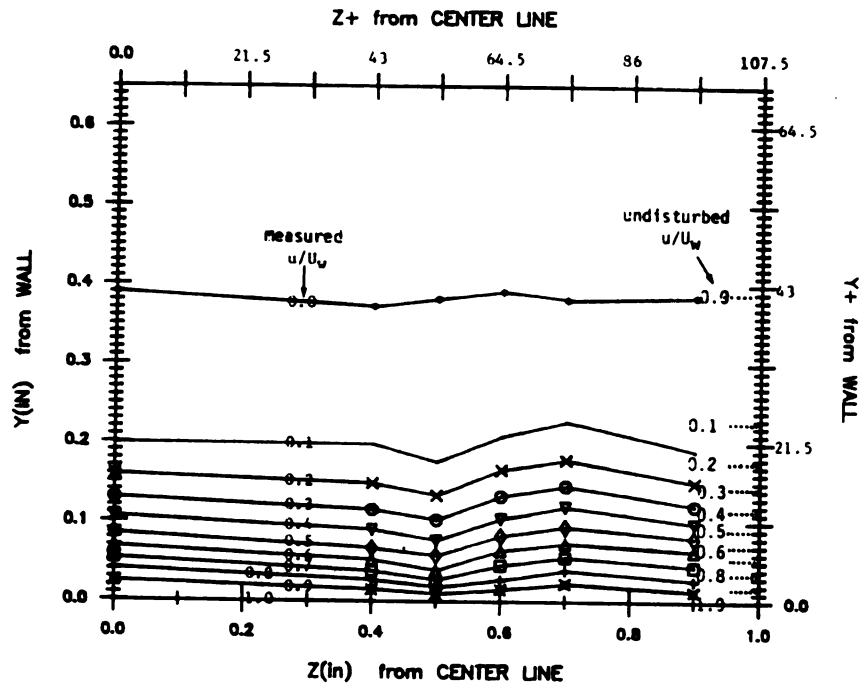


Fig. 5.17 Cont.

CONST. u , at $t^* = 24.4$ (3.0 sec)



CONST. u , at $t^* = 32.5$ (4.0 sec)

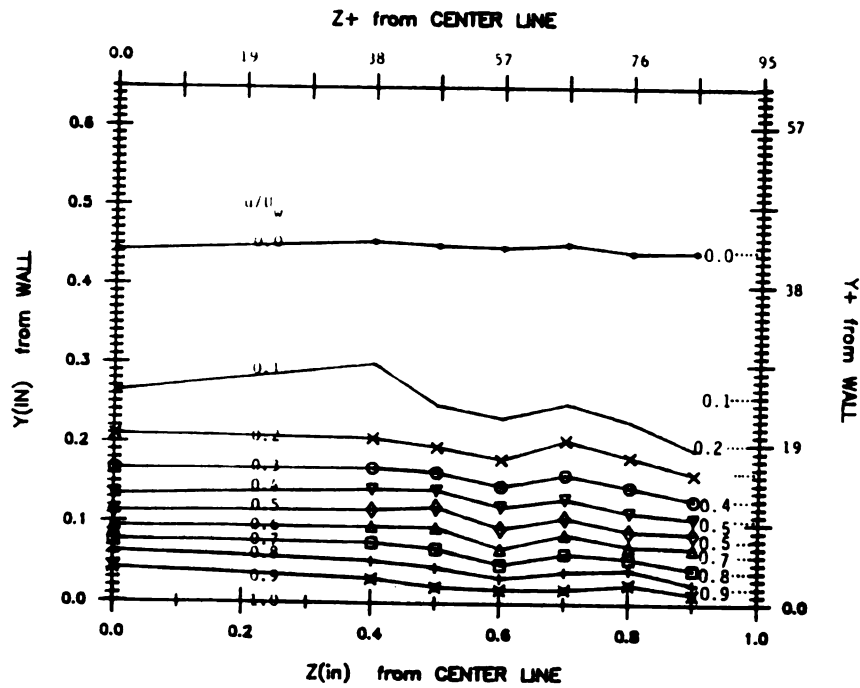
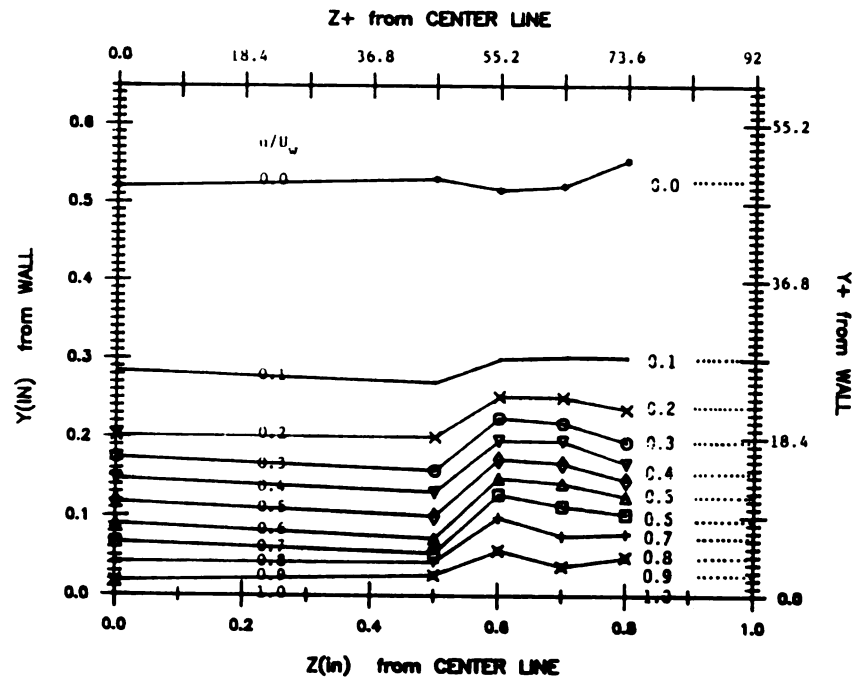


Fig. 5.18 The constant velocity lines in y - z plane.

CONST. u , at $t^* = 44.7$ (5.5 sec)



CONST. u , at $t^* = 57.0$ (7.0 sec)

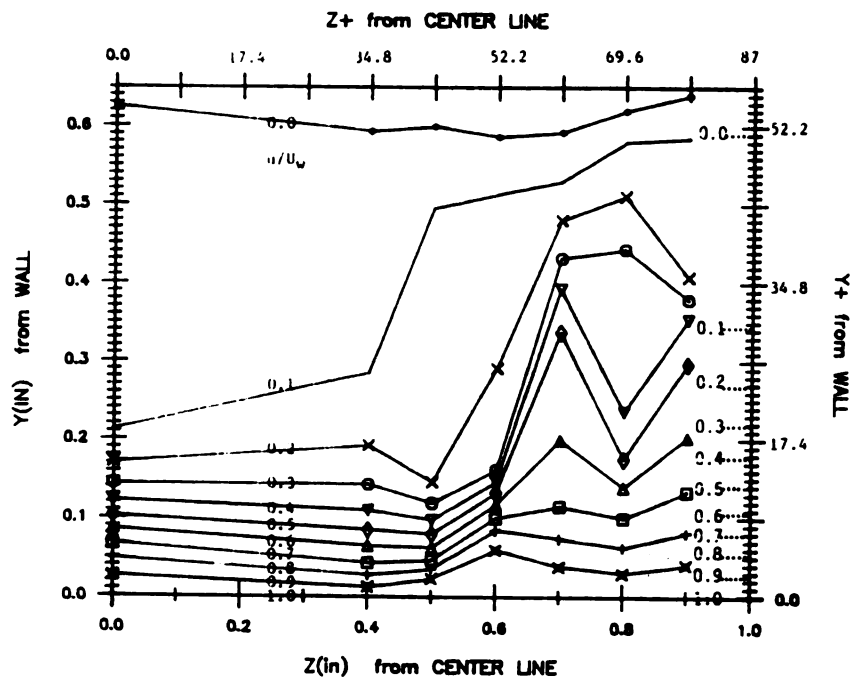


Fig. 5.18 Cont.

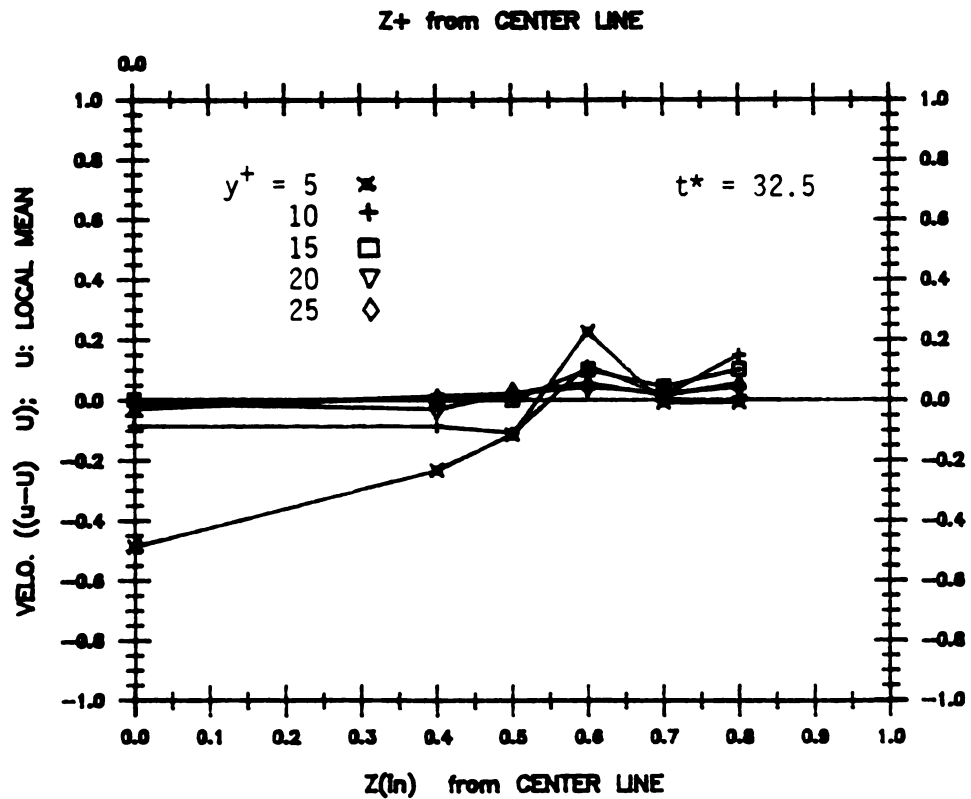
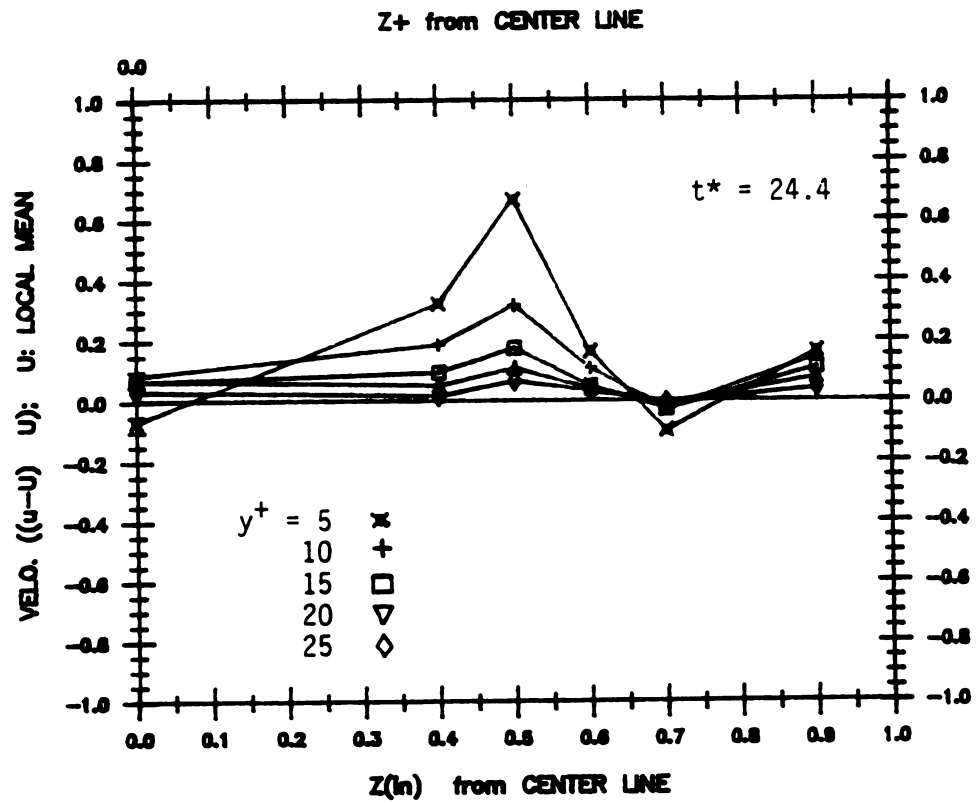


Fig. 5.19 The velocity defect or gain with respect to the undisturbed wall layer shown in (a). These sets of data had been converted to the turbulent boundary layer point of view by performing the Galilean transformation.

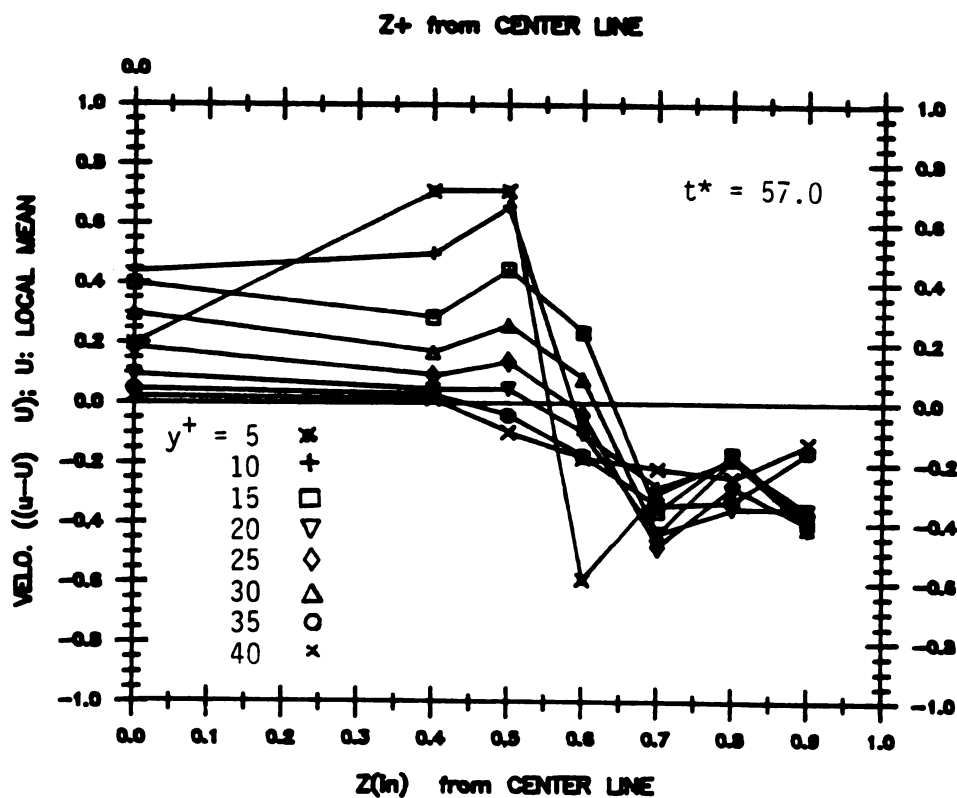
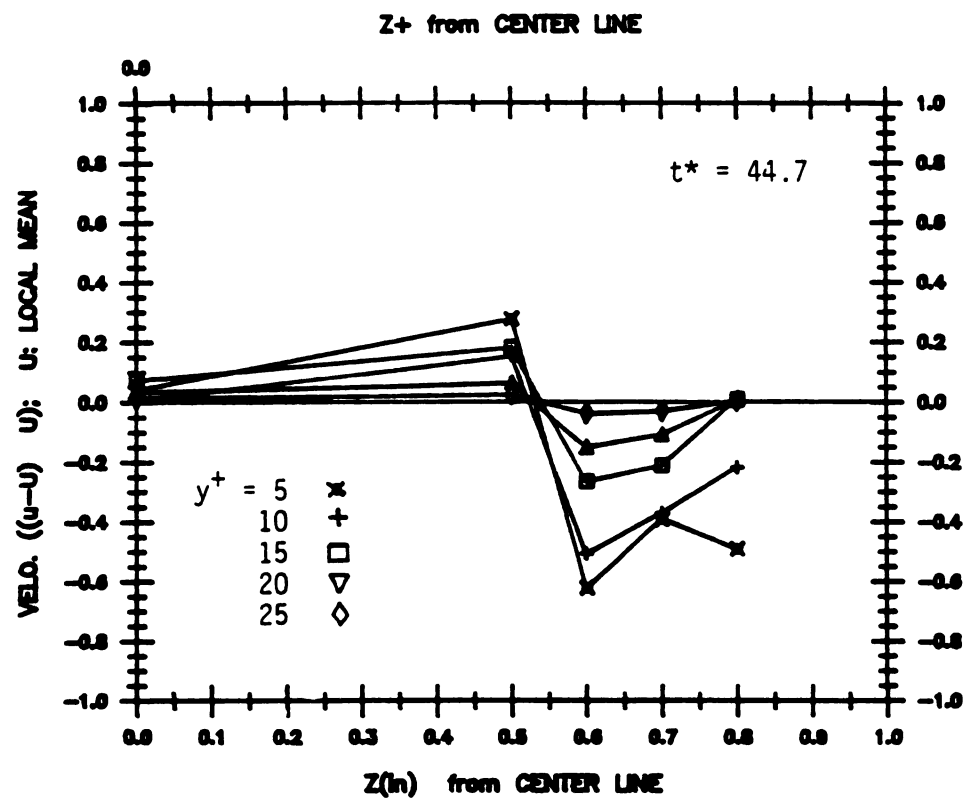


Fig. 5.19 Cont.

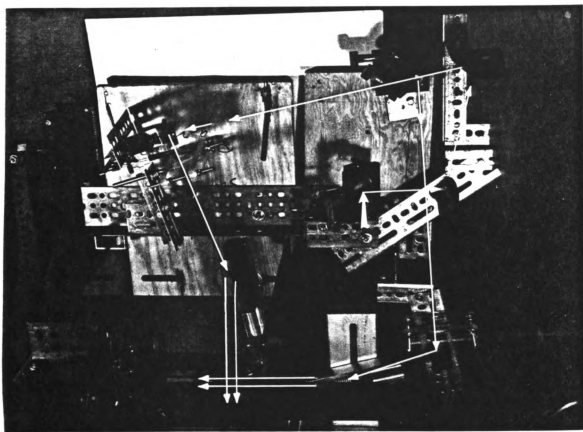


Fig. 5.20 A photo of the optical configuration and the orientation of the laser beam.

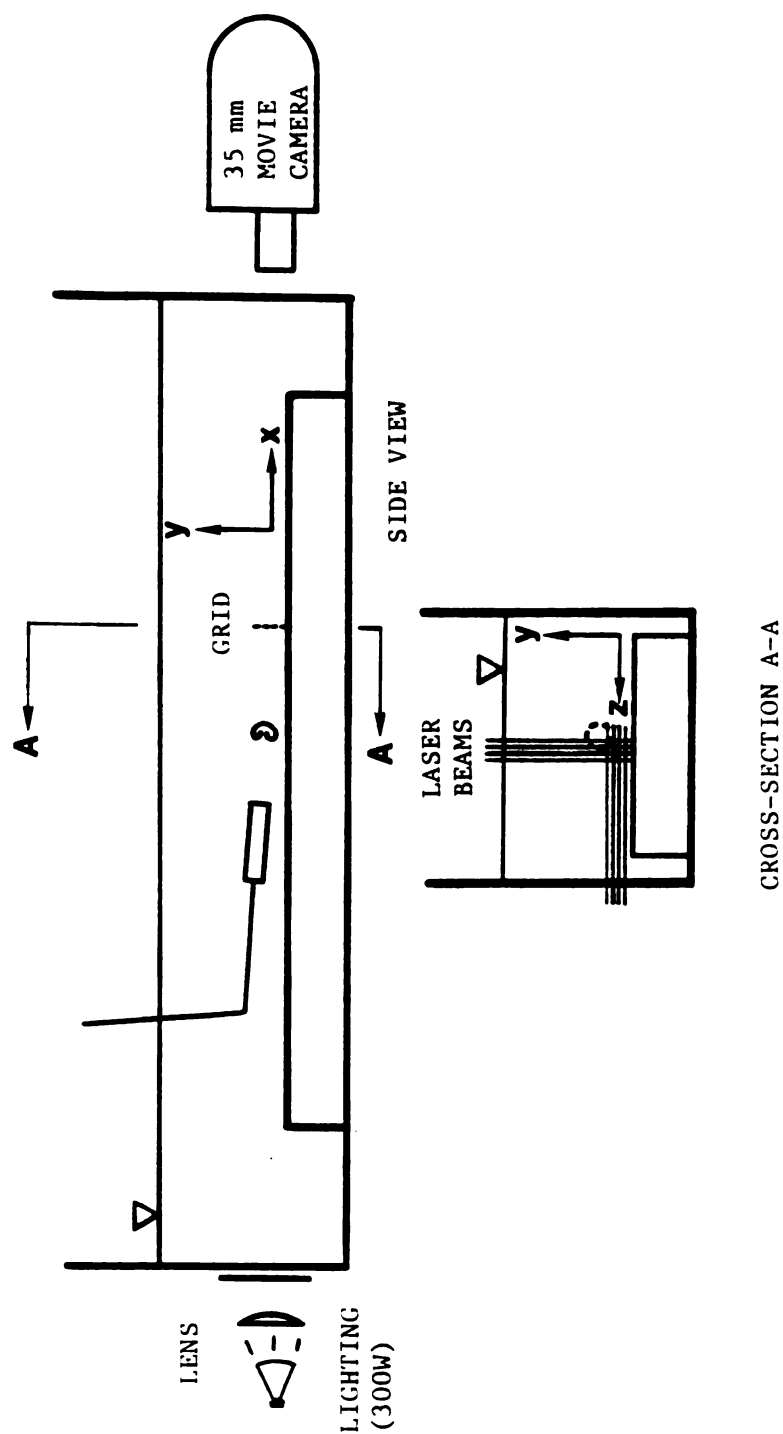


Fig. 5.21 The side view of the data acquisition and lighting system.

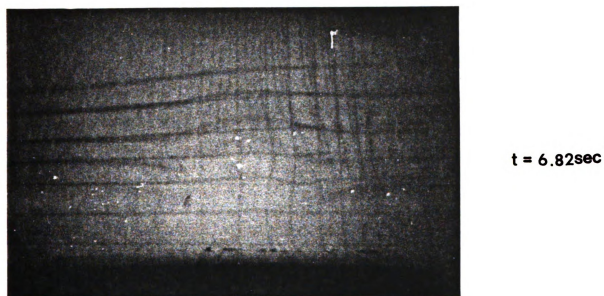
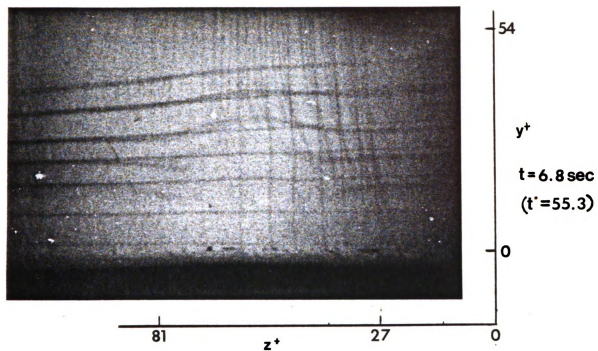


Fig. 5.22 The result of the streamwise vorticity measurement. Those photos are selected from the same sequence of movie in one experiment. Two photos of each set were 0.02 second apart which corresponded to $0.5t^+$ apart.

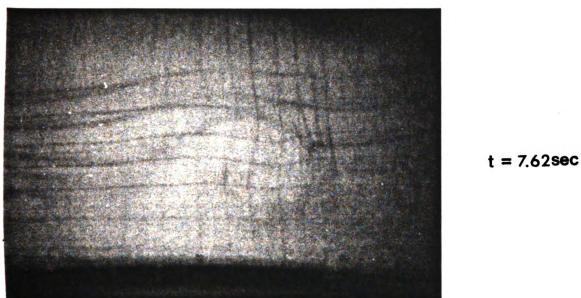
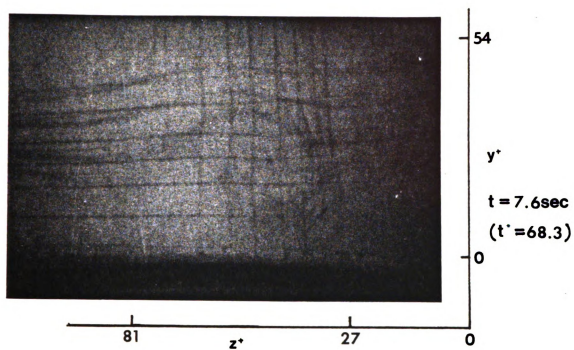


Fig. 5.22 Cont.

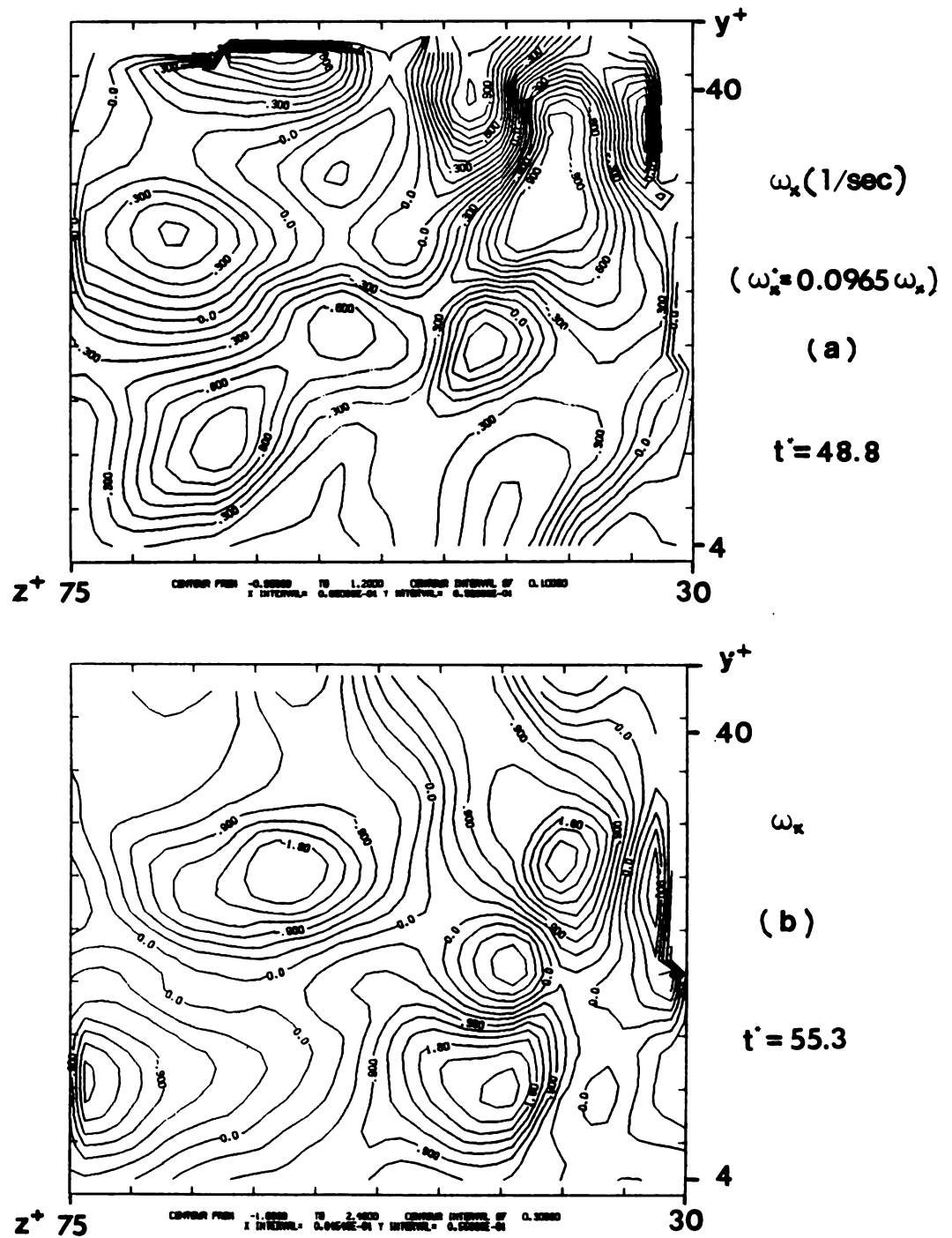


Fig. 5.23 The contour plots of the instantaneous streamwise vorticity distribution.

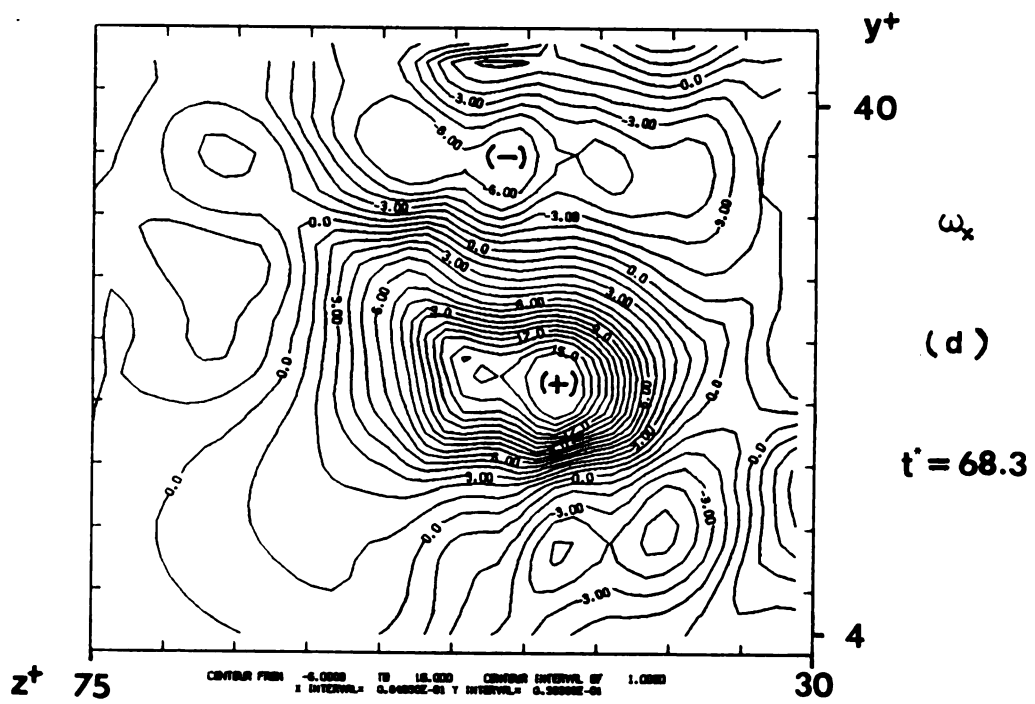
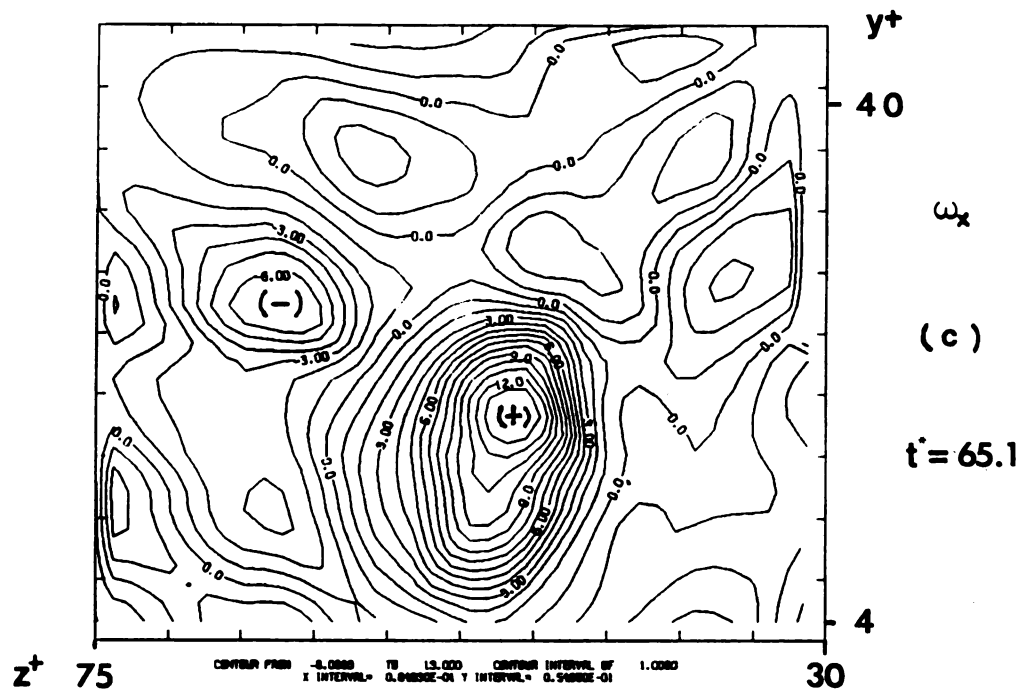


Fig. 5.23 Cont.

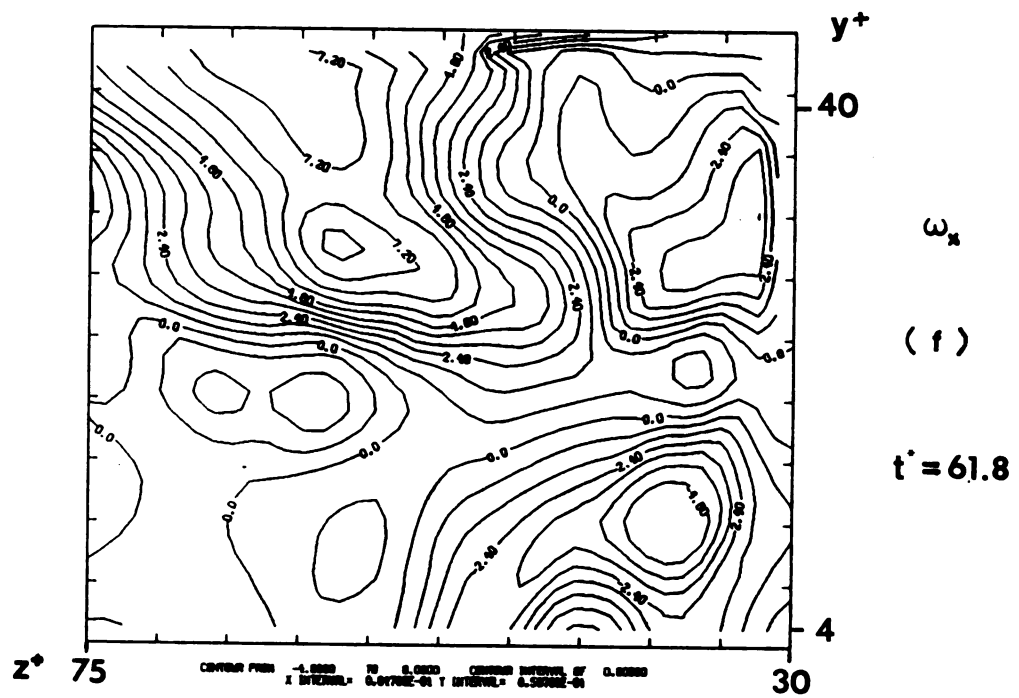
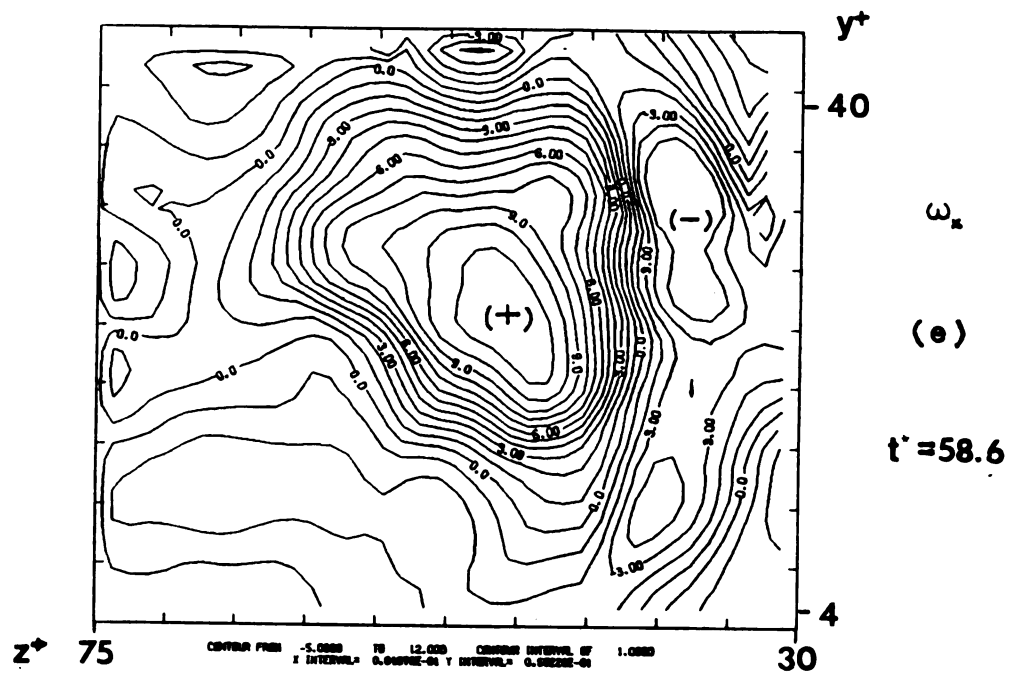


Fig. 5.23 Cont.

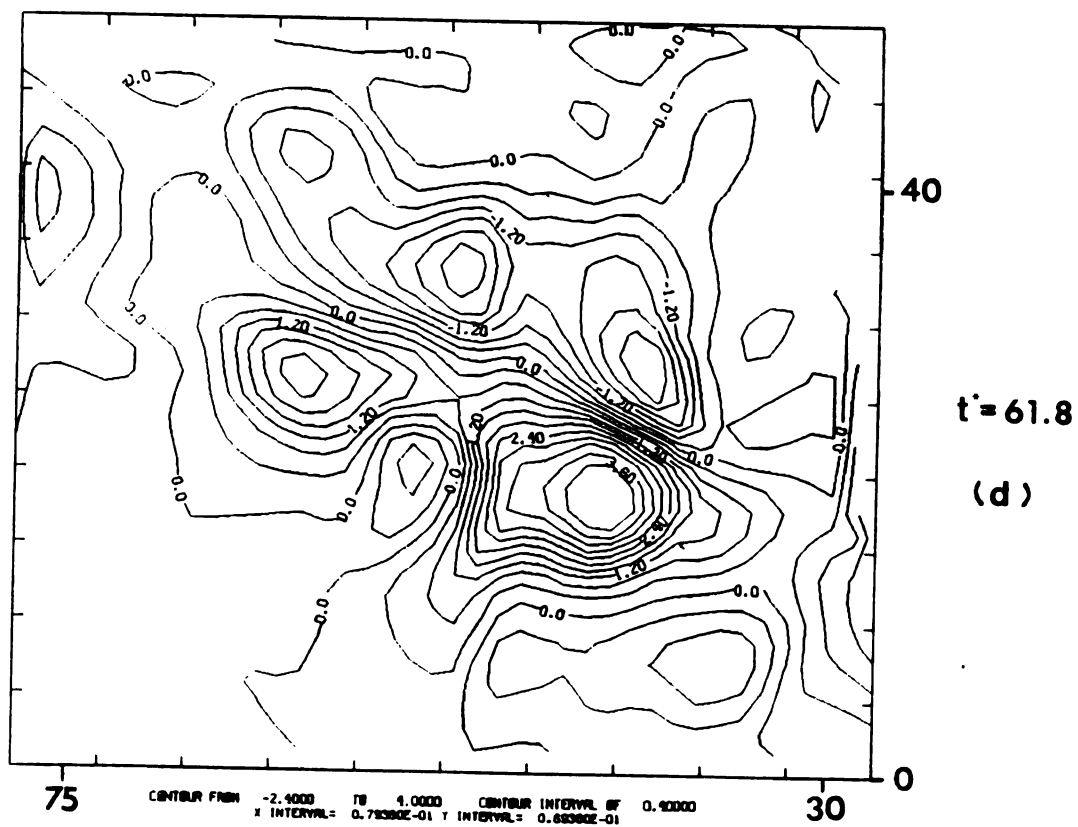
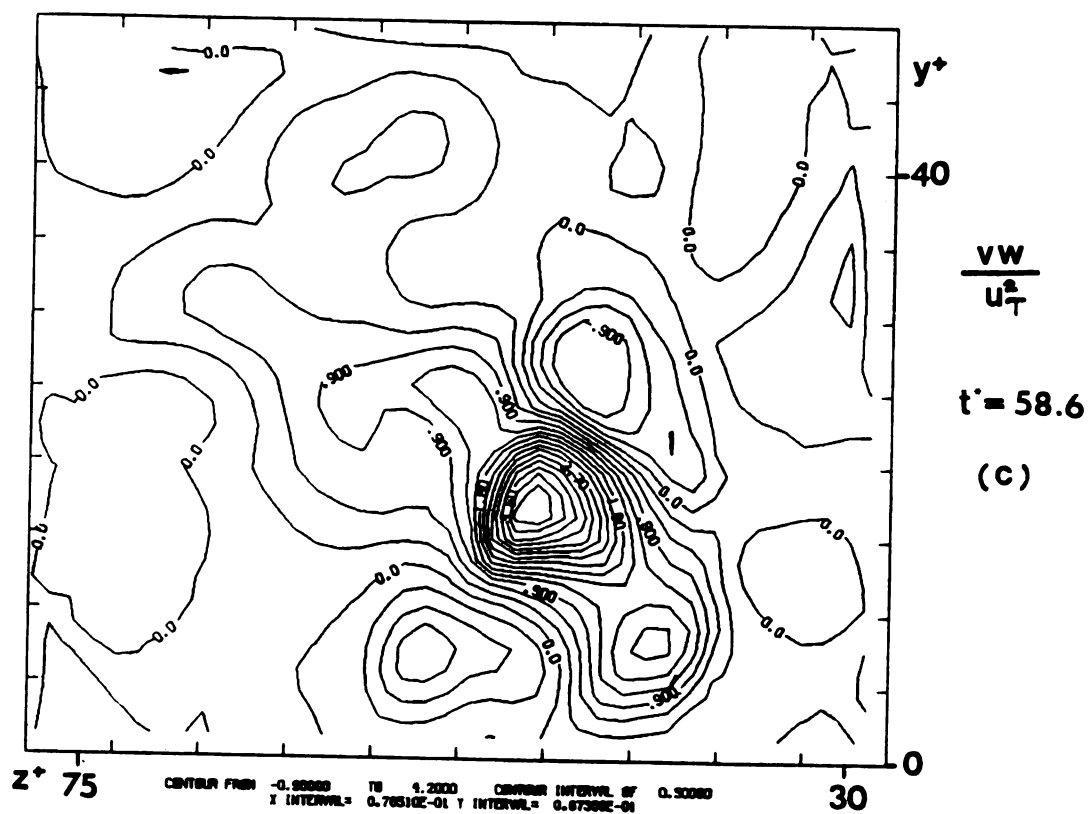


Fig. 5.24 Cont.

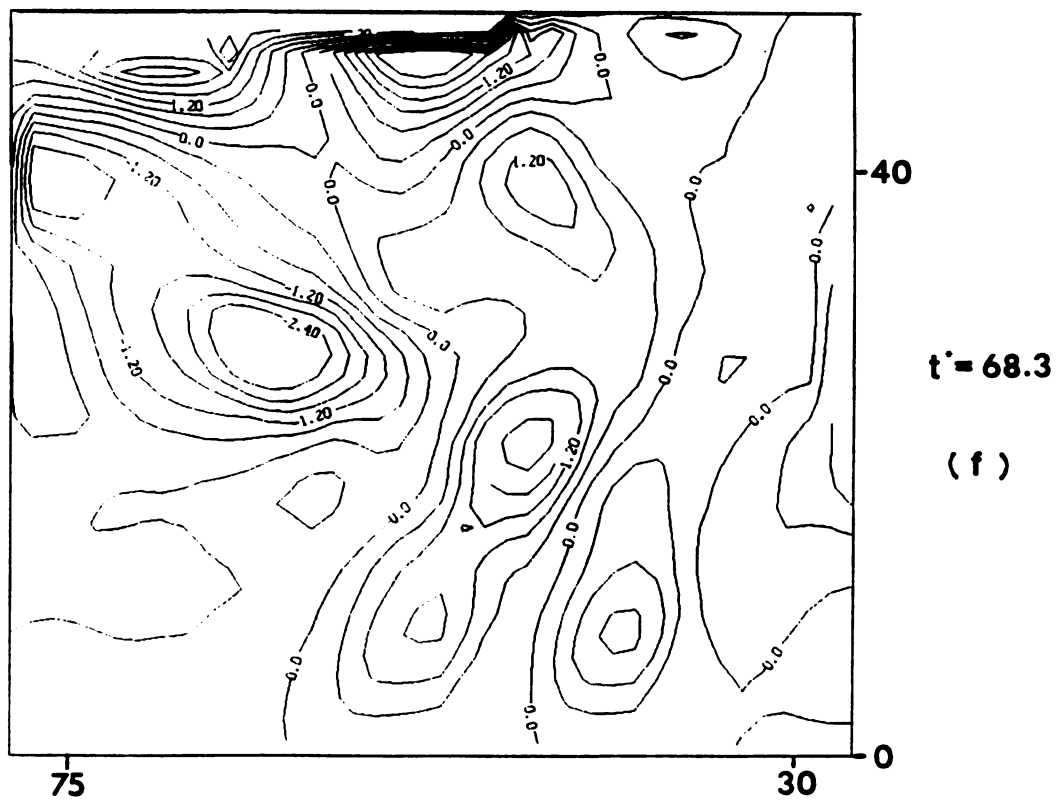
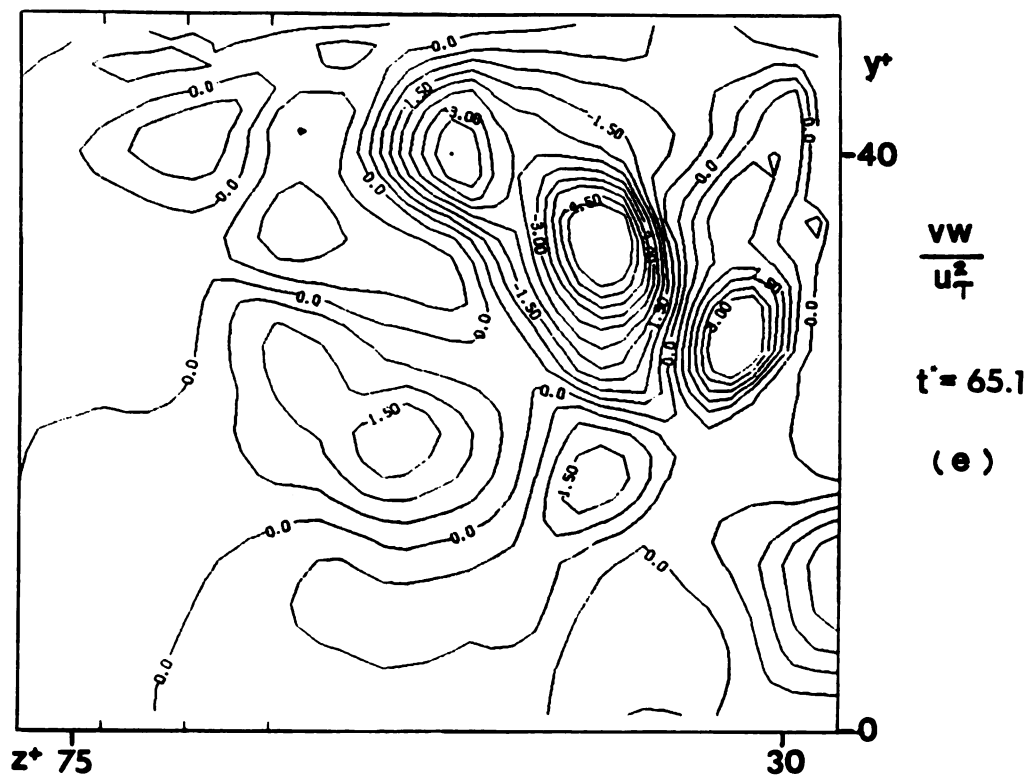
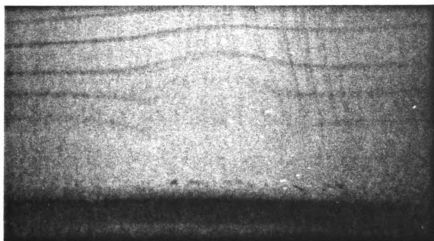
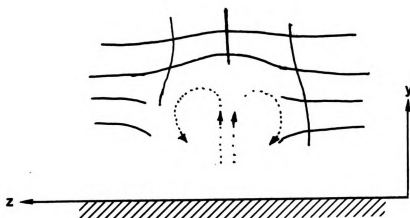


Fig. 5.24 Cont.



(a)



(b)

Fig. 5.25 A photo taken 0.02 second before $t=6.8$ seconds (shown in Fig. 5.25 (a)) indicates that a pair of counter-rotating streamwise vortices formed from the wall and moved upward.

CIRCULATION VS TIME

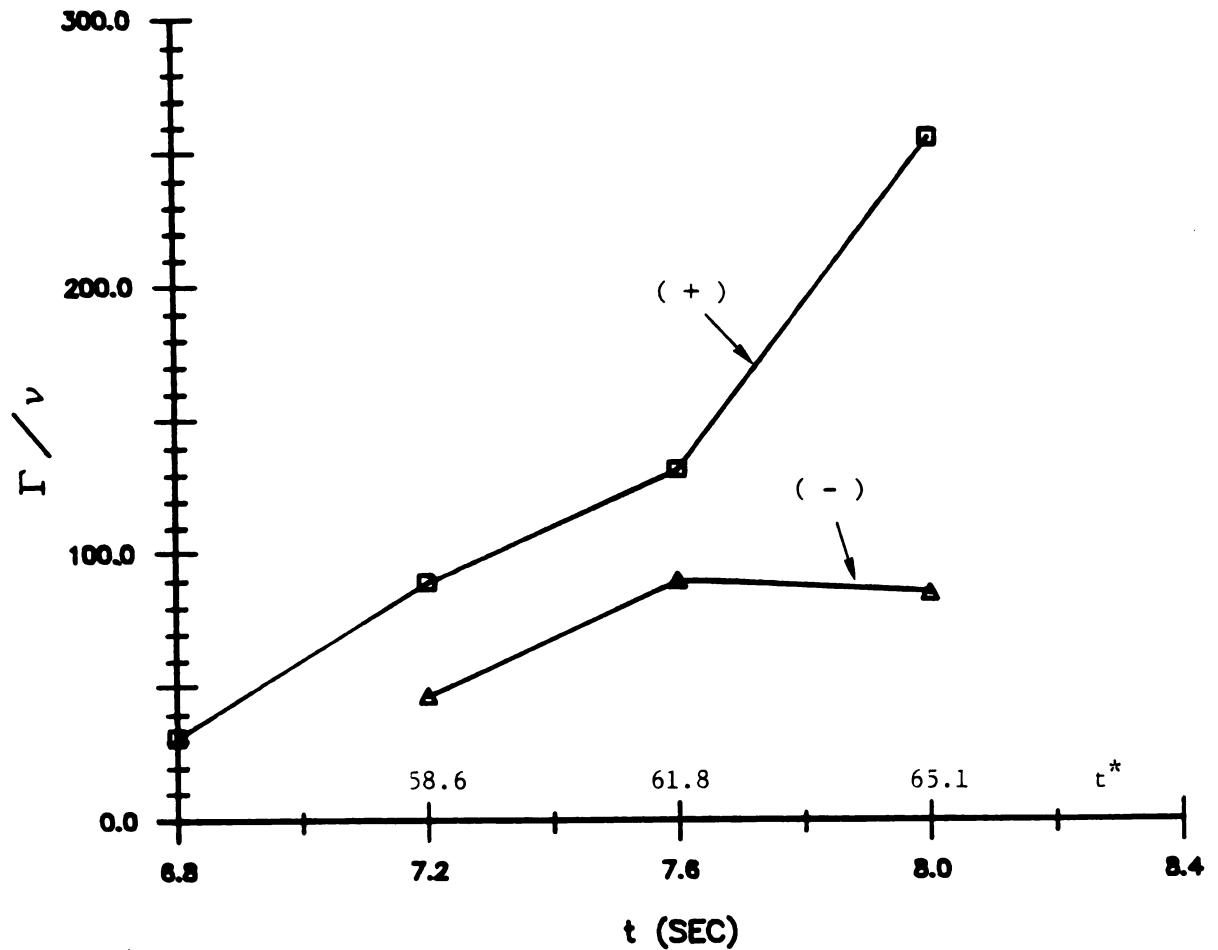


Fig. 5.26 The time evolution of total circulation of the strong vortex (the region with positive sign in Fig.5.22 (c)-(e); and the time evolution of the total circulation of one leg of the hairpin (the region with negative sign in Fig. 5.22 (c)-(e)).

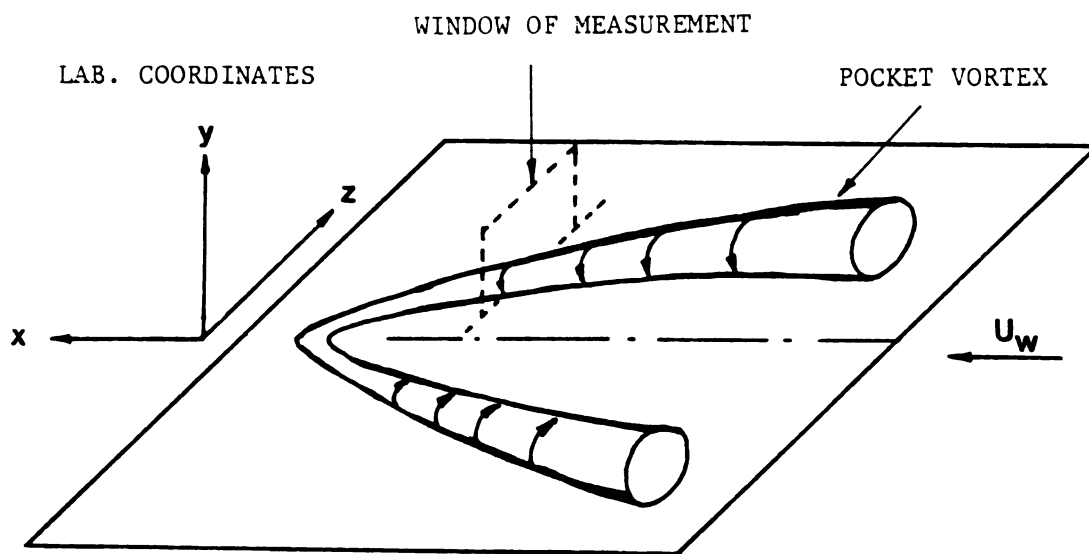


Fig. 5.27 A sketch of the pocket vortex (Falco 1980b).

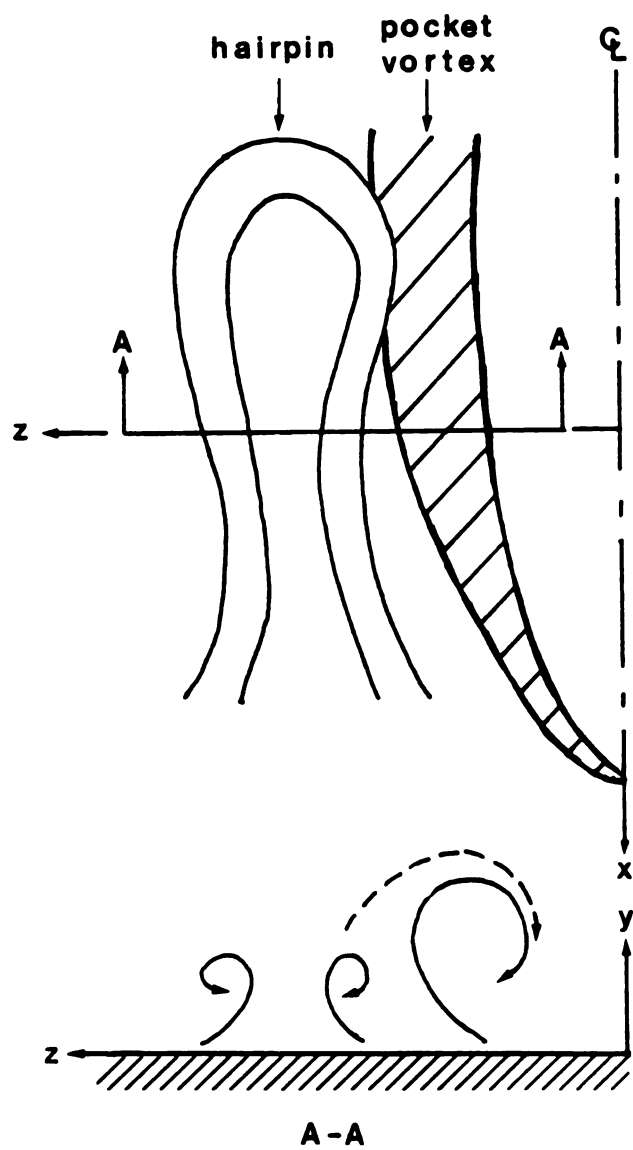


Fig. 5.28 The sketch of possible merging process.

APPENDIX

APPENDIX A

ERROR ANALYSIS OF THE PHOTOCHROMIC GRID TRACING TECHNIQUE FOR THE MEASUREMENT OF VORTICITY

Consider a unit of the mesh (see Fig. A.1). The corners of the undistorted mesh are defined as points 1a to 4a in counterclockwise rotation. We will assume that the mesh is spaced ϵ and that a worse case line movement between images is $1/2$ the mesh width. After time Δt the mesh square will move to position 1b to 4b. The vorticity

$$\begin{aligned}\omega_z &= \partial v / \partial x - \partial u / \partial y \\ &= \frac{(y_{1a} - y_{1b}) / \Delta t - (y_{2a} - y_{2b}) / \Delta t}{(x_{2a} - x_{1a})} - \\ &\quad \frac{(x_{1a} - x_{1b}) / \Delta t - (x_{4a} - x_{4b}) / \Delta t}{(y_{4a} - y_{1a})}\end{aligned}$$

where,

$$y_{1a} - y_{1b} = \Delta y_I = 1/2 \epsilon$$

$$y_{2a} - y_{2b} = \Delta y_{II} = 1/2 \epsilon$$

$$y_{4a} - y_{1a} = \Delta y_{III} = \epsilon$$

$$x_{1a} - x_{1b} = \Delta x_I = 1/2 \epsilon$$

$$x_{4a} - x_{4b} = \Delta x_{II} = 1/2 \epsilon$$

$$x_{2a} - x_{1a} = \Delta x_{III} = \epsilon$$

$$t_2 - t_1 = \Delta t$$

$$\therefore \omega_z = \frac{(\Delta y_I - \Delta y_{II}) / \Delta t}{\Delta x_{III}} - \frac{(\Delta x_I - \Delta x_{II}) / \Delta t}{\Delta y_{III}}$$

The uncertainty in the measurement of vorticity ($\delta \omega_z$) is thus,

$$\begin{aligned}
(\delta \omega_z)^2 &= (\partial \omega_z / \partial \Delta y_I \cdot \delta \Delta y_I)^2 + (\partial \omega_z / \partial \Delta y_{II} \cdot \delta \Delta y_{II})^2 \\
&+ (\partial \omega_z / \partial \Delta y_{III} \cdot \delta \Delta y_{III})^2 + (\partial \omega_z / \partial \Delta x_I \cdot \delta \Delta x_I)^2 \\
&+ (\partial \omega_z / \partial \Delta x_{II} \cdot \delta \Delta x_{II})^2 + (\partial \omega_z / \partial \Delta x_{III} \cdot \delta \Delta x_{III})^2 \\
&+ (\partial \omega_z / \partial \Delta t \cdot \delta \Delta t)^2
\end{aligned}$$

Estimates of the magnitudes of the terms are:

$$\begin{aligned}
\partial \omega_z / \partial \Delta t &= -((\Delta y_I - \Delta y_{II}) / \Delta x_{III}) / (\Delta t)^2 \\
&+ ((\Delta x_I - \Delta x_{II}) / \Delta y_{III}) / (\Delta t)^2 \\
&= -((1/2 \epsilon - 1/2 \epsilon) / \epsilon) / (\Delta t)^2 \\
&\cong 0
\end{aligned}$$

$$\partial \omega_z / \partial \Delta y_I = 1 / \Delta t \cdot \Delta x_{III} \cong 1 / \Delta t \cdot \epsilon$$

$$\partial \omega_z / \partial \Delta y_{II} = -1 / \Delta t \cdot \Delta x_{III} \cong 1 / \Delta t \cdot \epsilon$$

$$\begin{aligned}
\partial \omega_z / \partial \Delta y_{III} &= ((\Delta x_I - \Delta x_{II}) / \Delta t) / (\Delta y_{III})^2 \cong (1/2 \epsilon - 1/2 \epsilon) / \Delta t \cdot \epsilon^2 \\
&\cong 0
\end{aligned}$$

$$\partial \omega_z / \partial \Delta x_I = -1 / \Delta t \cdot \Delta y_{III} \cong -1 / \Delta t \cdot \epsilon$$

$$\partial \omega_z / \partial \Delta x_{II} = 1 / \Delta t \cdot \Delta y_{III} \cong 1 / \Delta t \cdot \epsilon$$

$$\begin{aligned}
\partial \omega_z / \partial \Delta x_{III} &= -((\Delta y_I - \Delta y_{II}) / \Delta t) / (\Delta x_{III})^2 \cong -(1/2 \epsilon - 1/2 \epsilon) / \Delta t \cdot \epsilon^2 \\
&\cong 0
\end{aligned}$$

Therefore $\delta \omega_z$ squared is equal to :

$$\begin{aligned}
(\delta \omega_z)^2 &= (\delta \epsilon / 2 \epsilon \Delta t)^2 + (\delta \epsilon / 2 \epsilon \Delta t)^2 + 0 + (\delta \epsilon / 2 \epsilon \Delta t)^2 \\
&+ (\delta \epsilon / 2 \epsilon \Delta t)^2 + (\delta \epsilon / 2 \epsilon \Delta t)^2 + 0 + 0 \\
&= 4 (\delta \epsilon / 2 \epsilon \Delta t)^2
\end{aligned}$$

Finally,

$$\delta \omega_z = (1 / \Delta t) (\delta \epsilon / \epsilon) \text{ to the first order in } \epsilon.$$

For example, (see Fig. A.2) assume that

a) meshing spacing = $1000\ \mu\text{m}$

b) line width = $100\ \mu\text{m}$

c) 10% reading error in reading the center of the $100\ \mu\text{m}$ line, i.e. $\delta\epsilon = 10\ \mu\text{m}$;

$$\therefore \delta\epsilon/\epsilon = 0.01$$

if $\Delta t = 0.01$ second (between two frames), we will have

$$\delta\omega_z = (1/\Delta t)(\delta\epsilon/\epsilon) = 1/\text{sec}.$$

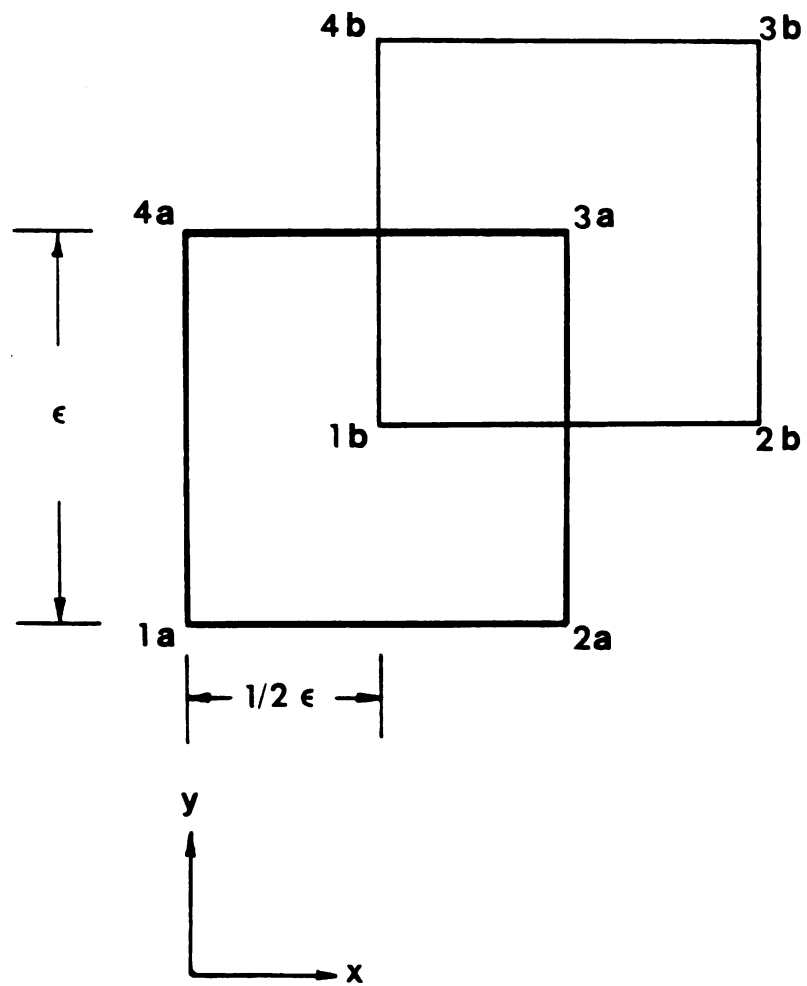


Fig. A.1 The undistorted and distorted mesh

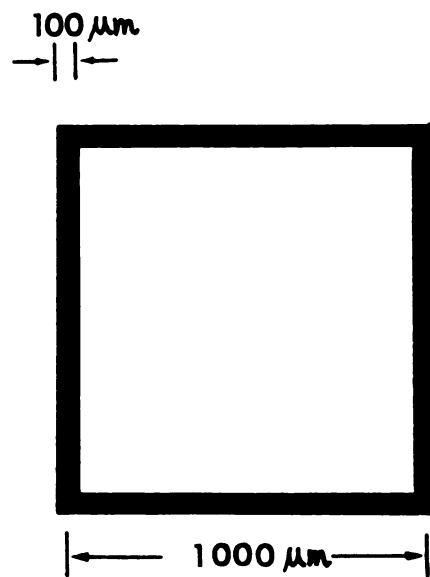


Fig. A.2 An example of the error analysis

BIBLIOGRAPHY

BIBLIOGRAPHY

- Acarlar, M.S. and Smith, C.R. 1984, "An Experimental Study of Hairpin-type Vortices as a Potential Flow Structure of Turbulent Boundary Layers", Rept. FM-5, Dept. of M.E./Mech., Lehigh Univ.
- Blackwelder, R.F. and Eckelmann, H. 1979, "Streamwise Vortices Associated with the Bursting Phenomenon", J. Fluid Mech. 94, p 577.
- Blackwelder, R.F. and Kaplan, R.E. 1976, "Burst Detection in Turbulent Boundary Layers. J. Fluid Mech. 76, p. 89-101.
- Brown, G.H. ed. 1971, "Photochromism", Wiley-Interscience, New York.
- Didden, N. 1979, "On the Formation of Vortex Rings: Rolling-up and Production of Circulation", J. Applied Math. and Physics (ZAMP), 30, p.101.
- Eckelmann, H. 1974, "The Structure of the Viscous Sublayer and the Adjacent Wall Region in a Turbulent Channel Flow", J.Fluid Mech. 65, p.439.
- Emmerling, R. 1973, "The Instantaneous Structure of the Wall Pressure under a Turbulent Boundary Layer Flow", Max-Planck-Institut fur Stromungsforschung Bericht Nr. 9.
- Falco, R.E. 1974, "Some Comments on Turbulent Boundary Layer Structure Inferred From the Movements of a Passive Contaminant", AIAA Paper 74-99.
- Falco, R.E. 1977, "Coherent Motions in the Outer Region of Turbulent Boundary Layers", Phys. Fluids Suppl. II 20, S124-S132.
- Falco, R.E. 1978, "The Role of Outer Flow Coherent Motions in the Production of Turbulence Near a Wall", in "Coherent Structure of Turbulent Boundary Layers", ed. C.R. Smith and D.E. Abbott pp. 448-461.
- Falco, R.E. 1980a, "The Production of Turbulence Near a Wall", AIAA Paper No. 80-1356.
- Falco, R.E. 1980b, "Structural Aspects of Turbulence in Boundary Layer Flows", in "Turbulence in Liquids" ed. Patterson and Zakin, pp. 1-15.
- Falco, R.E. 1980c: Combined Simultaneous Flow Visualization Hot-wire Anemometry for the Study of Turbulent Flows", J. of Fluids Engr. 102, p. 174-183.
- Falco, R.E. 1982, "A Synthesis and Model of Wall Region Turbulence Structure", in

"The Structure of Turbulence, Heat and Mass Transfer" ed. by Z. Zoric', pp. 124-135, Hemisphere Press.

Falco, R.E. 1983, "New Results, a Review and Synthesis of the Mechanism of Turbulence Production in Boundary Layers and its Modification", AIAA Paper No. 83-0377.

Falco, R.E., Chu, C.C., and Wiggert, D.C., 1983: "Experiments on Compliant Surfaces Using Quantitative Visual Technique," Symposium on Drag Reduction, National Science Academy, Washington D.C.

Falco, R.E., Chu, C.C. 1987: "Measurement of Fluid Dynamic quantities Using A Photochromic Grid Tracing Technique," Presented in SPIE 31st Annual Meeting.

Foss, J.F., Klewicki, C.L., and Disimile, P.L. 1984, NASA CR. 178098.

Gal-el-Hak, M., Blackwelder, R.F., and Riley, J.J. 1984, "On the Interaction of Compliant Coatings with Turbulent Boundary Layer Flows", J. Fluid Mech. 140, p.257

Hansen, R.J., Hunston, D.L., Ni, C.C., Reischman, M.M. 1980, "An Experimental Study of Flow-Generated Waves on a Flexible Surface", J. Sound and Vibration 68(3), P.317-334

Head, M.R. and Bandyopadhyay, P. 1981, "New Aspects of Turbulent Boundary Layer Structure", J. Fluid Mech. 107, p. 297-337.

Hecht, E. and Zajac, A. 1974, "Optics", Addison-Wesley, p.357.

Hill, M.J.M. 1894, Phil. Trans. Roy. Soc. A 185.

Hunston, D.L., Yu, C., and Bullman, G.W., "Mechanical Properties of Compliant Coating Materials", presents at ASME Energy Sources Technology Conference, Feb. 12-16, 1984

Kim, H.T., Kline, S.J., and Reynolds, W.C. 1971, "The Production of Turbulence Near a Smooth Wall in a Turbulent Boundary Layer", J. Fluid Mech. 50, p.133.

Kim, J. 1986, "Investigation of Turbulent Shear Flows by Numerical Simulation", Tenth Congress of Applied Mechanics, Austin TX June 16-20.

Lang, B.L. 1985, "Laser Doppler Velocity and Vorticity Measurements in Turbulent Shear Layers", Ph.D Thesis C.I.T.

Liang, S. 1984, "Experimental Investigation of Vortex Ring/Moving Wall Interactions", MS Thesis, Dept. Mech. Engr. Michigan State Univ.

Liang, S., Falco, R.E. and Bartholomew, R.W. 1983, "Vortex Ring/Moving Wall Interactions: Experiments and Numerical Modeling", Bull. Am. Phy. Soc., Series II, 28, p. 1397.

Lovett, J. 1982, "The Flow Fields Responsible for the Generation of Turbulence Near

the Wall in Turbulent Shear Flows", MS. Thesis, Dept. Mech. Engr. Michigan State Univ.

Mitchell, J.E. and Hanratty, T.J. 1966, "A Study of turbulence at a Wall Using a Electrochemical Wall Shear-Stress Meter", J. Fluid Mech. 26, part 1, p.199-221.

Moin, P., Leonard, A. and Kim, J. 1986, "Evolution of a Curved Vortex Filament into a Vortex Ring", Phy. Fluids 29, p.955-963

Offen, G.R., Kline, S.J. 1975, "A Proposed Model of the Bursting Process in Turbulent Boundary Layers", J. Fluid Mech. 70, part 2, p.209-228.

Oldaker, D.K. and Tiederman, W.G. 1977, "Spatial Structure of the Viscous Sublayer in Drag Reducing Channel Flow", Phy. Fluids 20 (10), p. 133-44.

Popovich, A.T. and Hummel, R.L. 1967, "Experimental Study of the Viscous Sublayer in Turbulent Pipe Flow", A.I.Ch.E.J. 14, p.21-25 (1967)

Praturi, A.K. and Brodkey, R.S. 1978, "A Stereoscopic Visual Study of Coherent Structures in Turbulent Shear Flow", J. Fluid Mech. 89, p. 251-272.

Runstadler, P.W., Kline, S.J. and Reynolds, W.C. 1963, "An Experimental Investigation of the Flow Structure of the Turbulent Boundary Layer", Dept. of Mech. Engr. Rep. MD-8, Stanford Univ.

Schraub, F.A. and Kline, S.J. 1965, "Study of the Structure of the Turbulent Boundary Layer with and without Longitudinal Pressure Gradients", Dept. of Mech. Engr. Rep. MD-12, Stanford Univ.

Seely, L.E., Hummel, R.L. and Smith, J.W., 1975, "Experimental Velocity Profiles in Laminar Flow around Sphere at Intermediate Reynolds Numbers", J. Fluid Mech. 68, p.591-608.

Signor, D. 1982, MS Thesis, Dept. of Mech. Engr., Michigan State Univ.

Smith, C.R. 1982, "Application of High Speed Videography for Study of Complex, Three-dimensional Water Flows", SPIE 348, "High Speed Photography", p. 345-352.

Smith, C.R. 1978 in "Coherent Structure of Turbulent Boundary Layers", ed. C.R. Smith and D.E. Abbott, p.50.

Smith, C.R. and Metzler, S.P. 1983, "The Characteristics of Low-speed Streaks in the Near Wall Region of a Turbulent Boundary Layer", J. Fluid Mech. 129, p. 27.

Sullivan, J.P., Widnall, S.E., and Ezekiel, S. 1973, "Study of Vortex Rings Using a Laser Doppler Velocimeter", AIAA J. Vol. 11, No.10, p.1384.

Taylor, J.R., 1982, "An Introduction to Error Analysis", Univ. Sci. Books, Calif.

Thomas, A.S.W., Bull, M.K. 1983, "On the Role of Wall-Pressure Fluctuations in Deterministic Motions in the Turbulent Boundary Layer", J. Fluid Mech. 128, p.283.

Wallace, J.M. 1986, Experiments in Fluids, Vol. 4, p.61.

Yoda, H. 1981, "Effects of Dilute Polymer Additives on the Turbulence Structure Near a Wall", MS Thesis, Dept. of Mech. Engr., Michigan State Univ.